Nonaqueous Electrolyte Design for Energy Storage and Electrosynthesis

Thesis by
Skyler Danielle Ware

In Partial Fulfillment of the Requirements for the
Degree of
Doctor of Philosophy in Chemistry

CALIFORNIA INSTITUTE OF TECHNOLOGY
Pasadena, California

2024
Defended December 13, 2023

Skyler Danielle Ware
ORCID: 0000-0002-3249-1946

ACKNOWLEDGEMENTS

No one gets a PhD on their own, and I'm certainly no exception. So many friends, family, colleagues, and mentors have helped me through this process, and I am tremendously grateful for all the support and guidance I've received along the way. While these acknowledgements are not exhaustive by any means, there are a few people I want to recognize specifically.

I don't think I would have been nearly as interested in chemistry without the influence of my high school chemistry teacher, Jeff Lazar. His zany jokes and mad-scientist approach to the subject brought a particular spark that still helps me find joy in chemistry more than a decade later.

I will be forever grateful to my undergraduate advisor, Dr. L. Robert Baker, who gave me my first opportunity to do scientific research. I spent two years in the Baker group learning to formulate a research question, communicate my findings, and persevere when things didn't go as planned. I am grateful to Dr. Baker and to everyone in the Baker group who taught me to do research and set me on the path to graduate school. Thank you also to Dr. Terry Gustafson and Dr. Steffen Lindert for their advice, support, and guidance during my undergraduate studies and beyond.

None of my work at Caltech would have been possible without my advisor, Prof. Kim See. Kim taught me to drive my own projects, to make clean figures and give clear presentations, to think outside the box, to advocate for myself, and so much more. Kim fosters a healthy and supportive group dynamic both inside and outside the lab, and I'll cherish the memories of group camping trips and barbecues just as much as the memories of group meetings and finished projects. I'm really grateful to have worked with an advisor who cares so deeply about her students.

My time at Caltech would not have been nearly as enjoyable without the wonderful members of the See group. I feel incredibly lucky to work with such brilliant scientists, and I've learned so much from all our discussions. In particular, I'd like to thank Charlie Hansen, who introduced me to the lab, mentored me through my transition to grad school, and worked with me on what would become my first paper. I'd also like to thank Team CSOE: Wendy Zhang, Brian Lee, and Christopher Povinelli. I never thought I'd end up doing organic chemistry when I joined the See group, but you all have taught me so much about the field, and I really appreciate all of our brainstorming sessions, commiseration, and celebrations when things finally

go right. Finally, I'd like to thank the women of the See group. You all are so amazing. Our weekly lunches have been one of the highlights of this past year, and I can't wait to see you flourish in your careers.

There are many other people in CCE who have helped me succeed during my PhD. I'd like to thank my committee members — Prof. Nate Lewis, Prof. Scott Cushing, and Prof. Sarah Reisman — for their guidance and support over the past five years. Thank you to Nathan Hart, Ricardo Zarazua, and Martin Mendez for making the custom glassware and equipment that our lab relies on every day. Thank you to Bruce Brunschwig and Azhar Carim for managing the MMRC, to David VanderVelde for managing the NMR facility, and to the GLAs who trained me on various shared instruments and patiently answered my many questions (and sometimes panicked emails): Michael Mazza, Ellen Yan, Jake Evans, Alex Shimozono, and Nina Gu.

Over the last year, I've found a second home in Caltech's theater department. I am so grateful to Brian Brophy, who took a chance on me as an untested actor and opened the door to what I hope will be a lifelong hobby. Through Brian's Storytelling for Scientists class and the two plays I've been a part of this year, I've found my voice and grown so much as a presenter and communicator. Thank you, Brian, for your endless encouragement and for the wonderful memories. Asmat, Sahangi, Matthew, Jane, and Michael: I've loved every minute of sharing the stage with you. And a huge thank you to everyone who worked tirelessly behind the scenes of *The Sunrise from the Moon* and *Another Revolution*.

Speaking of communicating, there are so many people I want to thank for supporting me on my journey to become a science writer. A couple years into graduate school, I realized that I was having more fun writing papers than running experiments, so I started doing everything I could to turn that into a career. I am immensely grateful for the training I received through the STEM Ambassador Program and the ComSciCon Flagship and SciWri workshops, and for the opportunity to work with Caltech Letters and Chembites while I developed my writing skills. I am especially grateful to Victoria Russell, who connected me with ComSciCon and tirelessly supported my science communication work throughout my PhD.

I was fortunate to receive a 2023 AAAS Mass Media Fellowship to pursue science journalism at *Science News* for a summer, and I am so thankful for everyone who made that experience possible. Thank you to Kristin Lewis, Olivia Monahan, and Linsi Goodin for organizing a fantastic program and building such a strong community of science writers. Thank you to the incredible 2023 cohort of Mass

Media fellows with whom I shared this summer, and thanks especially the DC crew for all the group dinners and weekend adventures. Thank you to Macon Morehouse, Carolyn Gramling, and Tina Saey for being wonderful mentors and showing me the ropes of journalism, and thank you to the rest of the *Science News* staff for sharing words of wisdom and welcoming me into the fold.

There are no words to express how much I appreciate my friends, and I absolutely would not be where I am today without them. To my Cincinnati friends, Erin, Brandon, Eddie, Nadja, Megan, Patrick, Margaret, Alex, Maddy, and Emma: thanks so much for joining me on this wild ride. Your love means the world to me. To my Pasadena friends, Wendy, Michelle, Tori, Brian, Jake, Zak, Patrick, and Dennis: thanks for the D&D adventures, the parties, the great memories, and for being with me through everything. I count myself extremely lucky to know each and every one of you.

I'd like to thank my family for their tremendous support along the way. My parents, Lori and Kevin Ware, taught me that I can do anything I put my mind to and gave me the tools to succeed. Even when they had no idea what I was working on, they cheered me on and sent me good vibes (and plenty of Cincinnati snacks). My siblings, Ashlyn and Jamie, were always there for good times and a steady stream of memes. My bonus parents, Dottie and Scott Engle, have been some of my biggest cheerleaders in grad school, and I am so grateful for their love and encouragement.

In the See group, we have a tradition of ending group meeting with pictures of our pets. So as I come to the end of my PhD, I want to thank our two wonderful cats, Ahsoka and Sabine. They've brought so much joy into my life, and I'm so grateful they've found their way into our little family.

Finally, my biggest thanks goes to my amazing husband, Sam Engle. His love and support have carried me through the tough times and made the good times so much better. From planning our wedding back home to adopting our two sweet cats to exploring LA together and hiking up every mountain we can find, my best memories are with him. Sam, my world is so much better with you in it, and I can't wait to see where the rest of our lives take us.

ABSTRACT

Electrochemically driven metal redox has enabled advances in both academic and industrial processes, including production of metals from their ores, storage of renewable energy in batteries and fuel cells, and greener chemical synthesis conditions. While many electrochemical reactions are performed in aqueous solutions, applications in energy storage and organic synthesis often require extreme applied potentials that lie outside the electrochemical stability window of water or necessitate water-free conditions to prevent undesirable side reactions. Herein, we develop tailored non-aqueous electrolytes for applications in both energy storage and organic electrosynthesis and analyze the effects of electrolyte composition on interfacial and electrochemical reactions. First, a series of highly concentrated solvate electrolytes is developed for Li-S batteries, and interfacial reactivity between the solvate electrolytes and the Li anode is investigated in detail. The addition of a fluoroether cosolvent limits electrolyte decomposition at the Li surface, improving cycling stability and enabling new high-temperature applications. Next, samarium(III)/(II) redox is investigated in a variety of non-aqueous electrolytes to support an electrocatalytic cycle for samarium-mediated carbon-carbon bond formation. The coordination environment of the samarium salt, which can be tuned through anion exchange between the electrolyte and the samarium precursor, strongly affects the reversibility and reducing power of the samarium redox couple. Third, electrolyte additives are studied to increase the desolvation barrier of Zn^{2+}. When Zn sacrificial anodes are used in organic electrosynthesis, such additives may prevent deleterious cross-plating of Zn^{2+} at the cathode. Finally, a detailed guide to troubleshooting metal sacrificial anodes is presented with special attention to issues commonly encountered in reductive electrosynthesis.

PUBLISHED CONTENT AND CONTRIBUTIONS

Martinolich, A. J., Ware, S. D., Lee, B. C., See, K. A. From Solid Electrolyte to Zinc Cathode: Vanadium Substitution in $ZnPS_3$. *J. Phys. Mater.* **2021**, 4, 024005. DOI: 10.1088/2515-7639/abe365.
SDW performed XPS measurements, analyzed XPS data, and helped write the manuscript.

Ware, S. D., Hansen, C. J., Jones, J. P., Hennessy, J., Bugga, R. V., See, K. A. Fluoride in the SEI Stabilizes the Li Metal Interface in Li-S Batteries with Solvate Electrolytes. *ACS Appl. Mater. Interfaces* **2021**, 13, 18865-18875. DOI: 10.1021/acsami.1c02629.
SDW designed and performed experiments, analyzed the data, and wrote the manuscript.

Zhang, W., Lu, L., Zhang, W., Wang, W., Ware, S. D., Mondragon, J., Rein, J., Strotman, N., Lehnherr, D., See, K. A, Lin, S. Electrochemically Driven Cross-Electrophile Coupling of Alkyl Halides. *Nature* **2022**, 604, 292-297. DOI: 10.1038/s41586-022-04540-4.
SDW performed XPS measurements, analyzed XPS data, and helped write the manuscript.

Iton, Z. W. B., Kim, S. S., Patheria, E. S., Qian, M. D., Ware, S. D., See, K. A. Battery Materials. *Comprehensive Inorganic Chemistry III* **2023**, 308-363. DOI: 10.1016/B978-0-12-823144-9.00110-2.
SDW participated in conception of the project and wrote sections 3.1.3.2, 3.1.3.3, 3.1.4, 5.1, and 5.2.

Qian, M. D., Laskowski, F. A. L., Ware, S. D., See, K. A. Effect of Polysulfide Speciation on Mg Anode Passivation in Mg-S Batteries. *ACS Appl. Mater. Interfaces* **2023**, 15, 9193-9202. DOI: 10.1021/acsami.2c19488.
SDW performed XPS measurements, analyzed XPS data, and helped write the manuscript.

Ware, S. D., Zhang, W., Charboneau, D. J., Klein, C. K., Reisman, S. E., See, K. A. Electrochemical Preparation of Sm(II) Reagent Facilitated by Weakly Coordinating Anions. *Chem. – Eur. J.* **2023**, 29, e202301045. DOI: 10.1002/chem.202301045.
SDW designed and performed experiments, analyzed the data, and wrote the manuscript.

Zhang, W., Gu, C., Wang, Y., Ware, S. D., Lu, L., Lin, S., Qi, Y., See, K. A. Improving the Mg Sacrificial Anode in Tetrahydrofuran for Synthetic Electrochemistry by Tailoring Electrolyte Composition. *JACS Au* **2023**, 3, 2280-

2290. DOI: 10.1021/jacsau.3c00305.
SDW analyzed XPS data and helped write the manuscript.

Ware, S. D., Zhang, W., See, K. A. A Guide to Troubleshooting Metal Sacrificial Anodes for Organic Electrosynthesis. *In preparation*.
SDW participated in conception of the project, led discussions on perspective content, and wrote the manuscript.

TABLE OF CONTENTS

LIST OF ILLUSTRATIONS

LIST OF TABLES

NOMENCLATURE

acac. acetylacetonate.

ALD. atomic layer deposition.

BE. binding energy.

CV. cyclic voltammetry.

DCM. dichloromethane.

DME. dimethoxyethane.

DMF. N,N-dimethylformamide.

DOL. dioxolane.

EDS. energy-dispersive X-ray spectroscopy.

EIS. electrochemical impedance spectroscopy.

Fc/Fc$^+$. ferrocene/ferrocenium.

G1. monoglyme.

G2. diglyme.

G4. tetraglyme.

LIB. lithium-ion battery.

LSV. linear sweep voltammetry.

MeCN. acetonitrile.

NHE. normal hydrogen electrode.

NMP. N-methyl-2-pyrrolidinone.

NMR. nuclear magnetic resonance.

OTf. triflate, $CF_3SO_3^-$.

PEEK. polyether ether ketone.

PVDF. polyvinylidene difluoride.

RT. room temperature.

SEI. solid-electrolyte interphase.

SEM. scanning electron microscopy.

SHE. standard hydrogen electrode.

TBA. tetrabutylammonium.

TFSI. bis(trifluoromethanesulfonyl)imide, $(CF_3SO_2)_2N^-$.

THF. tetrahydrofuran.

TPPA. tripyrrolidinophosphoric acid.

TTE. 1,1,2,2-tetrafluoroethyl-2,2,3,3-tetrafluoropropyl ether.

UV-Vis. ultraviolet-visible.

XPS. X-ray photoelectron spectroscopy.

Chapter 1

INTRODUCTION

1.1 Background and Context

The twelve principles of green chemistry guide efforts to improve sustainability and reduce the overall environmental impact of chemical reactions at both laboratory and industrial scales.[1, 2] Broadly, green chemistry focuses on improving safety, increasing energy efficiency, and reducing chemical waste. Electrochemistry, or the use of electricity to drive chemical reactions, has the power to promote several green chemistry principles in reaction design.[3–5] While the use of electricity to drive chemical processes does not inherently make those reactions perfectly sustainable, electrochemistry can make reactions "greener" by allowing the replacement of hazardous reagents with electrons, enabling the development of electrocatalytic systems, or permitting valuable products to be formed at each electrode. If the electrons used are generated from a renewable source such as wind or solar, the environmental impact of the electrochemical reaction is reduced even further. Renewable energy can also be stored for later use in electrochemical devices, reducing dependence on fossil fuels for energy.

Effectively incorporating electrochemistry into a chemical reaction almost always requires the use of a supporting electrolyte. Supporting electrolytes typically take the form of a freely dissociating salt dissolved in a liquid solvent, though other types of electrolytes may be employed instead.[6–9] Supporting electrolytes are ionically conductive but electronically insulating. The salt anions act as charge carriers in solution, balancing the movement of electrons through the circuit (Figure 1.1). The supporting electrolyte thus limits the Ohmic drop between the electrodes by increasing the conductivity of the solution. It also ensures that the electric field in solution is homogeneous and not dependent on the oxidation or reduction of the analyte.

1.2 Nonaqueous Electrolytes in Energy Storage and Electrosynthesis

Many electrochemical reactions, like the chlor-alkali process and corrosion studies, are conducted in aqueous supporting electrolytes.[10, 11] But electrochemical reactions in the fields of energy storage and organic electrosynthesis are often sensitive to water and must therefore be performed in dry organic solvents. The development

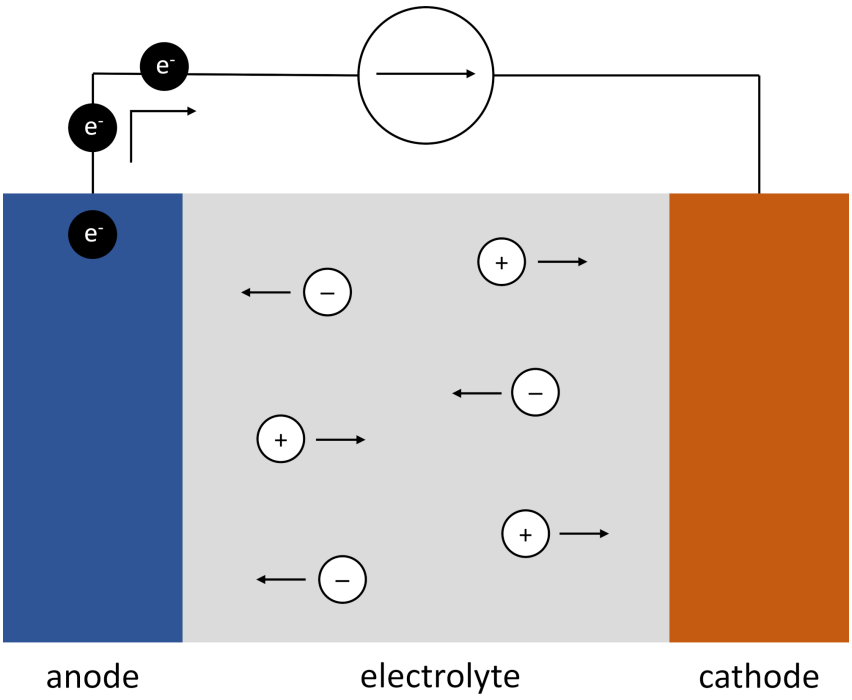

Figure 1.1: The supporting electrolyte anions migrate through the liquid electrolyte solution to charge-balance the movement of electrons through the circuit.

of nonaqueous supporting electrolytes is essential for upholding green chemistry principles and developing effective and sustainable reactions in both fields.

Water limits the potential range in which electrochemical experiments can be performed. The electrochemical stability window of water spans 1.23 V: The H_2 evolution reaction occurs at 0 V vs. the standard hydrogen electrode (SHE), and the O_2 evolution reaction occurs at 1.23 V vs. SHE. Any reactions that occur at potentials outside this range are incompatible with aqueous electrolytes, since water oxidation or reduction will be the more accessible reaction. Many important synthetic transformations require strongly reducing or oxidizing potentials,[12] so water-free electrolytes are necessary for expanding the chemical space of reactions that can employ electrochemistry. Organic solvents tend to have much wider electrochemical stability windows than water.[13, 14] Nonaqueous supporting electrolytes therefore enable electrochemical transformations in a much greater range of synthetic reactions.

Energy storage systems also require supporting electrolytes to maintain a wider electrochemical stability window than that of water. High operational voltage in a battery translates to greater power and longer battery life, which have major

implications for grid-scale energy storage. State-of-the-art Li-ion batteries operate at 3.8 V, and next-generation batteries are expected to have comparable or greater voltage, well beyond that which is compatible with water-based electrolytes.[15, 16]

Electrodes commonly used in energy storage and electrosynthesis, including Li, Mg, and Al are also known to chemically react with water. Li in particular reacts violently with water, producing flammable hydrogen gas. In addition to decomposing the electrolyte solution itself, these reactions can form an insulating oxide film at the electrode surface which prevents further oxidation or reduction reactions at the electrode and halts the desired redox reaction early.[17] In batteries, this insulating film formation can translate to low capacities and poor battery life. In electrosynthesis, reactions between the electrolyte and the anode can cause low yields and poor Faradaic efficiency. Nonaqueous electrolytes are required for developing electrochemical reactions that are compatible with strongly reducing metals.

The need for nonaqueous supporting electrolytes in organic electrosynthesis is compounded by the fact that synthetic reactions often require a specific solvent. The solubility of reactants, side reactions between the solvent and another component of the reaction, solvent cost and availability, safety, and literature precedent all dictate which solvent will be most suitable for a given synthetic transformation. Supporting electrolytes must be available in a range of solvents to best suit the reaction of interest. The electrochemical stability of the solvent at the required potential must also be considered.

Despite the need for water-free electrochemical reactions in a wide range of sectors, nonaqueous electrochemistry is generally less developed than its aqueous counterpart. While aqueous electrochemistry has been studied in depth for over 200 years, nonaqueous electrolytes have seen an explosion of interest since the mid 20th century.[18] Secondary (rechargable) batteries commercialized before the 1970s used aqueous electrolytes almost exclusively. And while key reactions in organic electrosynthesis were developed as early as 1830, organic electrochemistry has undergone a major expansion in the last 20 years, with many more reactions being electrified to access new reactivity and improve sustainability.[18]

The rapid expansion of nonaqueous electrochemistry has resulted in several beneficial applications driven by advances in supporting electrolytes. For example, reactions between energy storage electrodes and certain nonaqueous electrolytes do not necessarily yield an insulating surface film. In fact, an understanding of the reactions between nonaqueous electrolytes and graphite anodes has been critical to

the widespread adoption of Li-ion batteries: The surface film that forms from electrolyte decomposition on graphite is self-terminating and conducts Li^+, which allows the battery to cycle multiple times without further electrolyte degradation.[19, 20] Significant research is underway to develop similar surface films that can conduct multivalent metal ions such as Mg^{2+}, Zn^{2+}, or Al^{3+} on other anodes, which would enable less expensive batteries with higher capacities.[21–23]

Nonaqueous electrochemistry also presents fundamental scientific challenges. The supporting electrolyte almost always cannot be assumed to be inert and innocent relative to other components of the reaction of interest. Side reactions between the supporting electrolytes, solvents, substrates, and electrodes must be investigated in detail to ensure good electrochemical performance, as evidenced by the myriad studies of solid-electrolyte interphase (SEI) formation on battery anodes and by the extensive optimization required for organic electrosynthesis research. These interactions affect the success and efficiency of the desired transformation and must therefore be investigated to improve device performance, increase reaction yields, and develop more reliable and sustainable reactions.

1.3 Thesis Overview

This thesis addresses the interactions between nonaqueous electrolytes, metal electrodes, and species in solution for applications in electrochemical energy storage and organic electrosynthesis. The electrolytes are tailored for each reaction to yield beneficial electrode/electrolyte and analyte/electrolyte interactions which promote effective and efficient electrochemically-driven redox reactions.

Chapter 2 focuses on highly concentrated solvate electrolytes comprised of acetonitrile (MeCN) and lithium bis(trifluoromethanesulfonyl)imide (LiTFSI) for high-temperature Li-S batteries. The neat solvate electrolyte is not stable against Li metal at 90 °C, but addition of a fluoroether cosolvent increases the fluoride content in the Li SEI and limits electrolyte decomposition. Adding an AlF_3 coating on the Li metal further stabilizes the SEI and improves cyclability and initial battery capacity.

Chapter 3 focuses on electrochemically driven Sm(III)/(II) redox to support catalytic C-C bond formation. By tuning the properties of the supporting electrolyte, the efficiency of Sm redox and the reducing power of the Sm complex can be modulated. SmI_3 is electrochemically reduced to SmI_2 at bulk scale, and the electrogenerated SmI_2 is shown to perform similarly to commercial SmI_2 in a proof-of-concept organic reaction.

Chapter 4 explores electrolyte additives for electrosynthetic processes using Zn sacrificial anodes. Crown ethers slightly increase the Zn^{2+} deposition overpotential but not by enough to prevent competitive Zn^{2+} reduction at the cathode under strongly reducing conditions. Alternative experimental designs and potential future research directions for preventing Zn crossover are suggested.

Chapter 5 provides a detailed guide to troubleshooting sacrificial anodes in organic electrosynthesis. Common challenges with sacrificial anodes are explored, and experimental strategies for diagnosing and rectifying the issues are drawn from the fields of electrochemistry, surface characterization, and organic synthesis.

Chapter 6 provides an outlook for the future of nonaqueous electrolyte development in energy storage and electrosynthesis and a perspective on remaining questions in the field.

Chapter 2

FLUORIDE IN THE SEI STABILIZES THE LI METAL INTERFACE IN LI-S BATTERIES WITH SOLVATE ELECTROLYTES

Adapted from: Ware, S. D., Hansen, C. J., Jones, J. P., Hennessy, J., Bugga, R. V., See, K. A. Fluoride in the SEI Stabilizes the Li Metal Interface in Li-S Batteries with Solvate Electrolytes. *ACS Appl. Mater. Interfaces* **2021**, 13, 18865-18875. DOI: 10.1021/acsami.1c02629.

Abstract: Lithium-sulfur (Li-S) batteries offer high theoretical gravimetric capacities at low cost relative to commercial lithium-ion batteries (LIBs). However, the solubility of intermediate polysulfides in conventional electrolytes leads to irreversible capacity fade via the polysulfide shuttle effect. Highly concentrated solvate electrolytes reduce polysulfide solubility and improve the reductive stability of the electrolyte against Li metal anodes, but reactivity at the Li/solvate electrolyte interface has not been studied in detail. Here, reactivity between the Li metal anode and a solvate electrolyte (4.2 M LiTFSI in acetonitrile) is investigated as a function of temperature. Though reactivity at the Li/electrolyte interface is minimal at room temperature, we show that reactions between Li and the solvate electrolyte significantly impact the SEI impedance, cyclability, and capacity retention in Li-S cells at elevated temperatures. Addition of a fluoroether cosolvent to the solvate electrolyte results in more fluoride in the SEI which minimizes electrolyte decomposition, reduces SEI impedance, and improves cyclability. A 6 nm AlF_3 surface coating is employed at the Li anode to further improve interfacial stability at elevated temperatures. The coating enables moderate cyclability in Li-S cells at elevated temperatures but does not protect against capacity fade over time.

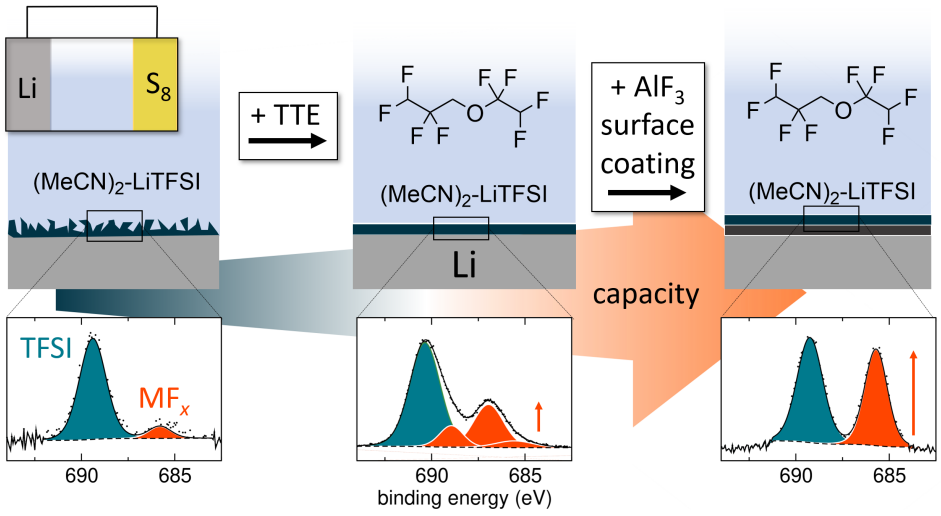

2.1 Introduction

Insufficient energy storage capacity and poor specific energy in batteries have inhibited electrification of the transportation sector.[24–27] While conventional Li-ion batteries (LIBs) remain at the forefront of the electric vehicle market, high material costs and low theoretical capacity limit their utility in the electrification of long-range, large payload sectors such as aerospace exploration and commercial ground or aerial transport.[28] Furthermore, electrification of commercial aerial transport and aerospace exploration requires lightweight energy storage systems with high specific energy. The high theoretical gravimetric capacity of Li-S batteries makes them possible candidates to meet the energy storage requirements for aerospace applications, thereby enabling new applications for batteries.[29] Li-S batteries are composed of a Li metal anode and a cathode containing elemental S_8. Li metal anodes offer high theoretical capacity (3862 mAh g^{-1}) and low reduction potential (-3.04 V vs. NHE). S cathodes are inexpensive and offer a theoretical capacity of 1672 mAh g^{-1}, which is much higher than conventional intercalation cathodes that are limited to < 250 mAh g^{-1} for various metal oxides.[30, 31]

Major challenges at both the anode and cathode have precluded commercialization of Li-S batteries. Li metal reacts with many organic solvents commonly used in LIBs, thereby limiting the number of suitable electrolyte candidates.[32] Additionally, the complex S reduction pathway causes the polysulfide shuttle effect, in which soluble S reduction intermediates dissolve in the electrolyte, diffuse away from the cathode, and are reduced at the anode.[31, 33, 34] Polysulfide shuttling leads to loss of active material, poor Coulombic efficiency, and significant capacity fade over time.

Highly concentrated electrolytes (>4 M) known as solvate electrolytes limit polysulfide solubility in Li-S cells.[35] The decreased solubility is achieved by forcing stoichiometric coordination of solvent molecules to Li^+, thereby limiting their ability to solvate polysulfide compounds. Yamada *et al.* used Raman spectroscopy to demonstrate that sufficiently high lithium bis(trifluoromethanesulfonyl)imide (LiTFSI) salt concentrations in acetonitrile (MeCN) result in coordination of most solvent molecules to Li^+.[36] The stoichiometry of the fully complexed solvate electrolyte is proposed to be 2:1 MeCN:LiTFSI (4.2 M; hereafter referred to as neat solvate electrolyte).[37] Uncoordinated, or free, MeCN is highly unstable against Li metal and is known to reductively decompose at the anode, forming gaseous products. Yamada *et al.* demonstrated that the solvate electrolyte does not react strongly with Li metal before cycling and suggested that the high salt concentrations result in preferential $TFSI^-$ decomposition at the electrode surface to yield a solid-electrolyte interphase (SEI) that prevents MeCN decomposition.[36] Even so, Nilsson *et al.* observed visible electrolyte decomposition after cycling a graphite|Li pseudo-half cell with the neat solvate electrolyte.[38]

The challenges with using the neat solvate electrolyte in electrochemical cells are associated with the high viscosity (138 cP) and low ionic conductivity (1.35 mS cm^{-1}) of the neat solvate electrolyte, compared to 2.2 cP and 10.8 mS cm^{-1} for the conventional electrolyte 1 M LiTFSI in 1:1 DOL/DME.[35, 36] To address these issues, Nazar and coworkers examined the neat solvate electrolyte with an added secondary solvent: 1,1,2,2-tetrafluoroethyl-2,2,3,3-tetrafluoropropyl ether (TTE).[35] Addition of TTE in a 2:1 solvate:TTE ratio (hereafter referred to as solvate + TTE electrolyte) significantly decreases the solvate viscosity to 22 cP and improves the ionic conductivity slightly to 1.6 mS cm^{-1}.[35] The addition of TTE to the neat solvate electrolyte may also alter the SEI formed at the Li metal electrode, potentially improving cell performance during cycling. Polysulfides are insoluble in TTE, leading to a suppressed polysulfide shuttle effect.[35, 39–41] However, TTE competes with MeCN coordination at Li^+, generating free MeCN that is able to solubilize polysulfides and react at the Li metal anode.[42]

Despite the advances in solvate electrolyte chemistry, few studies have been pursued on the reactivity between Li metal and solvate electrolytes, particularly at elevated temperatures. Solvate electrolytes provide new opportunities to examine reactivity at elevated temperatures owing to their high concentrations. The new temperature regime enabled by the solvate electrolytes is particularly useful for aerospace

applications; as an example, electrolytes with high boiling points are required for aerial missions to Venus, where temperatures of 90–120 °C are common just below the planet's middle cloud layer.[43] Li-S cells with glyme-LiTFSI solvate electrolytes have been shown to cycle at 55 °C with improved electron transfer kinetics, limited electrolyte decomposition on Li metal, and a quasi-solid state S reduction pathway.[41] A similar study has yet to be performed with MeCN-LiTFSI solvate electrolytes to determine the effect of elevated temperature on electrolyte stability and the S reduction pathway. Examining Li-S cells with MeCN-based solvate electrolytes at elevated temperatures provides valuable insight into interfacial reactivity and informs new applications for liquid-phase electrolytes.

Herein we study the temperature-dependent reactivity between Li metal and the solvate electrolyte with and without TTE. Electrochemical impedance spectroscopy indicates that reactivity between Li metal and the neat solvate electrolyte is accelerated at elevated temperatures, forming a high impedance surface film on the Li anode, while the presence of TTE in the electrolyte limits electrolyte decomposition at the Li anode. We demonstrate that reactivity between the solvate electrolytes and the Li anode strongly influences cyclability and capacity retention in Li-S cells. The Li anode is investigated by X-ray photoelectron spectroscopy (XPS) after reaction with the solvate electrolytes at room temperature and 90 °C, and the resulting surface films are characterized. The results indicate that TTE is necessary to stabilize the electrode/electrolyte interface and mitigate Li degradation. To further stabilize the interface, an AlF_3 coating is added to the Li anode to act as a barrier to electrolyte decomposition. The AlF_3 coating improves cell cyclability in the neat solvate electrolyte but does not protect against electrolyte decomposition over the full cell lifetime.

2.2 Methods

Materials Preparation

All electrolytes were prepared in an Ar-filled glovebox. Lithium bis(trifluoromethanesulfonyl) imide (LiTFSI, 99.95%, Sigma-Aldrich) was dried under vacuum at 120 °C overnight prior to use. Acetonitrile (MeCN, 99.9%, Fisher Scientific) was dried on a solvent purification system and transferred to the glovebox without exposure to air. The cosolvent 1,1,2,2-tetrafluoroethyl-2,2,3,3-tetrafluoropropyl ether (TTE, Synquest Laboratories) was degassed by freeze-pump-

thaw technique prior to introduction into the glovebox. The neat solvate electrolyte was prepared by combining MeCN and LiTFSI in a 2:1 mole ratio and stirring overnight to yield a colorless solution. Electrolytes with TTE were prepared by combining the neat solvate and TTE in a 2:1 volume ratio and stirring overnight.

Sulfur electrodes were prepared on the benchtop using a conventional method of electrode fabrication. Preparation of a typical electrode slurry involved mixing 40 mg polyvinylidene difluoride (PVDF, MTI) and 1 mL N-methyl-2-pyrrolidinone (NMP, anhydrous, 99%, Sigma Aldrich) in a Thinky centrifugal mixer for 15 min. Sulfur (200 mg, 99.998%, Sigma-Aldrich) and Super P conductive carbon (160 mg, 99+%, Alfa Aesar) were ground with a mortar and pestle and added to the PVDF solution along with an additional 1.7 mL NMP. The components were mixed in the centrifugal mixer for an additional 15 min. The slurry was cast on aluminum foil with a doctor blade at a thickness of 35 μm, dried in air at ambient temperature for at least 48 hours, then dried at 55 °C for 8 hours to yield 50 wt. % S electrodes.

AlF_3-coated Li was prepared by atomic layer deposition (ALD) in a nitrogen-filled glovebox equipped with a forced air moisture remover as reported previously.[44] A total of 100 ALD cycles were performed, yielding an average thickness of 6 nm.

Electrochemical Testing

All electrochemical cells were prepared in an Ar-filled glovebox. Galvanostatic cycling experiments were performed in 2032 coin cells with a Li foil (99.9%, Alfa Aesar) anode (either coated with AlF_3 or mechanically cleaned immediately prior to use), S cathode, Celgard 2400 separator, and 6 drops of electrolyte from a glass pipett (approx. 80 mg). Celgard separators were dried in air at 80 °C, then transferred to the glovebox before use. Electrochemical impedance spectroscopy (EIS) experiments were performed in Li-Li symmetric coin cells with ± 10 mV amplitude. Galvanostatic cycling experiments were conducted at a rate of C/10 (corresponding to an areal current density on the Li electrode ranging from 0.34–0.52 mA cm^{-2}). The cutoff discharge voltage was 1.2 V, and the cutoff charge voltage was 3 V. Electrochemical experiments were conducted on either a BCS 805 battery cycler (Bio-Logic) or a VMP3 potentiostat (Bio-Logic). High temperature cycling and EIS were performed in a Fisher Scientific gravity oven.

Sample Characterization

Raman spectra were collected using a Horiba Instruments XploRA PLUS Raman spectrometer. Samples were measured in a glass tube sealed with epoxy to prevent

reactions with air. All spectra were collected by averaging 40 acquisitions lasting 5 s each with an 1800 gr/mm grating, 50 μm slit, and 500 μm hole. The excitation wavelength was 785 nm. Temperature dependent Raman spectra were obtained by placing the glass tube in a custom copper heating mantle.

UV-Visible spectroscopy experiments were performed on a variable-temperature spectrometer (Varian) in a screw-cap cuvette. Temperature-dependent studies were performed with saturated solutions of Li polysulfides in neat solvate and in solvate + TTE electrolytes, prepared in an Ar-filled glovebox. Li polysulfide solutions were synthesized by combining stoichiometric amounts of lithium sulfide (Li_2S, Alfa Aesar, 99.9%) and sulfur in 1:1 (v/v) dioxolane (Sigma Aldrich) and dimethoxyethane (99.5 %, Sigma Aldrich) solvent under Ar atmosphere to target a nominal "Li_2S_6" stoichiometry. The solution was heated to 75 °C and reacted overnight under flowing Ar. The solvent was removed under vacuum at room temperature on a Schlenk line, yielding an orange residue.

^{1}H-NMR experiments were conducted on a Bruker 400 MHz spectrometer equipped with a 5 mm Prodigy broadband cryoprobe. Samples were diluted by a factor of 20 in deuterated MeCN (>99.8%, Sigma Aldrich) in an Ar-filled glovebox and sealed in screw-cap NMR tubes (Wilmad) to prevent exposure to air.

Samples for X-ray photoelectron spectroscopy (XPS) were prepared by assembling Li-Li symmetric coin cells with either neat solvate electrolyte or solvate + TTE electrolyte. The cells were held at either room temperature or 90 °C at open circuit for 24 h. The cells were then disassembled inside an Ar-filled glovebox and the Li was removed. Each Li sample was rinsed with 5-6 drops of dimethoxyethane (Sigma Aldrich, 99.5%) and dried under ambient glovebox conditions for at least 48 hours before analysis. The samples were mounted on a vacuum stage under Ar atmosphere, then transferred to the XPS with brief exposure to air.

XPS data were collected using a Surface Science Instruments M-Probe ESCA controlled by Hawk Data Collection software. Low-resolution survey spectra were acquired between binding energies of 1–1000 eV. Higher-resolution detailed scans, with a resolution of 0.065 eV, were collected on individual XPS lines of interest. The sample chamber was maintained at < 2 x 10^{-8} Torr. The XPS data were analyzed using CasaXPS analysis software, and individual peaks were fit with Shirley backgrounds. Peaks were deconvoluted using asymmetric Gaussian-Lorentzian line shapes. Spectra were referenced to adventitious C at 285 eV.

2.3 Results and Discussion

Li metal reactivity in solvate electrolyte with and without TTE

Interfacial reactivity between Li metal and the solvate electrolytes at room temperature (RT) and at 90 °C was probed using electrochemical impedance spectroscopy (EIS). Figure 2.1 shows EIS data for Li-Li symmetric cells prepared with neat solvate and solvate + TTE electrolytes. Spectra were collected continuously over a 47 h monitoring window. Generally, the Nyquist plots show two semicircular features. In all cases, the diameter of the high-frequency semicircle increases over time, suggesting that the feature it describes evolves over time. The high frequency semicircle is therefore ascribed to the surface film formed on the Li metal as the majority of reactivity in the cell is expected to occur between the Li metal electrode and the solvate electrolyte. A second semicircle is observed in the low frequency region of Figure 2.1a, c, and d. The width and height of the semicircle do not change over time, suggesting that the component does not evolve over the monitoring window. The low frequency feature is therefore attributed to a stable interface within the cell and is not considered further. A single semicircle is observed in the neat solvate electrolyte at 90 °C because a limited frequency window was used for those spectra (Figure 2.1b). To capture the low frequency feature, we would need to measure down to 1 μHz, which would require over 5 h of data acquisition. The 5 h window is much longer than the timescale of reactivity of the electrode at 90 °C and thus leads to distorted Nyquist plots. Therefore, the cell was measured to 1 Hz to maintain stability in the EIS measurements and the second semicircle is not observed.

The high frequency semicircle of each spectrum is fit with an equivalent circuit composed of a resistor (R_1) in series with an R_2/Q_2 circuit (where Q_2 is a constant phase element). R_1 describes the cell's series resistance, which is primarily electrolyte resistance. The R_2/Q_2 circuit represents resistance of the surface film formed on the Li anode. The constant phase element is employed to describe non-ideal capacitance, often attributed to interfacial surface roughness in battery systems.[45] The reactivity of the Li electrode with the neat solvate electrolyte can be inferred from the change in R_2 over time (Figure 2.2a). In the neat solvate electrolyte at RT, R_2 increases from 167.0 ± 68.4 Ω to 269.6 ± 95.7 Ω over 47 h (2.2 Ω/h), where the errors are determined by the standard deviation of three replicate measurements. In the neat solvate electrolyte at 90 °C, R_2 increases much faster from 2.4 ± 0.8 Ω to 727.9 ± 230.9 Ω over 47 h (15.5 Ω/h). The rapid increase of R_2 at 90 °C suggests faster reaction of the Li surface over time, resulting in an unstable, high impedance

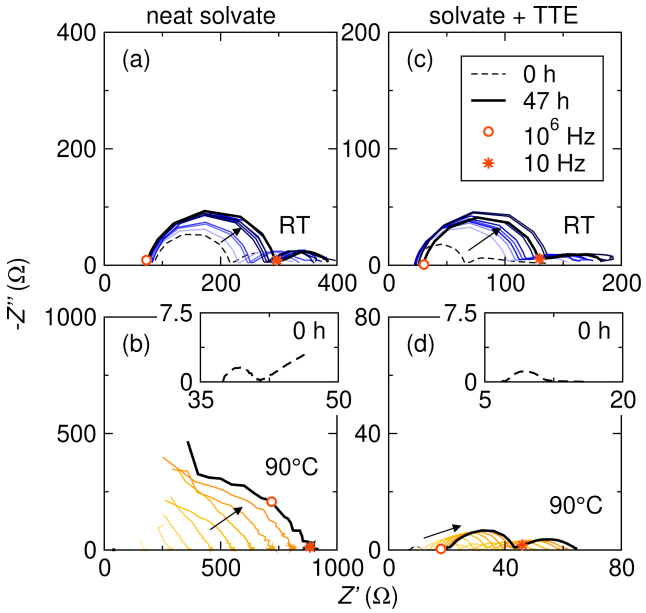

Figure 2.1: Nyquist plots of Li-Li symmetric cells prepared with (a) neat solvate electrolyte at room temperature (RT), (b) neat solvate electrolyte at 90 °C (inset: EIS spectrum collected at t = 0), (c) solvate + TTE electrolyte at RT, and (d) solvate + TTE electrolyte at 90 °C. The insets in (b) and (d) show the EIS spectrum collected at t = 0. EIS data was collected from (a,c,d) 10^6–10^{-6} Hz and (b) 10^6–1 Hz with a 10 mV sinus amplitude continuously for 47 h. Addition of TTE to the solvate electrolyte yields lower surface film resistance over the full monitoring window at both temperatures.

surface film. Initially, R_2 is lower at 90 °C compared to RT due to reduced kinetic barriers at elevated temperatures.

Adding TTE to the solvate electrolyte affects R_2 at both RT and 90 °C. R_2 is plotted as a function of time for cells with solvate + TTE electrolyte in Figure 2.2b. In general, cells prepared with solvate + TTE electrolyte exhibit lower R_2 at all temperatures than cells with neat solvate electrolyte, likely due to improved wetting of the Celgard separator concomitant with the reduction in solvate viscosity after addition of TTE.[35] At RT, surface film resistance increases from 39.2 ± 3.7 Ω to 88.8 ± 10.4 Ω over 47 h (1.1 Ω/h) - a slightly smaller increase than that observed in cells prepared with neat solvate electrolyte. At 90 °C, the difference between the two electrolytes becomes more apparent. Cells prepared with solvate + TTE electrolyte maintain lower R_2 at 90 °C than at RT for the full 47 h duration, increasing from 0.8 ± 0.6 Ω to 20.7 ± 11.9 Ω (0.4 Ω/h). The lower R_2 suggests formation of a lower impedance surface film on the Li electrode and decreased reactivity between Li and the electrolyte over time.

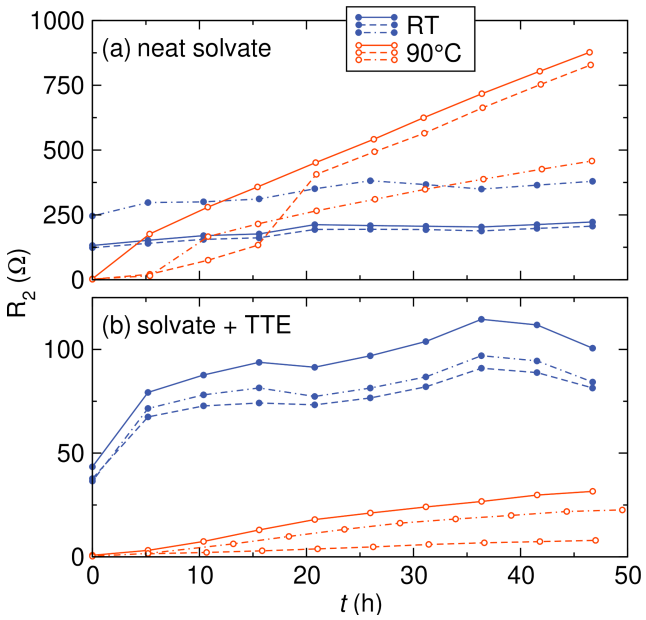

Figure 2.2: Surface film resistance, R_2, extracted from the Nyquist plots of Li-Li symmetric cells at RT and 90 °C with (a) the neat solvate electrolyte and (b) the solvate + TTE electrolyte. Data from three replicate cells are shown in each electrolyte at each temperature. R_2 increases rapidly in cells with neat solvate electrolyte at 90 °C, suggesting relatively fast reactivity between the electrolyte and the Li electrode. When TTE is added to the electrolyte, R_2 remains small and increases slowly over time, suggesting formation of a low impedance and more protective surface film on the Li electrode.

When TTE is added to the electrolyte, R_2 is lower at both RT and 90 °C over the full 47 h monitoring window, indicating that TTE stabilizes the electrode/electrolyte interface. Without TTE, R_2 increases substantially, suggesting formation of a high impedance surface film at the Li electrode. MeCN is known to decompose on Li, forming products that include LiCN, CH_4, and C_2H_4.[36, 46, 47] In solvate electrolytes, however, MeCN is coordinated to Li^+ centers, reducing its reactivity with Li metal before cycling.[36] Although reactivity is reduced in highly concentrated electrolytes relative to conventional dilute systems, some concentration of MeCN in the solvate remains uncoordinated, or free,[36] and would likely react at the Li surface, leading to electrolyte depletion and formation of an insulating surface film. We expect that elevated temperatures will also shift the equilibrium towards free MeCN following LeChatelier's Principle, causing greater reactivity at the Li electrode at high temperatures. Addition of TTE has also been shown to increase the concentration of free MeCN,[42] but the high impedance surface film likely associated with increased MeCN decomposition (*vide infra*) is not observed in cells

containing the solvate + TTE electrolyte suggesting a secondary effect in the TTE-containing electrolytes. Addition of TTE to the electrolyte could simply limit the activity of MeCN at the Li electrode by reducing its concentration or TTE could change the SEI on Li to yield a lower impedance surface film.

To investigate the effects of temperature and TTE presence on free MeCN concentration, the C≡N stretching mode of MeCN was examined via Raman spectroscopy. Figure 2.3a-b shows the Raman spectra of the solvate electrolyte with and without TTE in the region containing solvent-related modes. Four modes are observed between 2225 and 2325 cm^{-1} (Figure 2.3a-b), and the spectra are normalized to the most intense mode, labeled mode *b*. Mode *a* (2257 cm^{-1}) is ascribed to the C≡N stretch in free MeCN, and mode *b* (2279 cm^{-1}) is assigned to the C≡N stretch in MeCN coordinated to Li^+.[48] Modes *c* and *d* (2295 cm^{-1} and 2310 cm^{-1}, respectively) are assigned to C-H stretching in free and coordinated MeCN, respectively.[48] Since the C-H stretching modes are less sensitive to Li^+ coordination than the C≡N modes, the C≡N modes are examined to probe Li^+ coordination and modes *c* and *d* are not considered further. The relative intensity of mode *a* increases with respect to *b* with increasing temperature in both electrolytes, indicating a shift in equilibrium toward free MeCN. To quantify the relative ratio of free MeCN to coordinated MeCN, the ratio of the peak areas was determined by fitting the Raman spectra with component Gaussian functions. The area ratio is plotted as a function of temperature for both electrolytes in Figure 2.3c. The relative concentration of free MeCN trends similarly with temperature in both electrolytes, suggesting that temperature is the dominant driving force affecting free MeCN concentration. The solvate + TTE electrolyte exhibits larger free MeCN concentrations at all temperature points (previously explored at RT[42]), indicating that the higher impedance surface film measured in the absence of TTE cannot be explained in terms of increased free MeCN in the neat solvate electrolyte. The results suggest that TTE acts to stabilize the Li surface and prevent the reactions that would otherwise occur between Li and free MeCN in the neat solvate electrolyte.

The decrease in surface film resistance as shown by EIS and the trends in free MeCN concentration as indicated by Raman spectroscopy suggest that TTE significantly impacts the surface film formed on Li. To further characterize the surface film resulting from reactivity at the Li-electrolyte interface, XPS was employed to examine Li metal after reaction with the neat solvate electrolyte. The surface film is generated by chemical reactivity between Li metal and the solvate electrolytes rather

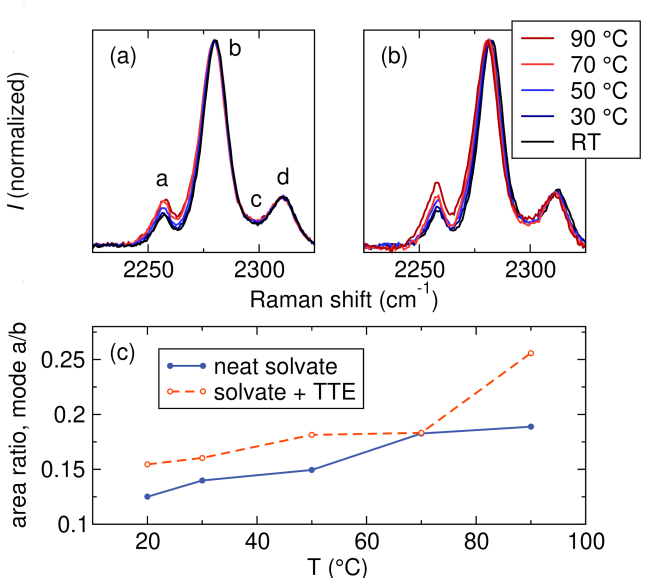

Figure 2.3: Raman spectra of MeCN-related modes in (a) neat solvate electrolyte and (b) solvate + TTE electrolyte. (c) Relative ratios of free MeCN to coordinated MeCN trend similarly with temperature in both electrolytes and indicate that temperature, rather than TTE content, is the driving force affecting free MeCN content.

than through electrochemical cycling but will be referred to as an SEI hereafter. Li metal was reacted for 24 h with the neat solvate electrolyte at both RT and 90 °C. Figure 2.4a-c shows the XPS spectra measured on the surface of the Li metal following 24 h reaction with the neat solvate electrolyte at RT. In the O region of the XPS spectrum (Figure 2.4a), two major peaks are observed. The lower binding energy (BE) peak at 532.5 eV is in the region of sulfate species and is assigned to Li_2SO_4, likely a decomposition product derived from the TFSI anion.[49] The higher BE peak at 533.7 eV is assigned to Li_2O.[50] A single peak is present at 400.1 eV in the N region of the spectrum (Figure 2.4b) and is assigned to adsorbed MeCN.[51] The XPS signal from F (Figure 2.4c) is dominated by an intense peak at 689.4 eV which is likely related to the -CF_3 group in the adsorbed TFSI anion. A smaller peak appears at 685.7 eV and is assigned to LiF.[52] The low intensity of the LiF peak as compared to the TFSI-derived peak suggests minimal decomposition of LiTFSI on Li metal at RT.

Figure 2.4d-f shows the XPS spectra of the Li metal surface following 24 h reaction with the neat solvate electrolyte at 90 °C. At elevated temperatures, the surface speciation after reaction is different than that observed after reaction at RT. In the O region of the spectrum (Figure 2.4d), a new, lower BE peak appears at

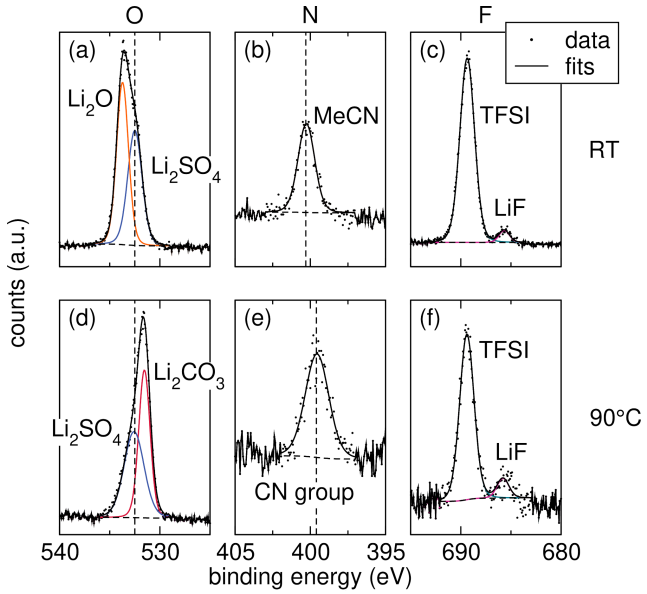

Figure 2.4: The (a) O, (b) N, and (c) F regions of the XPS spectra of Li metal reacted with neat solvate electrolyte at RT. The (d) O, (e) N, and (f) F regions of the XPS spectra of Li metal reacted with neat solvate electrolyte at 90 °C. Formation of carbonate species and a shift of the -CN group to lower BE at 90 °C suggest decomposition of the neat solvate electrolyte at high temperatures. Dotted lines indicate positions of the Li_2SO_4 and MeCN-related peaks and are guides for the eye.

531.5 eV and is in the region of Li_2CO_3.[49] The Li_2O peak observed after reaction at RT is not present after reaction at 90 °C. The presence of Li_2CO_3 in the Li SEI has been linked to interfacial instability and the continuous consumption of organic electrolytes following SEI breakdown and repair during cycling with Li metal anodes.[53, 54] The single peak in the N region of the spectrum (Figure 2.4e) is observed at 399.4 eV, a lower BE than after reaction at RT. The peak appears in the BE range of an organic -CN group but is too low to be assigned to adsorbed MeCN, suggesting some reduction of the MeCN at the surface. The appearance of the carbonate peak and the shift of the N peak to lower BE, coupled with the increase in free MeCN content at elevated temperatures, suggest decomposition of MeCN on the Li surface at 90 °C. Interestingly, the F region of the XPS spectrum shown in Figure 2.4f yields the same two peaks as in the case of the RT reaction. As LiTFSI is the only F-containing compound present, the consistent F speciation suggests that the stability of LiTFSI against Li metal does not change significantly at 90 °C.

The decomposition of MeCN at the Li surface would result in small changes to the bulk electrolyte speciation. MeCN decomposition was probed by ^{1}H-NMR

spectroscopy, which revealed the evolution of new peaks after reaction between the neat solvate electrolyte and Li at 90 °C. No new peaks appeared after reaction at RT.

To determine if the SEI formed after reaction between Li and the solvate + TTE electrolyte is different from that of the neat solvate electrolyte, leading to the lower impedance interface observed by EIS, the SEI generated from reaction between the solvate + TTE electrolyte and the Li anode was also studied by XPS. Figure 2.5a-c shows the XPS spectra of Li metal following 24 h reaction with the solvate + TTE electrolyte at RT. The O region of the spectrum (Figure 2.5a) yields peaks very similar to those observed after reaction with the neat solvate electrolyte (Figure 2.4a). The lower BE peak at 532.2 eV is assigned to Li_2SO_4,[49] and the higher BE peak at 533.4 eV is assigned to Li_2O.[50] A third, new peak at 534.6 eV appears with low intensity, which is in the range of primarily organic O-containing species and could be due to contamination.[55] The N region of the spectrum (Figure 2.5b) again yields a single peak at 400.0 eV which is assigned to adsorbed MeCN.[51] In the F region (Figure 5c), two major peaks are observed. The lower BE peak at 685.4 eV is assigned as LiF and may be shifted to slightly lower binding energy due to the formation of a thicker or less conductive SEI.[52] The higher BE peak occurs at 689.1 eV and is most likely derived from either the TFSI anion or TTE. The similarity between the Li surfaces after reaction with the neat solvate and with the solvate + TTE electrolytes indicates that TTE does not significantly alter the surface speciation on Li after chemical reaction at RT. The EIS data in Figure 2.2 also suggests that the SEI is not significantly impacted by TTE at RT; though cells with neat solvate exhibit higher R_2 over the full monitoring window due to poor wetting of the electrodes,[35] the rate of increase in R_2 is similar.

Figure 2.5d-f shows the XPS spectra of Li metal after 24 h reaction with the solvate + TTE electrolyte at 90 °C. The surface speciation again changes at elevated temperatures. In the O region (Figure 2.5d), the peak at 533.1 eV is assigned to a sulfate species but appears at too high of a BE to be Li_2SO_4 (532.2 eV).[49] A lower BE peak again appears at 531.5 eV and is assigned to Li_2CO_3.[49] The Li_2CO_3 peak is small compared to the Li_2SO_4 peak, unlike in the 90 °C reaction with the neat solvate electrolyte (Figure 2.4d). The N region of the XPS spectrum (Figure 2.5e) exhibits one major peak at 399.9 eV, at a slightly lower BE than the MeCN peak observed at RT. The peak observed at 90 °C lies in the range of a -CN group in an organic molecule but is too low to be definitively assigned as adsorbed MeCN. The observed reduction in N-species BE may indicate MeCN decomposition at the

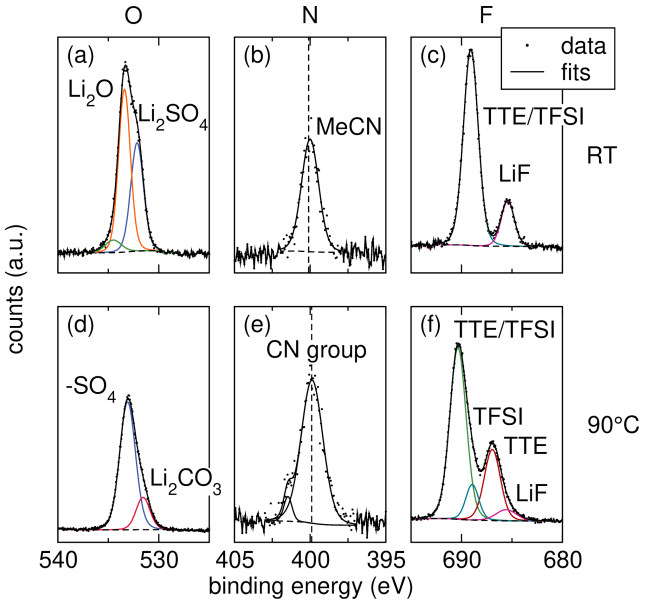

Figure 2.5: The (a) O, (b) N, and (c) F regions of the XPS spectra of Li metal reacted with solvate + TTE electrolyte at RT. The (d) O, (e) N, and (f) F regions of the XPS spectra of Li metal reacted with solvate + TTE electrolyte at 90 °C. Reduced signal from Li_2CO_3 and additional F species after reaction at 90 °C likely contribute to the formation of a low-impedance surface film. Dotted lines indicate the positions of the MeCN peaks and are guides for the eye.

Li surface, similarly to the neat solvate electrolyte at 90 °C (Figure 2.4e). The decreased intensity of the Li_2CO_3 peak in the O region of the XPS spectrum and the smaller shift in N-species BE (0.2 eV) indicate reduced MeCN decomposition at the Li surface at 90 °C in the presence of TTE relative to the case of the neat solvate electrolyte.

Additional peaks appear in the F region of the XPS spectrum (Figure 2.5f) following reaction with the solvate + TTE electrolyte at 90 °C. The lowest BE peak appears at 685.6 eV and is assigned to LiF.[56] Three additional peaks appear at higher binding energies of 686.9, 688.9, and 690.4 eV and are likely from the TFSI anion or from TTE. Since the F speciation did not significantly change between RT and 90 °C reaction with the neat solvate electrolyte as shown in Figure 2.4f, it is likely that the new peaks are related to the interaction between Li and TTE at elevated temperatures.

Bulk stability of the solvate + TTE electrolyte was probed by ^{1}H-NMR. No new peaks were observed at RT or at 90 °C, indicating suppressed electrolyte decomposition when TTE is present.

The appearance of new fluorinated species on the Li surface and the reduction in relative intensity of the Li_2CO_3 peak after reaction at 90 °C in the presence of TTE suggest that TTE affects the speciation at the Li/electrolyte interface. The EIS and XPS results suggest that TTE enables the growth of a low impedance SEI and precludes formation of the resistive surface film that would otherwise develop following high-temperature reactions between Li and MeCN.

Cycling behavior of Li-S cells

The surface layer generated on Li by reaction with TTE may act as a barrier to prevent further reactions between the Li anode and the electrolyte. To evaluate the capabilities of the solvate electrolyte and assess the extent of Li stabilization by TTE, we evaluated Li-S cells at RT and 90 °C using the neat solvate and solvate + TTE electrolytes. Figure 2.6a shows discharge and charge curves for cycle 1 of a Li-S cell prepared with neat solvate electrolyte. At RT, the cell immediately polarized to the cutoff voltages (1.2 V and 3 V, data not shown), which we attribute to poor wetting of the Li surface due to the high viscosity of the electrolyte and to the low conductivity of the solvate electrolyte.[35] At 90 °C, however, substantial discharge capacity is achieved on the first reduction. The profile is very different from that observed in conventional 1 M electrolyte, in which two discernible discharge plateaus are observed due to the multistep reduction processes.[57, 58] Here, however, because Li polysulfide solubility is reduced,[35, 41] the discharge profile appears similar to that studied at 55 °C, in which a quasi-solid state reduction mechanism is invoked with various nucleation events that cause inflections in the profile.[41, 59] At 90 °C, the cell exhibits an initial discharge capacity of 1004 ± 261 mAh g^{-1}. Interestingly, the subsequent charging profile is reproducibly unstable, which could be an effect of the reactivity of the Li anode with the electrolyte at elevated temperatures.

Figure 2.6b shows discharge and charge curves for the first and twentieth cycles of Li-S cells prepared with the solvate + TTE electrolyte. As previously observed, at RT addition of TTE enables cell cycling but at comparatively low capacities.[59] We observe a sloping discharge profile, which has been attributed to poor kinetics of the Li_2S conversion reaction.[59] At 90 °C, a single plateau is observed in the discharge, and much higher capacities (1187 ± 57 mAh g^{-1}) are obtained compared to the RT data. The shape of the profiles is similar to that reported previously at 55 °C.[59] Unlike the cells prepared with neat solvate electrolyte, cells with solvate + TTE electrolyte can be reversibly cycled with high Coulombic efficiency and stable voltage profiles. We note that the Li metal electrode is more stable at elevated

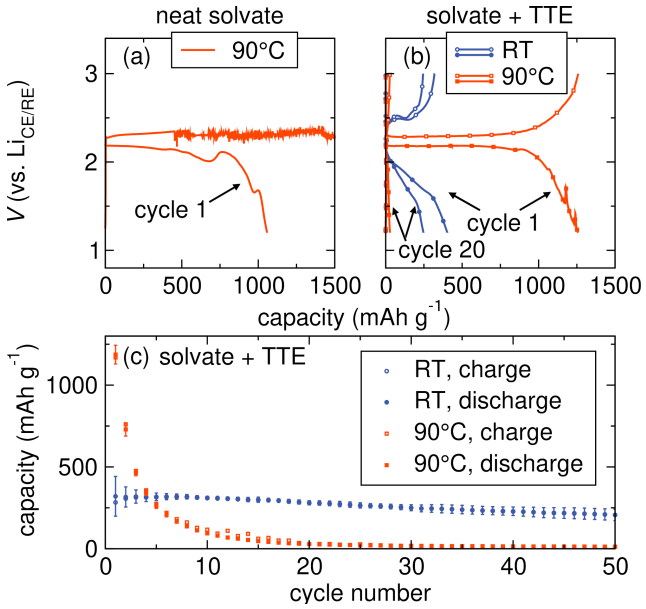

Figure 2.6: Charge and discharge profiles at various temperatures of Li-S cells prepared with (a) neat solvate electrolyte and (b) solvate + TTE electrolyte. Cells prepared with neat solvate electrolyte do not cycle at RT due to the high viscosity and low ionic conductivity of the neat solvate electrolyte. (c) Capacity fade in Li-S cells prepared with solvate + TTE electrolyte. Cells cycled at high temperatures yield higher initial capacity but more rapid capacity fade than cells cycled at RT. All cells were cycled at C/10 rate.

temperatures with TTE in the electrolyte, which could contribute to more stable charge curves.

Capacity retention changes dramatically at elevated temperature. The average discharge and charge capacity of the Li-S cells prepared with solvate + TTE electrolyte is plotted in Figure 2.6c. Li-S cells containing the neat solvate electrolyte are not shown because they do not cycle. The average capacity of three replicate cells is shown with error bars indicating the standard deviation between the replicates. Cells cycled at RT exhibit low initial discharge capacity but slow capacity fade from 320 ± 122 mAh g^{-1} to 207 ± 35 mAh g^{-1} over 50 cycles (59% capacity retention). By contrast, cells cycled at 90 °C exhibit high initial discharge capacity but rapid capacity fade to less than 10% of the average initial discharge capacity within the first eight cycles.

Several phenomena could explain the observed capacity fade at elevated temperatures. The surface film generated by reaction of TTE with the Li anode may break down upon cycling or continuously consume TTE as new Li is stripped and plated,

propagating electrolyte decomposition at the Li anode. Alternatively, the capacity fade may be due to the polysulfide shuttle effect and the loss of active material from the cathode by dissolution of soluble S reduction products. The highly concentrated solvate electrolytes (with and without TTE) are suggested to act as nonsolvents for polysulfide species at RT,[35, 41, 59] but the shift in free MeCN content at elevated temperatures may enable some polysulfide solubility. To probe polysulfide solubility at temperature, Li polysulfides dissolved in the neat solvate and solvate + TTE electrolytes were examined using UV-Visible spectroscopy (UV-Vis). The UV-Vis spectra of the electrolytes saturated with "Li_2S_6" as a function of temperature are shown in Figure 2.7a-b. The absorption peak at 261 nm is assigned to S_8 and is used for quantification of S/polysulfide solubility.[40, 41] At RT, the spectra of the neat solvate and the solvate + TTE electrolytes are very similar, suggesting similar polysulfide solubility. Upon heating, the absorption peak at 261 nm increases in the neat solvate electrolyte, whereas the solvate + TTE electrolyte shows minimal absorption at 261 nm even at 90 °C. Therefore, polysulfide solubility is higher in the neat solvate electrolyte than in solvate + TTE electrolyte at elevated temperatures.

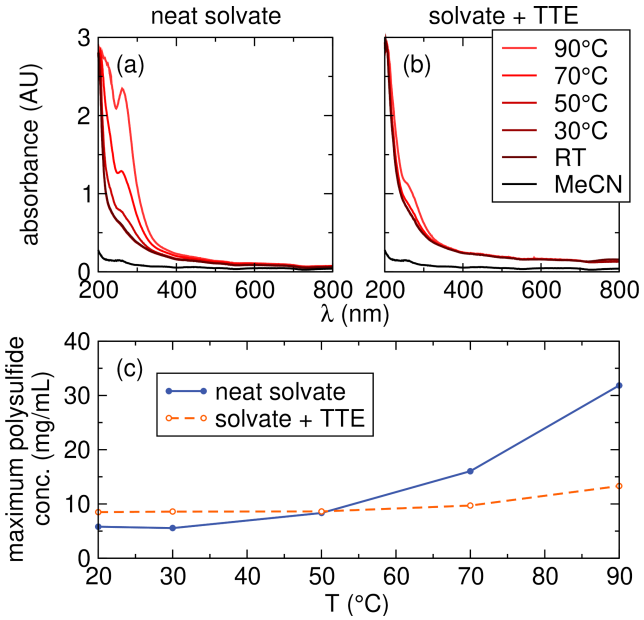

Figure 2.7: UV-Visible spectra of Li polysulfides in (a) neat solvate electrolyte and (b) solvate + TTE electrolyte as a function of temperature. (c) Polysulfide solubility remains low in the solvate + TTE electrolyte but increases with temperature, suggesting that the polysulfide shuttle may contribute to capacity fade in Li-S cells with solvate + TTE electrolyte at 90 °C.

A Beer's law standard curve was measured to quantify the concentration of Li polysulfides from the UV-Vis data. A known quantity of "Li_2S_6" was dissolved in MeCN, and spectra were collected following sequential additions of MeCN to the original solution. UV-vis spectra of the standard solutions are shown in Figure 2.8. Only the absorption peak at 261 nm appears in the spectra of polysulfides dissolved in the solvate electrolytes, but an additional peak at 612 nm was observed when Li polysulfides were dissolved in MeCN. The new absorption peak is attributed to the $S_3^{\cdot-}$ radical mode and is observed in high dielectric solvents.[40] The initial "Li_2S_6" and the resulting dissolved polysulfides are not one discrete molecule due to several disproportionation reactions that are affected by concentration and stoichiometry, so quantification using one absorption feature in the spectrum is not accurate. However, absorption at 261 nm is linear with the known S concentration in the standards. Polysulfide solubility is therefore measured from the 261 nm band and is reported here as the maximum possible concentration since the 261 nm band does not account for all Li polysulfides in the standard solutions.

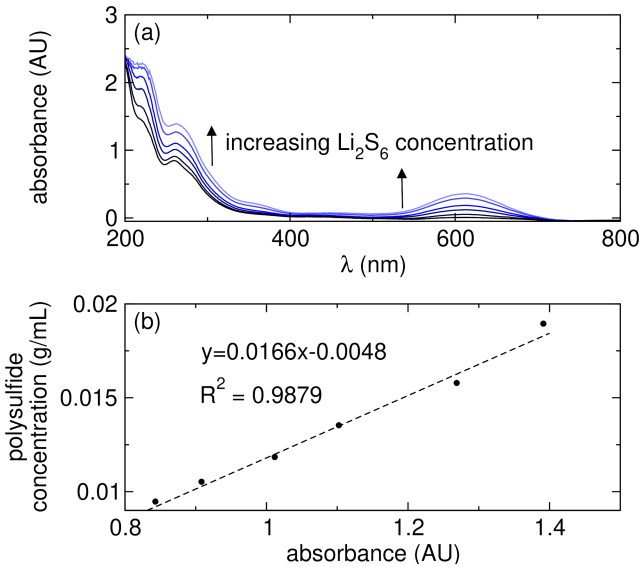

Figure 2.8: Quantification of Li polysulfides in MeCN. (a) UV-Visible spectra of Li polysulfides in MeCN at RT, with the arrow indicating increasing polysulfide concentration. Peaks corresponding to S_8 (261 nm) and $S_3^{\cdot-}$ (612 nm) are observed due to several disproportionation reactions during polysulfide dissolution. (b) The intensity of the 261 nm peak is plotted against the Li polysulfide concentration in each standard solution to derive a Beer's Law relationship.

Figure 2.7c shows the concentration of dissolved Li polysulfides in each solvate electrolyte as a function of temperature. While the maximum polysulfide concentration

in the neat solvate electrolyte steadily increases with temperature (from 6 mg/mL at RT to 32 mg/mL at 90 °C), solubility in the solvate + TTE electrolyte increases only slightly from 8 mg/mL at RT to 14 mg/mL at 90 °C. The moderate increase in Li polysulfide solubility at elevated temperatures suggests that the polysulfide shuttle effect may contribute to capacity fade in Li-S cells, in addition to capacity fade due to reactivity at the Li anode.

Effects of AlF_3 surface film on Li anode stability

To investigate the effect of the Li metal anode reactivity, we prepared a 6 nm film of AlF_3 on the Li metal surface by ALD as described previously.[44] AlF_3 may prevent Li surface reactivity by acting as a barrier to reactions between the electrolyte and Li electrode. AlF_3 surface coatings have been studied on transition metal oxide cathodes such as $LiCoO_2$ and $Li[Ni_{1/3}Mn_{1/3}Co_{1/3}]O_2$ and have been shown to deposit as uniform thin films.[60–62] AlF_3 coatings have yielded improved cycling performance on such cathode materials, particularly at high voltages, by acting as a protective coating and preventing excessive electrolyte decomposition on the electrode surface.[60, 62] AlF_3 coatings have recently been investigated on Li metal and have been shown to significantly limit MeCN decomposition at the Li/electrolyte interface and improve the cyclability of Li-S cells at RT.[44]

Figure 2.9 shows EIS spectra collected on AlF_3-coated Li | electrolyte | AlF_3-coated Li symmetric cells prepared with neat solvate and solvate + TTE electrolytes. The spectra are fit to an equivalent circuit consisting of a resistor (R_1) ascribed to the series resistance of the cells in series with RQ circuits. The spectra of cells prepared with the neat solvate electrolyte at RT are fit with two RQ circuits, similar to the EIS spectra of uncoated Li symmetric cells. The spectra of cells prepared with the neat solvate electrolyte at 90 °C are fit with one RQ circuit, since the timescale of reactivity between the electrode and electrolyte at 90 °C requires a higher cutoff frequency (*vide infra*) and the low frequency feature is not observed. The spectra of all cells prepared with solvate + TTE electrolyte are fit with three RQ circuits. The high-frequency (R_2/Q_2) and mid-frequency (R_3/Q_3) semicircles both change with time at approximately the same rate. For the sake of discussion clarity, we assign the high frequency semi-circle as the SEI. The addition of AlF_3 coincides with the appearance of a new semicircle (R_3/Q_3) that does not appear with bare Li, so R_3/Q_3 may correspond to charge transfer at the Li/AlF_3 interface. The third semicircle observed at frequencies down to 1 μHz yields constant resistance over time and is thus not considered further. The time required to measure to 1 μHz is much

longer than the timescale of reactivity between the electrode and the neat solvate electrolyte at 90 °C (*vide supra*), thus, EIS data under such conditions (Figure 2.9b) was obtained to 1 Hz and the low frequency feature(s) are not observed.

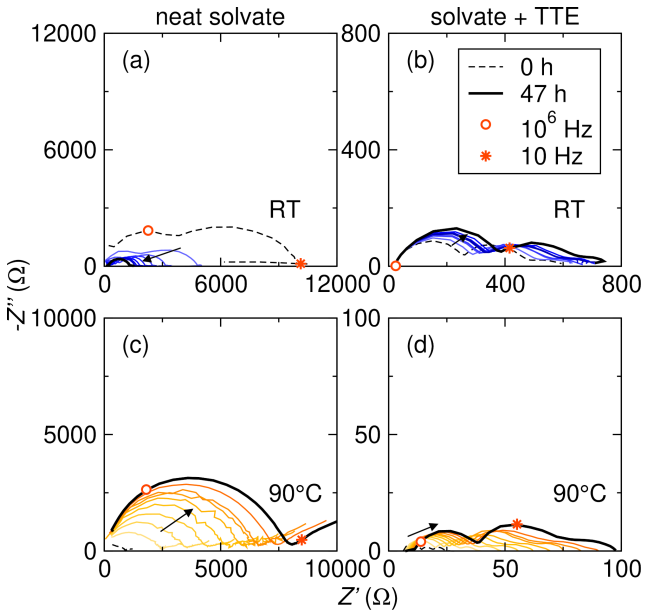

Figure 2.9: Nyquist plots of AlF_3-coated Li symmetric cells with neat solvate electrolyte at (a) room temperature (RT) and (b) 90 °C. Nyquist plots of AlF_3-coated Li symmetric cells with solvate + TTE electrolyte measured at (c) RT and (d) 90 °C. EIS data was collected from 10^6–10^{-6} Hz (a,c,d) or 10^6–1 Hz (b) at 10 points per decade, with a 10 mV amplitude, continuously for 47 h. Addition of AlF_3 coating increases overall resistance in all cases. Cells with solvate + TTE electrolyte yield lower resistances than those with neat solvate electrolyte.

Figure 2.10a shows evolution of R_2 over time in cells prepared with the neat solvate electrolyte. Three replicate cells are shown at RT and at 90 °C. Cells without TTE show significant increases in R_2 at elevated temperatures, but at RT, R_2 decreases over time. Although the exact cause for the decrease in R_2 is unknown, we hypothesize that it may be due to improved wetting of the electrode with the viscous neat solvate electrolyte over time, with possible contributions from reaction between the electrolyte and the AlF_3 coating to improve contact. Cells prepared with the neat solvate electrolyte at 90 °C yield high R_2 values that increase from 558.3 ± 342.9 Ω to 4913.3 ± 2311.8 Ω over 47 h. The high initial R_2 and increase suggest high resistivity of the AlF_3 layer and reaction of the coated Li with the neat solvate electrolyte to form a high impedance surface film.

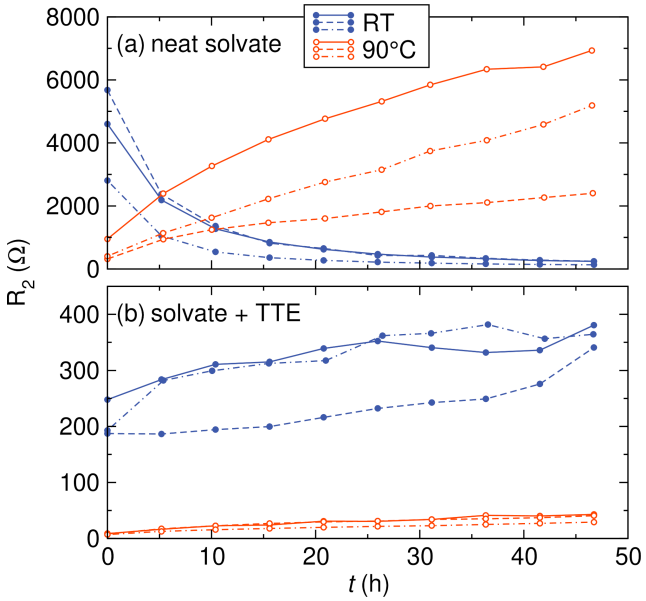

Figure 2.10: SEI resistance, R_2, extracted from the Nyquist plots of three replicate AlF_3-coated Li symmetric cells with (a) neat solvate electrolyte and (b) solvate + TTE electrolyte at room temperature (RT) and 90 °C. R_2 increases rapidly in cells with neat solvate electrolyte at 90 °C, suggesting reactivity between the electrolyte and the Li electrode. When TTE is added to the electrolyte, R_2 remains small and increases slowly over time, suggesting formation of a low impedance surface film on the Li electrode.

R_2 vs. time data for three replicate cells prepared with solvate + TTE electrolyte are shown in Figure 2.10b. Similarly to the cells prepared with uncoated Li (Figure 2.2b), cells prepared with solvate + TTE electrolyte exhibit lower R_2 values than those prepared with neat solvate electrolyte at all temperatures, likely due to improved wetting of the Celgard separator following the reduction in electrolyte viscosity upon adding TTE. Cells studied at RT exhibit a slight increase in R_2 from 209.4 ± 33.4 Ω to 358.2 ± 20.5 Ω over 47 h. The R_2 observed here is larger than that for cells prepared with uncoated Li under the same conditions (Figure 2.2b), which may be due to low ionic conductivity of the AlF_3 surface film. At 90 °C, R_2 increases from 8.0 ± 0.9 Ω to 37.6 ± 10.4 Ω. Again, the cells studied at 90 °C exhibit lower R_2 for the full 47 h duration, and the lower R_2 suggests that the presence of TTE prevents the formation of the high impedance surface film that would otherwise be generated by reaction of Li and free MeCN. The R_2 values observed at 90 °C are comparable to those in cells with uncoated Li, suggesting minimal additional stabilization of the Li/electrolyte interface from the AlF_3 layer. We therefore hy-

pothesize that the presence of TTE is the primary factor controlling the stability of the electrode/electrolyte interface.

Reactivity of the AlF_3 layer may be indicated by changes in R_3. R_3 vs. time data for three replicate cells prepared with solvate + TTE electrolyte at RT and 90 °C are shown in Figure 2.11. R_3 increases in both cases similarly to R_2. Since R_3 is only present when the AlF_3 coating is present, we assign R_3 to the AlF_3/electrolyte interface.

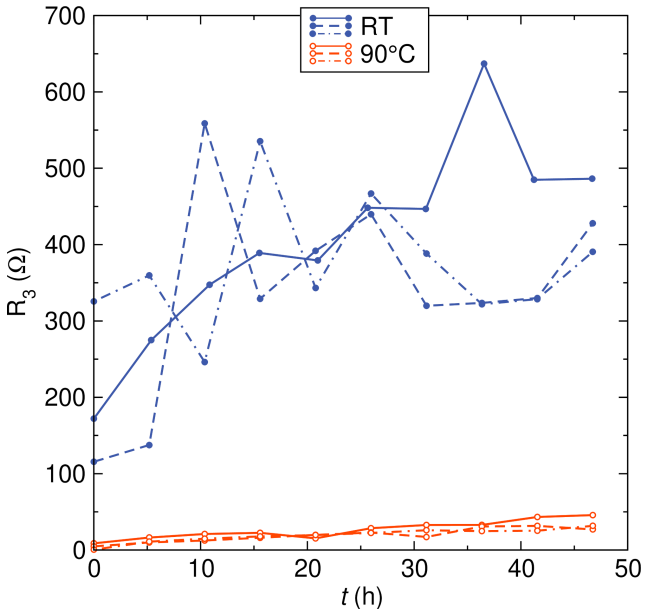

Figure 2.11: Charge transfer resistance, R_3, from the mid-frequency EIS feature of three replicate AlF_3-coated Li symmetric cells with solvate + TTE electrolyte at room temperature and 90 °C. R_3 increases at both temperatures similarly to R_2. An increase in R_3 may indicate reactivity at the Li/AlF_3 interface.

AlF_3-coated Li was assembled into Li-S cells to further evaluate the effects of AlF_3 on interfacial reactivity. The cells were first evaluated at RT and 90 °C with the neat solvate electrolyte. Figure 2.12a shows discharge and charge curves for cycles 1 and 20 of an AlF_3-coated Li-S cell prepared with neat solvate electrolyte at 90 °C. As with cells with uncoated Li, the cell at RT immediately polarized to the cutoff voltages (3 V and 1.2 V, data not shown) due to poor kinetics for interfacial charge transfer as described above. Interestingly, the AlF_3 coating enables cells prepared with the neat solvate to cycle at 90 °C beyond the first charge. Cells prepared under similar conditions with uncoated Li reproducibly failed during the first charge, as shown in Figure 2.6a. A single plateau is again observed in the discharge profile, which

may indicate a quasi-solid state S reduction mechanism rather than a conventional solvent-mediated pathway.[41, 59]

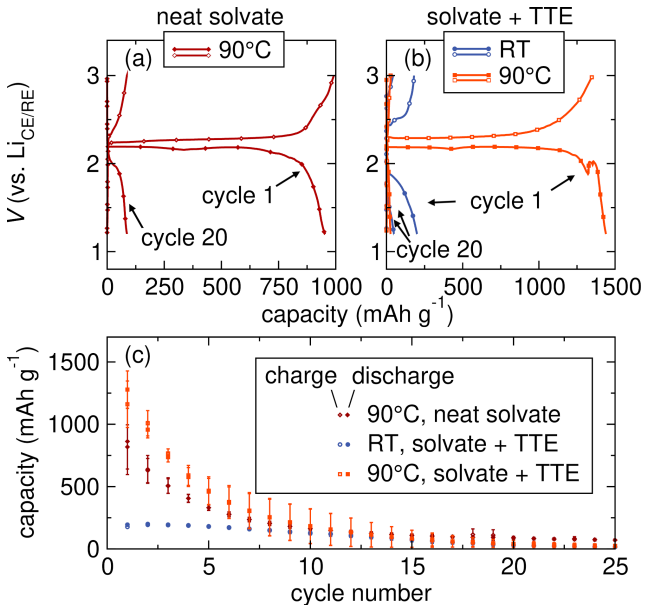

Figure 2.12: Charge and discharge profiles at various temperatures of AlF_3-coated Li-S cells prepared with (a) neat solvate electrolyte and (b) solvate + TTE electrolyte. Cells prepared with neat solvate electrolyte do not cycle at RT due to the poor kinetics of interfacial charge transfer. (c) Capacity fade in AlF_3-coated Li-S cells prepared with the neat solvate electrolyte and the solvate + TTE electrolyte. Cells cycled at high temperatures yield higher initial capacity but more rapid capacity fade than cells cycled at RT. All cells were cycled at C/10 rate.

Figure 2.12b shows discharge and charge curves for cells prepared with the solvate + TTE electrolyte. As previously demonstrated, cells cycled at RT exhibit low initial discharge capacity and sloping voltage profiles. The voltage profiles at RT are qualitatively similar to those in cells with uncoated Li but with greater polarization, which is attributed to poor kinetics imposed by the AlF_3 coating. Much greater initial discharge capacities are observed at 90 °C (1278 ± 150 mAh g^{-1}) than at RT (194 ± 9 mAh g^{-1}). Similar to the cells with uncoated Li, a single reduction plateau is observed at 90 °C, consistent with data previously reported at 55 °C.[41, 59]

The average discharge and charge capacities of the AlF_3-coated Li-S cells prepared with neat solvate electrolyte at 90 °C and with solvate + TTE electrolyte at RT and at 90 °C are shown in Figure 2.12c. The average capacities for three replicate cells are shown, with error bars indicating the standard deviation. Cells cycled at RT exhibit low initial capacity and somewhat more rapid capacity fade (to less than 10% of

the initial discharge capacity within the first twenty cycles) than cells prepared with uncoated Li (Figure 2.6c). Cells cycled at 90 °C exhibit high initial capacities with both electrolytes of 818 ± 177 mAh g^{-1} and 1278 ± 150 mAh g^{-1} for cells with neat solvate and solvate + TTE electrolyte, respectively. The capacity still fades rapidly in both cases, however, which may indicate reactivity between the AlF_3-coated Li and the solvate electrolytes as well as potential contributions from the polysulfide shuttle.

XPS was conducted on the AlF_3-coated Li before and after reaction with each solvate electrolyte at RT and 90 °C to investigate the utility of the AlF_3-coated Li at limiting decomposition reactions of the solvate electrolytes. Figure 2.13a-c shows the XPS spectra of the AlF_3-coated Li following reaction with the neat solvate electrolyte at RT. In the O region of the spectrum (Figure 2.13a), the lower BE peak at 532.3 eV is assigned to Li_2SO_4 and is likely derived from LiTFSI, similarly to the case of the uncoated Li in Figure 2.4.[49] The higher BE peak appears at 533.6 eV and is assigned to Li_2O.[50] The single peak in the N region (Figure 2.13b) appears at 400.1 eV, is assigned to adsorbed MeCN, and indicates minimal decomposition of free MeCN at RT.[51] Two peaks appear in the F region of the spectrum (Figure 2.13c). The higher BE peak at 689.2 eV is likely derived from the TFSI anion. The lower BE peak appears at 685.4 eV and is assigned to LiF.[52, 63]

Figure 2.13d shows the O region of the XPS spectrum after reaction between AlF_3-coated Li and the neat solvate electrolyte at 90 °C. A new, low BE peak appears at 531.4 eV and is assigned to Li_2CO_3, similar to the case of the uncoated Li.[49] The peaks at 532.3 eV (Li_2SO_4) and 533.6 eV (Li_2O) appear at the same BE after reaction at 90 °C as after reaction at RT.[49, 50] The presence of Li_2CO_3 suggests the formation of an insulating surface film as has been shown previously and trends similarly with the reactivity on uncoated Li shown above.[53, 54] The XPS in the N region shown in Figure 2.13e yields one peak at 399.4 eV and indicates MeCN decomposition as described for uncoated Li reacted with neat solvate at 90 °C. The F region of the spectrum in Figure 2.13f again yields two major peaks at 689.2 eV and 685.4 eV related to the TFSI anion and LiF, respectively.[52, 63] The similarities between the speciation on the surface of the uncoated and AlF_3-coated Li after reaction with the neat solvate electrolyte suggest that the AlF_3 coating provides little additional stabilization against reactions between Li metal and the neat solvate electrolyte at elevated temperature.

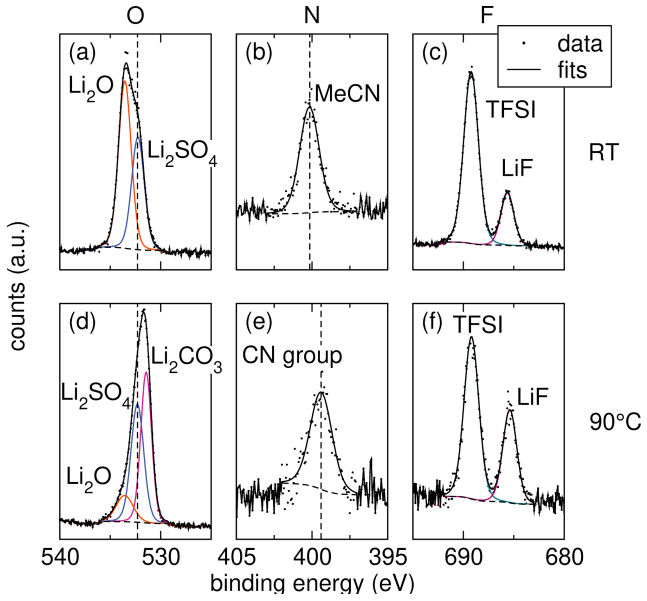

Figure 2.13: The (a) O, (b) N, and (c) F regions of the XPS spectrum of AlF_3-coated Li after exposure to neat solvate electrolyte at RT. The (d) O, (e) N, and (f) F regions of the XPS spectrum of AlF_3-coated Li metal after exposure to the neat solvate electrolyte at 90 °C. Dotted lines indicate the positions of the Li_2SO_4 and MeCN peaks and are guides for the eye. Formation of carbonate species and a shift of the CN group to lower BE at 90 °C suggests decomposition of the neat solvate electrolyte at high temperatures.

Figure 2.14a-c shows the XPS spectra of AlF_3-coated Li after reaction with the solvate + TTE electrolyte at RT. Similar to the reactions without AlF_3 coating, the O region of the spectrum yields a peak at 532.5 eV that is assigned to Li_2SO_4. The N region of the XPS spectrum yields one peak at 400.1 eV which is assigned to adsorbed MeCN.[49] The F region yields two major peaks at 689.2 eV and 685.4 eV, which are assigned to the TFSI anion and LiF, respectively, as well as a smaller peak at 685.9 eV assigned to LiF.[52, 63] The similarity to all other reactions between the solvate electrolytes and Li indicates that the AlF_3 layer does not significantly alter interactions between Li and the electrolyte at RT.

Figure 2.14d-f shows XPS of AlF_3-coated Li after reaction with the solvate + TTE electrolyte at 90 °C. The O signal still contains a peak at 532.5 eV that is assigned to Li_2SO_4. Interestingly, no new peaks appear in the O region of the spectrum at lower binding energies. Instead, a single peak appears at 533.7 eV and is assigned as Li_2O.[50] Additionally, the N region shows a single peak at 400.1 eV which is ascribed to adsorbed MeCN.[49] In all other high-temperature reactions between Li and the solvate electrolytes, the N peak shifts to lower binding energies, suggesting

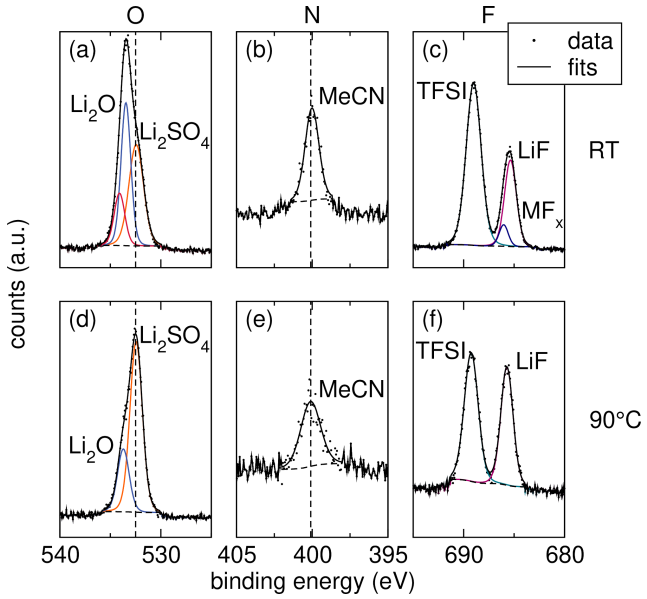

Figure 2.14: The (a) O, (b) N, and (c) F regions of the XPS spectrum of AlF_3-coated Li metal reacted with solvate + TTE electrolyte at RT. The (d) O, (e) N, and (f) F regions of the XPS spectrum of AlF_3-coated Li metal reacted with solvate + TTE electrolyte at 90 °C. Dotted lines indicate the positions of the Li_2SO_4 and MeCN peaks and are guides for the eye. The lack of carbonate species and the negligible shift in N-species BE after reaction at 90 °C suggests enhanced stability of the generated Li surface film.

some decomposition of MeCN. The lack of evidence for carbonate species and the lack of shift in N species BE signal decreased MeCN decomposition, which would lead to lower SEI resistance as shown by EIS (*vide supra*). The lack of decomposition could explain the slight increase in the initial discharge capacity in Li-S cells prepared with AlF_3-coated Li vs. with uncoated Li. Interestingly, the F region of the spectrum yields the same two peaks at 689.2 eV and 685.4 eV as in the spectrum of AlF_3-coated Li reacted with the neat solvate electrolyte at 90 °C (Figure 2.13f). In the F region of the spectrum of uncoated Li reacted with the solvate + TTE electrolyte at 90 °C (Figure 2.4f), two additional peaks appear related to TTE. The lack of such peaks in the case of AlF_3-coated Li may indicate a lesser contribution from F-containing species to the high initial discharge capacity observed in Li-S cells prepared with AlF_3-coated Li.

2.4 Conclusions

Reactivity between Li metal and the solvate electrolytes changes dramatically as a function of temperature and TTE content. Addition of TTE to the solvate electrolyte reduces polysulfide solubility even at elevated temperatures, prevents formation of a high-impedance surface film on Li metal, and leads to lower SEI resistance and greater cyclability of Li-S cells at elevated temperatures. The interfacial improvements result from reduced formation of carbonate species on the Li surface at elevated temperatures, formation of additional F-containing species on the Li surface, and decreased MeCN decomposition. The addition of 6 nm AlF_3 surface coating increases SEI resistance in all cases but enables cycling at elevated temperatures in the neat solvate electrolyte and inhibits formation of carbonate species on the Li surface in cells with solvate + TTE electrolyte. Capacity fade at elevated temperatures can likely be ascribed both to reactivity at the Li/electrolyte interface and to the polysulfide shuttle effect, enabled by higher concentrations of free MeCN at 90 °C, and remains a challenge to be addressed. The work described herein provides insight into the stability of solvate electrolytes against Li metal at elevated temperatures and highlights the need for studies examining reactivity with new electrolyte systems at both the anode and the cathode to fully understand and address failure mechanisms in Li-S batteries.

Chapter 3

ELECTROCHEMICAL PREPARATION OF SM(II) REAGENT FACILITATED BY WEAKLY COORDINATING ANIONS

Adapted from: Ware, S. D., Zhang, W., Charboneau, D. J., Klein, C. K., Reisman, S. E., See, K. A. Electrochemical Preparation of Sm(II) Reagent Facilitated by Weakly Coordinating Anions. *Chem. – Eur. J.* **2023**, 29, e202301045. DOI: 10.1002/ chem.202301045.

Abstract: Samarium diiodide (SmI_2) is widely used as a strong one-electron reducing agent and is often employed to form C–C bonds in complex systems. Despite their utility, SmI_2 and related salts suffer from several drawbacks that render the use of Sm reducing agents in large-scale synthesis impractical. Here, we report factors influencing the electrochemical reduction of Sm(III) to Sm(II), towards the goal of electrocatalytic Sm(III) reduction. We probe the effect of supporting electrolyte, electrode material, and Sm precursor on Sm(II)/(III) redox and on the reducing power of the Sm species. We find that the coordination strength of the counteranion of the Sm salt affects the reversibility and redox potential of the Sm(II)/(III) couple and establish that the counteranion primarily determines the reducibility of Sm(III). Electrochemically generated SmI_2 performs similarly to commercial SmI_2 solutions in a proof-of-concept reaction. The results will provide fundamental insight to facilitate the development of Sm-electrocatalytic reactions.

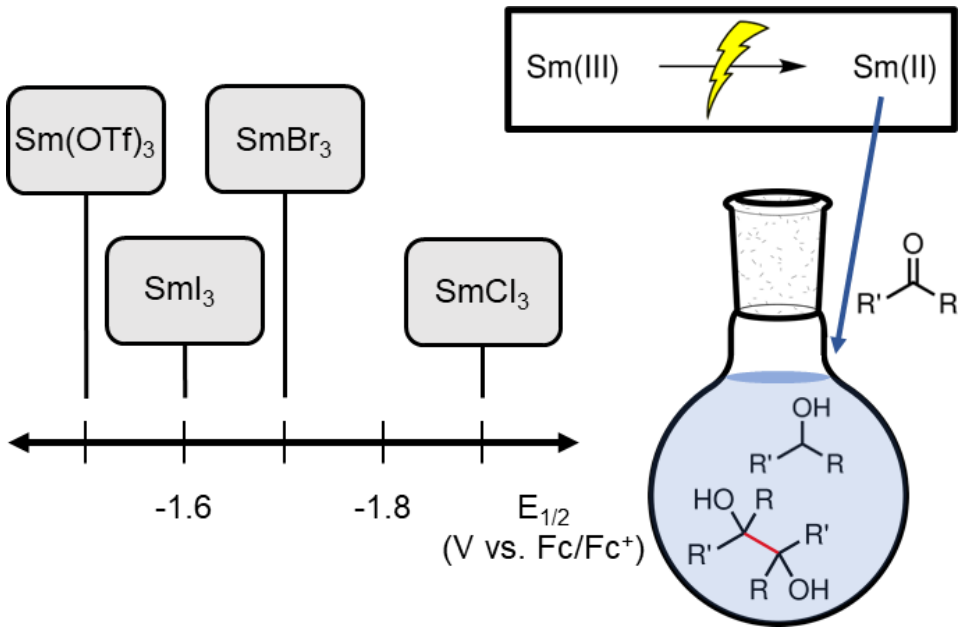

3.1 Introduction

Since its introduction to the synthetic community by Kagan and coworkers, samarium diiodide (SmI_2) has been widely used as a strong one-electron reducing agent in a broad range of synthetic organic reactions, including in the synthesis of antiviral, antibacterial, and anticancer natural products.[64–73] Despite their versatility, solutions of SmI_2 must contend with several disadvantages that limit their utility on large scale.[74] Many reactions that employ SmI_2 as a reducing agent require, at minimum, stoichiometric quantities of SmI_2 to achieve high yields. In addition to becoming prohibitively expensive at large scales, the limited solubility of SmI_2 in tetrahydrofuran (THF) requires the use of significant solvent volumes, rendering industrial-scale reactions impractical. The terminal Sm(III) byproduct is also poorly soluble in most reaction solvents, making Sm recovery or recycling efforts challenging. Furthermore, solutions of SmI_2 are unstable and have been known to precipitate SmI_x complexes over time.[74] For many applications, solutions of SmI_2 must be prepared fresh before use, adding reagent-intensive, costly, and time-consuming steps to synthetic reactions.

Many of these challenges could be addressed by developing a reaction system that is catalytic in Sm. A chemically catalytic Sm(II)/(III) system was developed for aldehyde reduction and pinacol coupling reactions by Aspinall *et al.* in 2005.[75] Though the chemically catalytic system permits a significant reduction in the quantities of SmI_2 and solvent required to achieve high yields, the additives and sacrificial reductant required to turn over Sm(III) may interfere with the primary chemistry

and limit the scope of Sm-mediated reactions. Additionally, the need for a sacrifical reductant increases the amount of chemical waste generated and results in poor atom economy for the catalytic process.

An electrocatalytic system in which the Sm(III) generated during the synthetic reaction is reduced to Sm(II) *via* electrolysis rather than by a sacrificial reductant would address many of the above challenges. An electrocatalytic process would permit low solvent volumes and catalyst loading while removing the requirement for a sacrificial reductant, which can improve the scope of the reaction and reduce the amount of chemical waste generated as compared to the chemically catalytic system. Electrochemically reducing the Sm(III) complex back to Sm(II) also provides a mechanistic handle to interrogate the mechanism of the synthetic reaction. However, the fundamental properties of electrochemical systems that enable effective and efficient Sm(III) reduction are poorly understood.

The electrochemistry of Sm complexes in solution was initially probed at elevated temperatures for Sm separation from nuclear waste[76–78] and was later studied at room temperature for organic electrosynthesis. Initial Sm-electrocatalytic systems for the bulk-scale reduction of ketones and organohalides were developed by Périchon and coworkers, but those systems relied on a sacrificial anode to support Sm(III) reduction, generating additional byproducts that can limit the scope of subsequent reactions.[67, 79–83] SmI_2 was electrochemically oxidized and reduced through cyclic voltammetry with LiI supporting electrolyte in THF by Flowers and coworkers in 2000, but the Sm redox properties were only studied from previously synthesized SmI_2 starting material and were not scaled up to synthetically relevant proportions.[84] Inspired by these initial results suggesting that Sm(II) can be electrochemically accessed from Sm(III), we aim to propose design rules for the development of Sm-electrocatalytic systems.

Previous work demonstrates that multiple factors affect the redox behavior of Sm salts in solution. Several supporting electrolytes, including ionic liquids as well as tetraalkylammonium salts in acetonitrile or THF, have been shown to support Sm(III) reduction to Sm(II). The choice of supporting electrolyte leads to shifts in the measured Sm(II)/(III) redox potential, as does the presence of strongly coordinating additives, though few general trends have been established regarding the influence of other supporting electrolyte properties on electrochemical generation of Sm(II).[76, 85–88] In addition to the supporting electrolyte, the working electrode for Sm redox also plays a role in electrochemically driven systems. In a supporting electrolyte of

0.04 M $TBAPF_6$ in THF, Mellah and coworkers found that electrochemical Sm redox was only observed at a Sm metal working electrode.[86] Other electrolyte systems permit Sm redox at a glassy C, Pt, or Hg pool electrode, but the underlying factors influencing the observed Sm redox behavior (or lack thereof) remain unclear.[76, 84, 85]

Here, we investigate the effect of the supporting electrolyte, electrode material, and Sm reagent on the efficacy and reversibility of Sm(II)/(III) redox and on the reducing power of the active Sm species. We find that the relative coordination strength of the counteranion of the Sm salt strongly affects the reversibility and potential of the Sm(II)/(III) redox couple. The coordination environment of the Sm complex can be controlled to an extent through anion exchange with the supporting electrolyte. We identify electrochemical conditions that allow for electrolytic preparation of Sm(II) from SmI_3, highlighting the ability to continuously reduce Sm(III) in solution. The electrochemically prepared Sm(II) is used in a proof-of-concept organic reaction and gives similar yields and product distributions to commercially available solutions of SmI_2, suggesting that the nature of the catalyst is not significantly altered following electrochemical generation. The results will inform efforts to develop new electrocatalytic Sm redox reactions, which have been previously limited by poor fundamental understanding of electrochemical Sm(III) reduction.

3.2 Methods

Materials Preparation

All chemicals were handled and stored in an Ar-filled glovebox unless stated otherwise. Lithium iodide (LiI, 99.9%, Sigma-Aldrich), lithium bis(trifluoromethanesulfonyl)imide (LiTFSI, 99.95%, Sigma-Aldrich), lithium chloride (LiCl, 99%, Sigma-Aldrich), and lithium bromide (LiBr, >99%, Sigma-Aldrich) were dried at 110°C under vacuum overnight before use. Tetrahydrofuran (THF, >99.9%, Fisher Scientific) was dried on a solvent purification system (Pure Process Technologies) and transferred to the glovebox without exposure to air. Tetrabutylammonium hexafluorophosphate ($TBAPF_6$, >99%, Sigma-Aldrich) was recrystallized from ethyl acetate (99.8%, Sigma-Aldrich) in air before transferring to the glovebox. Benzylacetone (98%, Combiblocks) and triethylamine (99+%, Fisher Scientific) were distilled prior to use. All other chemicals were used without further purification.

All electrolytes were prepared in an Ar-filled glovebox. Solutions containing SmI_2 were prepared by diluting a commercial solution of SmI_2 in THF (Thermo Scientific), adding the chosen supporting electrolyte salt, and stirring until fully dissolved to yield a dark blue solution. All electrolytes containing SmI_2 or LiI were prepared in the dark and the vials wrapped in Al foil to minimize light-induced degradation. SmI_3 was synthesized *in situ* for cyclic voltammetry (CV) experiments by combining samarium(III) triflate ($Sm(OTf)_3$, 98%, Sigma Aldrich) and LiI in THF. SmI_3 was synthesized *in situ* for bulk electrolysis experiments by combining SmI_2 solution and 0.5 equivalents of solid I_2 (>99.99%, Alfa Aesar).

Electrochemical Testing

All electrochemical experiments were conducted on a VMP3 potentiostat (Bio-Logic) in an Ar-filled glovebox. All CV experiments were conducted in a 10 mL glass three-electrode cell (Pine Research Instrumentation) with a gas-tight PEEK cap. Unless otherwise stated, a polished glassy carbon disk (3.0 mm O.D., Pine) was used as the working electrode, Pt wire (Pine) was used as the counter electrode, and Ag wire (Pine) was used as a pseudo-reference electrode. Sm(II)/(III) redox couples studied with LiI supporting electrolyte were referenced to ferrocene/ferrocenium (Fc/Fc^+) by first referencing to bis(benzene)chromium (97%, Sigma Aldrich) via CV, then calculating the potential difference from Fc/Fc^+[89]. Sm(II)/(III) redox couoples studied with all other supporting electrolytes were referenced to Fc/Fc^+ via CV. All peaks were analyzed and baseline subtracted using EC-Lab fitting software (Bio-Logic). All bulk electrolysis experiments were conducted in a 20 mL divided cell (Pine) equipped with a fritted glass separator. The counter electrode was separated from the working and reference electrodes to prevent consumption of the reduced Sm product. A polished glassy carbon plate (Sigma-Aldrich) was used as the working electrode, Pt mesh (BASi) was used as the counter electrode, and Ag wire (Pine) was used as the reference electrode. The electrolyte was stirred in both compartments to facilitate transport of the active species to the electrode surface.

Sample Characterization

UV-Visible (UV-Vis) spectra were collected on a Cary 500 UV-Vis-NIR spectrometer in a screw-cap cuvette. All samples were prepared in a glovebox and transferred to the instrument without exposure to air. A THF background was subtracted from all spectra.

Titration of commercial and electrogenerated solutions of SmI_2 was performed as reported previously.[90] Briefly, 1 mL SmI_2 solution in THF (1 equiv.), 7.2 μL H_2O (4 equiv.), and 41.8 μL triethylamine (3 equiv.) were combined to yield a dark green solution. A separate solution of 0.05 M 2-heptanone in THF was added dropwise to the SmI_2 solution until the dark green solution turned colorless.

Nuclear magnetic resonance (NMR) spectra were recorded on a Varian Inova 500 MHz spectrometer. ^{1}H-NMR data is referenced to the phenyl proton of the internal standard 1,3,5-trimethoxybenzene (1H, δ = 6.08 ppm).[91] The reduction of benzylacetone by SmI_2 was performed as follows: to an oven-dried opaque 20 mL vial equipped with a stir bar were added benzylacetone (0.05 mmol, 1 eq.) and SmI_2 solution in THF (0.10 mmol SmI_2, 2 eq., either commercial or eletrogenerated). Some reaction conditions tested included water (0.4 mmol, 8 eq.) and triethylamine (0.3 mmol, 6 eq.). The reaction was allowed to stir at room temperature under N_2 overnight. The resulting reaction mixture was quenched with 1 M aqueous HCl and extracted thrice with dichloromethane (DCM, 99.9%, Fisher Scientific). The internal standard was added to the combined organic layers. The resulting solution was dried over magnesium sulfate ($MgSO_4$, >99%, Fisher Scientific), filtered through a cotton plug, concentrated under vacuum, and diluted in deuterated chloroform ($CDCl_3$, 99.8%, Cambridge Isotope Labs). The solution was analyzed with ^{1}H-NMR, and the spectral data matched those reported in the literature.[92–94]

3.3 Results and Discussion

Effect of supporting electrolyte and working electrode on Sm redox

To gain a baseline understanding of the properties that influence electrochemically driven Sm redox, we first investigate the redox behavior of SmI_2 in a supporting electrolyte of 0.5 M LiI in THF using cyclic voltammetry (CV). This electrolyte was first demonstrated to support Sm redox by the Flowers group in 2000.[84] CVs of 5 mM SmI_2 at varying scan rates are shown in Figure 3.1a. The CVs of SmI_2 with LiI supporting electrolyte show coupled oxidative and reductive waves that scale directly with scan rate. The Sm redox couple exhibits wide peak splitting that increases as the scan rate is increased. The peak splitting cannot be attributed solely to the supporting electrolyte resistance. CVs collected with IR compensation (Figure 3.2) still exhibit peak splitting larger than the approx. 60 mV that would be expected for a reversible one-electron redox couple. Therefore, we attribute the

peak splitting to irreversible electron transfer kinetics. The slow electron transfer kinetics are likely attributable to the large reorganization energy about the Sm center following reduction or oxidation, induced by changes in the Sm-I bond length and the Sm coordination geometry.[95–97]

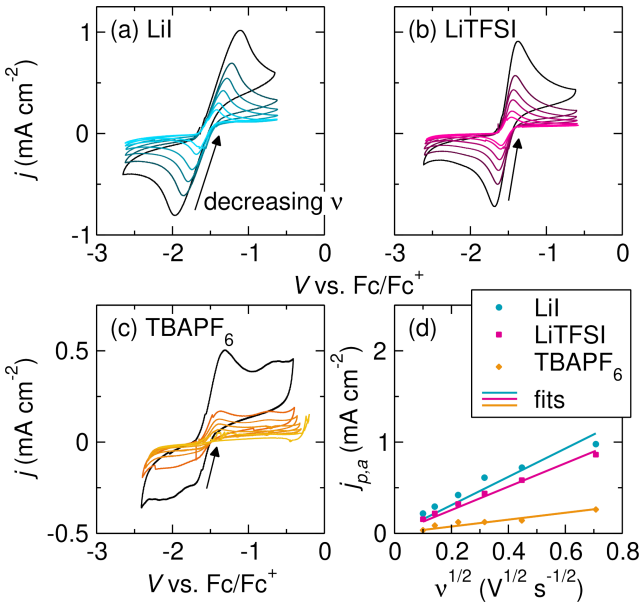

Figure 3.1: CVs of 5 mM SmI_2 with (a) 0.5 M LiI, (b) 0.5 M LiTFSI, and (c) 0.5 M $TBAPF_6$ supporting electrolytes in THF. Scan rates (ν) of 500, 200, 100, 50, 20, and 10 mV s^{-1} are shown. (d) Plot of peak current density, $j_{p,a}$, vs. $\nu^{1/2}$ for each supporting electrolyte. High SmI_2 diffusion coefficients with LiI and LiTFSI supporting electrolytes mitigate diffusion limitations in long-term experiments, leading to more facile reduction of Sm(III).

The supporting electrolyte influences the redox properties of SmI_2 in solution. Supporting electrolytes with larger ions have been suggested to prevent aggregation of SmI_2 in solution and enable more facile Sm redox.[98] Previous studies of the redox behavior of lanthanide complexes at room temperature employed ionic liquids containing the bistriflimide anion ($TFSI^-$) due to their wide electrochemical stability window.[76] A solution of 0.5 M LiTFSI in THF is used here to assess the effect of a large supporting electrolyte anion on the redox behavior of SmI_2. CVs of 5 mM SmI_2 with LiTFSI supporting electrolyte are shown in Figure 3.1b. Coupled features attributable to Sm redox are observed, with similar peak current densities to the voltammograms collected with LiI supporting electrolyte. The peak splitting is slightly smaller than that from SmI_2 with LiI supporting electrolyte, suggesting a lower kinetic barrier to redox and possibly indicating that the larger supporting

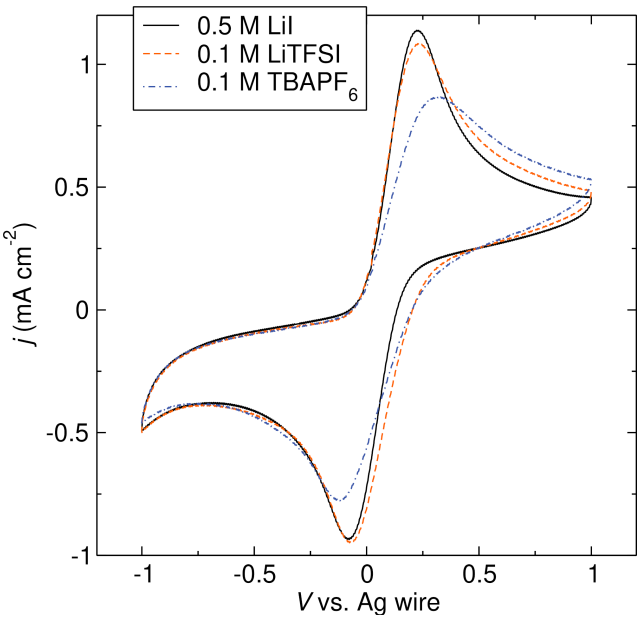

Figure 3.2: CVs of 5 mM SmI_2 with (a) 0.5 M LiI, (b) 0.1 M LiTFSI, and (c) 0.1 M $TBAPF_6$ supporting electrolytes with IR compensation. While the peak splitting in each case decreases relative to CVs collected without IR compensation, the peak splitting is still much larger than the 57 mV that would be expected for a reversible one-electron redox couple. Therefore, the electrochemical irreversibility and slow electron transfer kinetics are not attributable solely to the electrolyte resistance.

electrolyte anion may prevent some aggregation of SmI_2 in solution. The peak splitting is still larger than that expected for an electrochemically reversible redox couple.

To determine whether an additional benefit can be gained from employing both a large anion and a large cation, tetrabutylammonium hexafluorophosphate ($TBAPF_6$) is also tested as a supporting electrolyte. $TBAPF_6$ is often used as a supporting electrolyte for electrochemical reactions in organic synthesis due to its wide electrochemical stability window and low reactivity against common organic compounds.[86, 99, 100] CVs of 5 mM SmI_2 with 0.5 M $TBAPF_6$ supporting electrolyte in THF are shown in Figure 3.1c. A clear oxidative wave is observed at high scan rates, but the corresponding reductive wave is poorly resolved. The peak current densities are additionally smaller than those in LiI or LiTFSI supporting electrolytes, indicating less favorable redox activity. At low scan rates, the redox couple becomes fully irreversible, indicating decomposition or side reactions between SmI_2 and $TBAPF_6$. A solution of 5 mM SmI_2 + 0.1 M $TBAPF_6$ in THF bleaches over approximately three hours even when kept in the dark, suggesting that the reaction

is neither related to I^--derived photodecomposition nor induced by direct electrochemical transformation. Images of the SmI_2/$TBAPF_6$ electrolyte at various time points are shown in Figure 3.3. Possible side reactions include F^--abstraction by SmI_2 or hydrolysis of the PF_6^- anion by trace water to form free F^- and subsequent generation of electrochemically inert SmF_3.

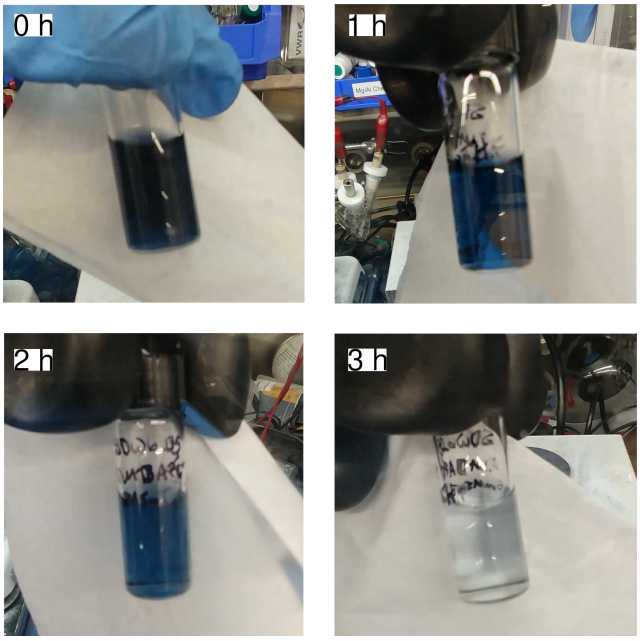

Figure 3.3: Images of a solution of 5 mM SmI_2 + 0.1 M $TBAPF_6$ in THF (a) immediately after SmI_2 addition, (b) 1 h after SmI_2 addition, (c) 2 h after SmI_2 addition, and (d) 3 h after SmI_2 addition. The solution bleaches over the course of 3 h, possibly due to formation of SmF_x species following hydrolysis of the PF_6^- anion after reaction with trace water.

The diffusion coefficient of the Sm complex in each supporting electrolyte can be estimated from the CVs following the equation $j_p = (2.99 \times 10^5)\alpha^{1/2}D_O^{1/2}C_O{*}\nu^{1/2}$, where j_p is the peak current density, α is the transfer coefficient, D_O is the diffusion coefficient, $C_O{*}$ is the starting Sm concentration, and ν is the scan rate. Calculations of the transfer coefficient for LiI and LiTFSI supporting electrolytes are shown in Figure 3.4 and for $TBAPF_6$ in Table 3.1). The peak oxidative current is plotted vs. the square root of scan rate for each supporting electrolyte in Figure 3.1d. The LiI supporting electrolyte yields the highest Sm diffusion coefficient of 8.5 $\times$ 10^{-6} cm^2s^{-1}, followed by LiTFSI and $TBAPF_6$ (1.3 $\times$ 10^{-6} cm^2s^{-1} and 1.8 $\times$ 10^{-7} cm^2s^{-1}, respectively). The high diffusion coefficients provided by the LiI and LiTFSI supporting electrolytes mitigate diffusion limitations in long-term experiments, leading to more facile reduction of Sm(III).

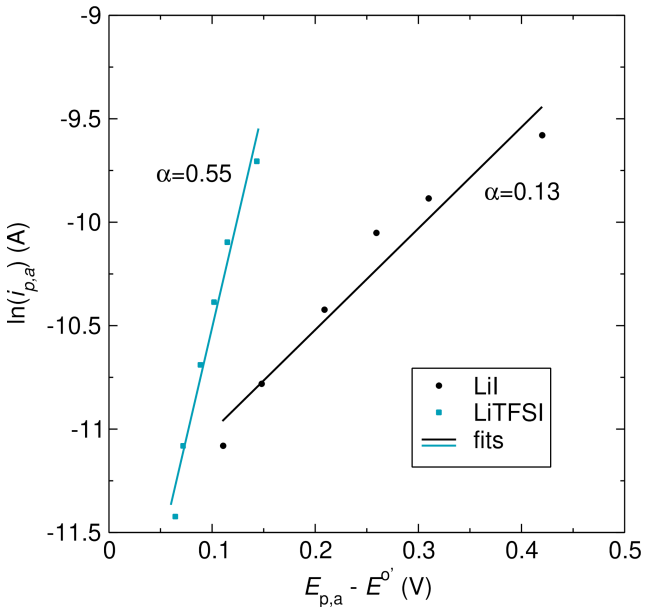

Figure 3.4: Plot of ln($i_{p,a}$) vs. $E_{p,a}$-$E^{o'}$ from CVs of 5 mM SmI_2 with LiI or LiTFSI supporting electrolytes at scan rates of 500, 200, 100, 50, 20, and 10 mV/s. The transfer coefficient α can be calculated from the equation $j_p = 0.227FC_O{*}k^0\exp[-\alpha F(E_p\text{-}E^{o'})/RT]$, where j_p is the peak current density, C_O* is the starting Sm concentration, k^0 is the heterogeneous rate constant, α is the transfer coefficient, F is the Faraday constant, R is the ideal gas constant, T is temperature, E_p is the peak potential, and $E^{o'}$ is the formal potential of the Sm(II)/(III) redox couple.

scan rate (mV/s)	E_p-$E_{p/2}$ (V)	α
500	0.151	0.317
200	0.157	0.304
100	0.121	0.395
50	0.136	0.351
20	0.125	0.381
10	0.126	0.379

Table 3.1: Estimation of α from CVs of 5 mM SmI_2 with $TBAPF_6$ supporting electrolyte at various scan rates. Since $E^{o'}$ cannot be determined with $TBAPF_6$ supporting electrolyte, α can be estimated from the equation $|E_p\text{-}E_{p/2}| = 1.857RT/\alpha F$, where $E_{p/2}$ is the potential where the current is half the peak value and all other variables are as defined above. An average α value of 0.35 was used for D_O calculations.

The peak current also scales with SmI_2 concentration for all supporting electrolytes. CVs of SmI_2 at various concentrations (10, 5, 2, and 1 mM) with 0.5 M LiI supporting electrolyte are shown in Figure 3.5a. The peak oxidative and reductive current

both decrease as concentration decreases, with no change in the reversibility of the redox couple. CVs of SmI_2 at the above concentrations with 0.5 M LiTFSI supporting electrolyte are shown in Figure 3.5b. Similar behavior is observed in LiTFSI supporting electrolyte, but the redox couple is poorly resolved at low concentrations (1 mM SmI_2). CVs of SmI_2 at the above concentrations with 0.5 M $TBAPF_6$ supporting electrolyte are shown in Figure 3.5c. While both the oxidative and reductive wave are observed for the 10 mM SmI_2 electrolyte, the irreversibility of the SmI_2 redox couple is preserved at all concentrations below 10 mM, and the reductive peak current disappears with decreasing SmI_2 concentration. A plot of peak oxidative current density vs. SmI_2 concentration in all three supporting electrolytes is presented in Figure 3.5d. The peak current density increases monotonically in all three supporting electrolytes, but the oxidative and reductive peak currents are higher when using the LiI or LiTFSI supporting electrolyte as compared to the $TBAPF_6$ supporting electrolyte, and the LiI supporting electrolyte supports the greatest Sm redox current at low concentrations. Based on the high diffusion coefficients and the linear and monotonic concentration profiles, we conclude that both LiI and LiTFSI supporting electrolytes promote Sm redox. The Sm redox performance is best with LiI supporting electrolyte, particularly at low concentrations.

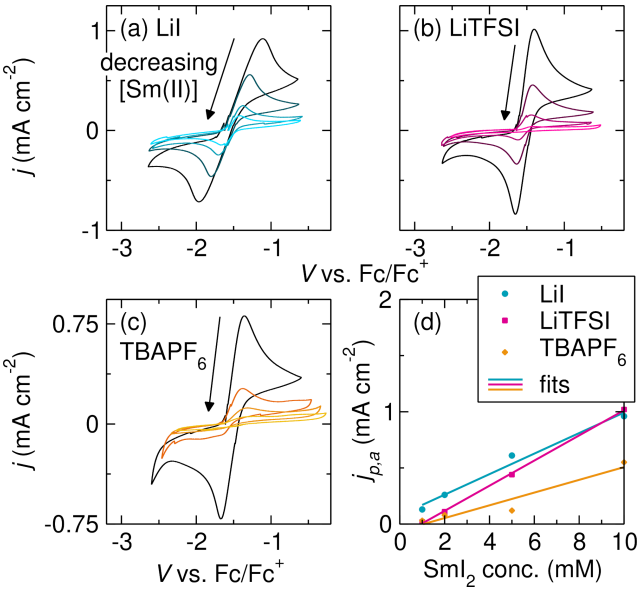

Figure 3.5: CVs of SmI_2 at various concentrations (10, 5, 2, and 1 mM) with (a) 0.5 M LiI, (b) 0.5 M LiTFSI, and (c) 0.5 M $TBAPF_6$ supporting electrolyte. All voltammograms are collected at a scan rate of 100 mV s^{-1}. (d) Plot of peak current density, $j_{p,a}$, vs. SmI_2 concentration for each supporting electrolyte.

Several working electrodes are examined in the three supporting electrolytes discussed above. The results of the working electrode studies are shown in Figure 3.6. While a glassy carbon working electrode enables Sm redox with all three supporting electrolytes, Sm redox at a Au working electrode is only observed with the LiTFSI supporting electrolyte, and Sm redox at a Pt working electrode is only observed with the $TBAPF_6$ supporting electrolyte. Because glassy carbon permits Sm redox in multiple supporting electrolytes, a glassy carbon working electrode is used for all further experiments. Although the exact reason for the greater efficacy of the glassy carbon working electrode is difficult to ascertain directly, we hypothesize that the presence of C=O groups on the glassy carbon surface may promote Sm redox, as previously shown for Eu(II)/(III).[101]

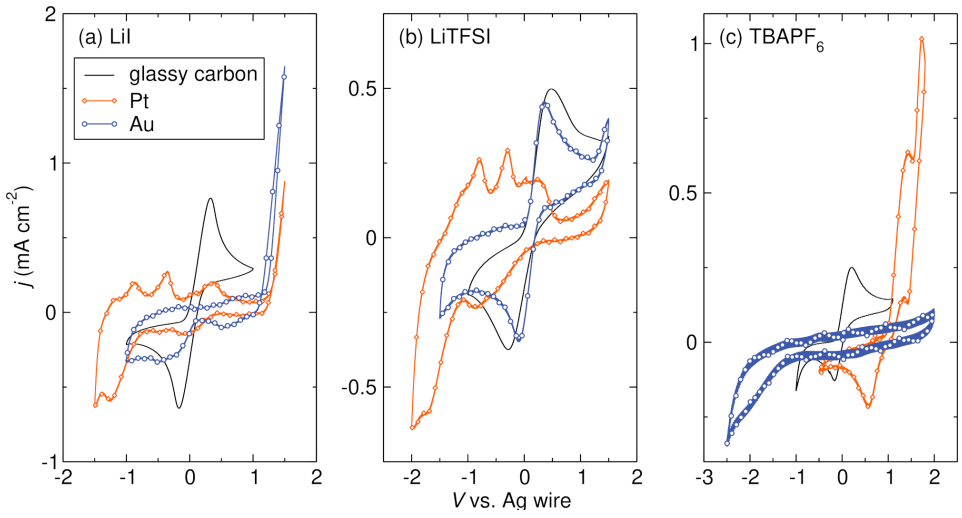

Figure 3.6: CVs of SmI_2 with (a) 0.5 M LiI, (b) 0.1 M LiTFSI, and (c) 0.1 M $TBAPF_6$ supporting electrolytes on glassy C, Au, and Pt working electrodes. While Sm redox behavior is observed on Au electrodes with LiTFSI supporting electrolyte and on Pt electrodes with $TBAPF_6$ supporting electrolyte, glassy carbon electrodes yield the best performance in all supporting electrolytes.

Effect of counteranion on Sm redox

The counteranion of the Sm species strongly influences the potential of the Sm redox couple. For instance, $SmCl_2$ and $SmBr_2$ are known to be stronger reducing agents than SmI_2 and can therefore chemically reduce different species in solution.[102] To probe the effect of the counteranion on the electrochemical reversibility of the Sm redox couple, $SmCl_2$ is generated from SmI_2 and excess LiCl. SmI_2 and LiCl are known to undergo anion exchange to form $SmCl_2$ in solution.[102] Figure 3.7a shows the CV of SmI_2 with 0.5 M LiCl supporting electrolytes. Contrary to CVs with

LiI supporting electrolyte, no redox peaks are observed with the LiCl supporting electrolyte. UV-Visible (UV-Vis) spectroscopy confirms anion exchange between the SmI_2 starting material and the LiCl supporting electrolyte (Figure 3.7b). Some reactivity is apparent after 5 minutes, as seen from the blue-shift in absorbance values of the two peaks between 500 nm and 700 nm. After two hours, the SmI_2 is fully converted to $SmCl_2$ and the peak at 550 nm disappears entirely.

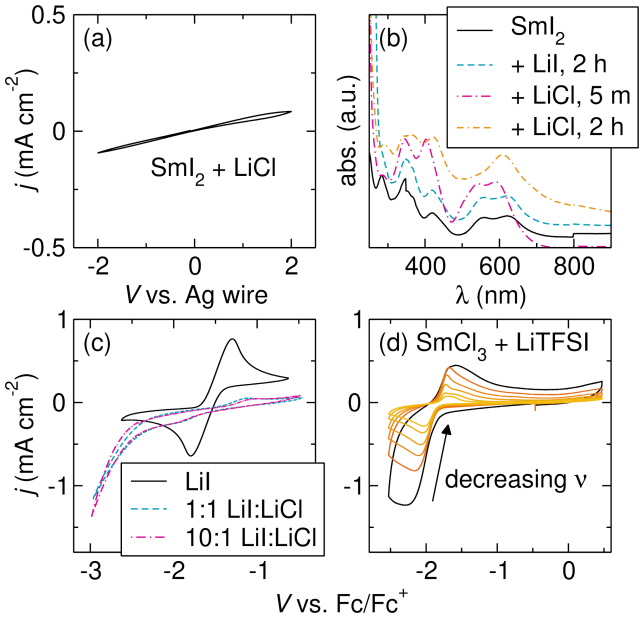

Figure 3.7: Sm redox activity in the presence of Cl^- anions. (a) CV of SmI_2 with 0.5 M LiCl supporting electrolyte. No Sm redox activity is observed in the LiCl supporting electrolyte. (b) UV-Vis spectra of SmI_2 with LiI and LiCl supporting electrolytes collected at various times after Li salt addition. A distinct change in the spectrum after addition of LiCl indicates anion exchange between SmI_2 and LiCl. (c) CVs of SmI_2 with mixed LiI/LiCl supporting electrolyte. The electrolyte ionic strength was kept constant at 0.5 M. Addition of any LiCl to the supporting electrolyte precludes Sm redox. All voltammograms in panels a-c were collected at 100 mV s^{-1}. (d) CVs of $SmCl_3$ with 0.5 M LiTFSI supporting electrolyte. Scan rates (ν) of 500, 200, 100, 50, 20, and 10 mV s^{-1} are shown.

The supporting electrolyte composition is varied to further probe whether the loss of redox activity is due to inherent challenges with the LiCl supporting electrolyte or to the difficulty of electrochemically reducing $SmCl_2$. Figure 3.7c shows CVs of SmI_2 with mixed LiI/LiCl supporting electrolyte. The ionic strength of the supporting electrolyte is kept constant at 0.5 M, but the ratio of LiI to LiCl is varied to assess the effect of the LiCl supporting electrolyte. Even at a LiI:LiCl ratio of 10:1, minimal

redox activity is observed, indicating that the loss of redox activity in LiCl supporting electrolyte is primarily due to the difficulty of oxidizing and reducing $SmCl_x$ rather than to challenges with the LiCl supporting electrolyte, such as low conductivity. To further confirm this hypothesis, CVs of commercially available $SmCl_3$ are collected with 0.5 M LiI in THF as the supporting electrolyte (Figure 3.8). No Sm redox is observed within the electrochemical stability window of the electrolyte, confirming that $SmCl_x$ species are much more difficult to reduce than SmI_x species. Redox features attributable to $SmCl_3$ are only observed when the supporting electrolyte is changed to 0.5 M LiTFSI, suggesting that more facile electrochemical redox is enabled by larger supporting electrolyte anions (Figure 3.7d). The $SmCl_3$ redox potential lies at –1.9 V vs. Fc/Fc^+.

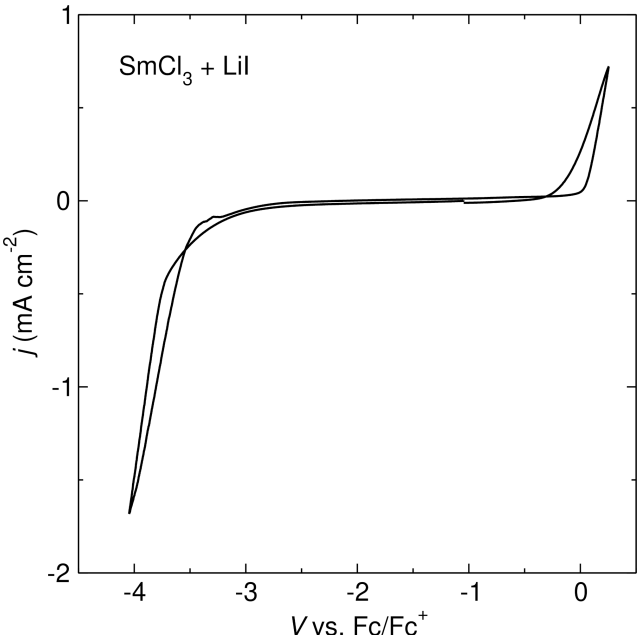

Figure 3.8: CV of 10 mM $SmCl_3$ with 0.5 M LiI supporting electrolyte. No Sm redox behavior is observed in the LiI supporting electrolyte. Redox from $SmCl_3$ is only observed with LiTFSI supporting electrolyte, suggesting more facile redox enabled by the larger supporting electrolyte anions.

In addition to $SmCl_3$, samarium(III) acetylacetonate ($Sm(acac)_3$) is studied to verify the hypothesis that Sm complexes with more strongly coordinating anions are more difficult to reduce. Redox on $Sm(acac)_3$ is attempted with LiI, LiTFSI, and $TBAPF_6$ supporting electrolytes. The CVs are shown in Figure 3.9. No redox features are observed within the electrochemical stability window of any of the supporting electrolytes tested, suggesting that the strong anion coordination limits Sm redox in solution.

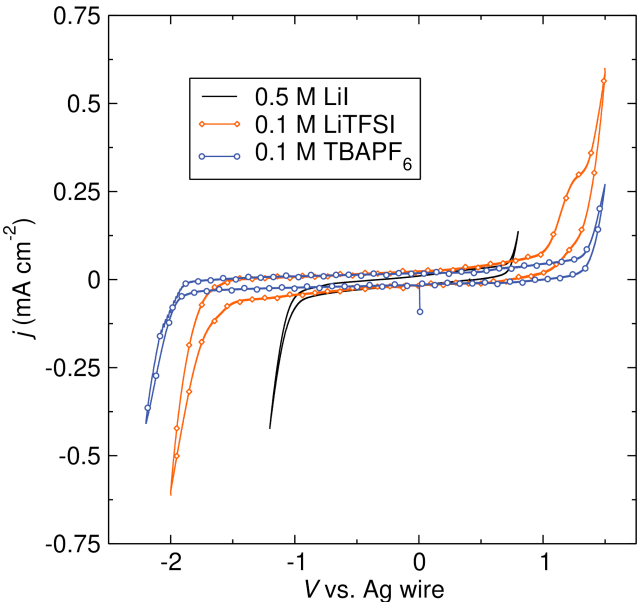

Figure 3.9: CVs of 10 mM $Sm(acac)_3$ with 0.5 M LiI, 0.1 M LiTFSI, and 0.1 M $TBAPF_6$ supporting electrolytes. No Sm redox behavior is observed in any of the supporting electrolytes, likely due to the strong coordination of the acetylacetonate ligand.

Sm(III) salts with more weakly coordinating anions than Cl^- are examined to probe the effect of the counteranion properties on the Sm redox potential. The more weakly coordinating anions may, to some extent, remain within the primary coordination sphere of the Sm cation, but they can be displaced more easily upon reaction with more strongly coordinating anions or reduction of the Sm cation.[103–108] Figure 3.10a shows CVs of commercially available $Sm(OTf)_3$ with 0.5 M LiTFSI supporting electrolyte. Coupled oxidative and reductive features are observed, indicating that $Sm(OTf)_3$ can be electrochemically oxidized and reduced at mild potentials. Coordinative stabilization by the OTf^- anion may contribute to the more mild reduction potential of $Sm(OTf)_3$.[103] The Sm redox couple exhibits large peak splitting of > 1 V and low peak currents, and the ratio of $i_{p,c}$:$i_{p,a}$ is greater than 1, suggesting that this $Sm(OTf)_3$/LiTFSI redox system is not electrochemically reversible.

Figure 3.10b shows CVs of 10 mM $SmBr_3$ with 0.5 M LiTFSI supporting electrolyte. The Sm redox couple is subject to a high kinetic barrier, as shown by the large peak splitting and the change in peak splitting as a function of scan rate. The peak splitting is much smaller for $SmBr_3$ than for $Sm(OTf)_3$, suggesting a more reversible redox

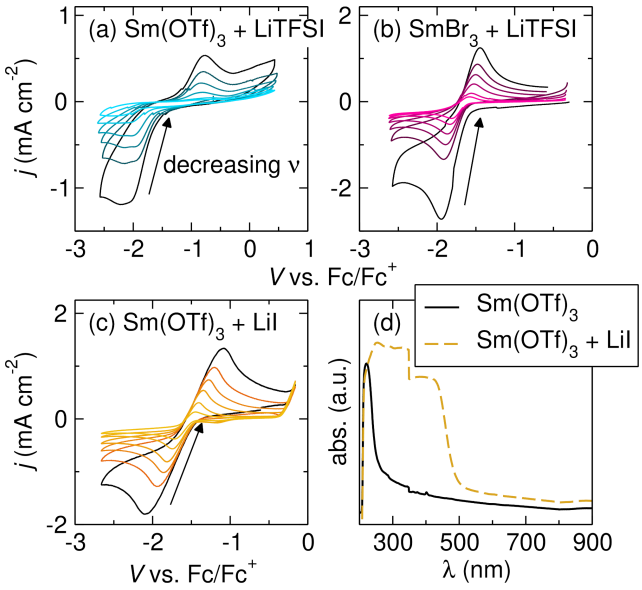

Figure 3.10: CVs of (a) 10 mM $Sm(OTf)_3$ with 0.5 M LiTFSI supporting electrolyte, (b) 10 mM $SmBr_3$ with 0.5 M LiTFSI supporting electrolyte, and (c) 10 mM SmI_3, formed *in situ* from anion exchange between $Sm(OTf)_3$ and LiI, with 0.5 M LiI supporting electrolyte. Scan rates (ν) of 500, 200, 100, 50, 20, and 10 mV s^{-1} are shown. (d) UV-Vis spectra confirming formation of SmI_3 from anion exchange between $Sm(OTf)_3$ and LiI. $SmBr_3$ and SmI_3 redox exhibit the smallest peak splitting, suggesting more electrochemically reversible redox couples.

couple. The ratio of $i_{p,c}$:$i_{p,a}$ is again greater than 1, however, suggesting that redox on $SmBr_3$ is not entirely reversible.

A 10 mM solution of SmI_3 is generated via anion exchange between $Sm(OTf)_3$ and excess LiI, as the more strongly coordinating I^- can replace the more weakly coordinating OTf^- similarly to the preparation of $SmCl_2$ described above. Formation of SmI_3 is confirmed by UV-Vis spectroscopy and by an immediate color change from colorless to yellow upon addition of LiI (Figure 3.10d). Figure 3.10c shows CVs of this *in situ*-prepared 10 mM SmI_3 with 0.5 M LiI supporting electrolyte. Coupled redox features are observed, indicating that the SmI_3 starting material can be electrochemically reduced to SmI_2 in LiI supporting electrolyte. The peak splitting is again smaller for SmI_3 than for $Sm(OTf)_3$, suggesting a more reversible redox couple. The ratio of $i_{p,c}$:$i_{p,a}$ is approximately 1, indicating a more electrochemically reversible redox couple than either $SmBr_3$ or $Sm(OTf)_3$.

The equilibrium potentials of each Sm redox couple are summarized in Table 3.2. The equilibrium potential of Sm redox shifts as a function of the coordination

strength of the anion. When referenced to a ferrocene/ferrocenium (Fc/Fc^+) internal reference couple, the Sm redox potential becomes increasingly negative as the relative anion coordination strength increases. The $E^{o'}$ of the Sm(II)/Sm(III) redox couple shifts from –1.5 V vs. Fc/Fc^+ when measured using a $Sm(OTf)_3$ salt to –1.6 V vs. Fc/Fc^+, –1.7 V vs. Fc/Fc^+, and finally –1.9 V vs. Fc/Fc^+ using SmI_3, $SmBr_3$, and $SmCl_3$, respectively. We find that the coordination strength of the counteranion in the Sm salt thus provides a handle to tune the reducing power of the Sm electrocatalyst, which is consistent with prior work investigating the influence of halide salts on SmI_2 reduction.[84, 102, 109]

Sm salt	Supp. electrolyte	$E^{o'}$ (V vs. Fc/Fc^+)
SmI_2	0.5 M LiI	-1.5 V
SmI_2	0.5 M LiTFSI	-1.5 V
SmI_2	0.5 M $TBAPF_6$	-1.5 V
SmI_2	0.5 M LiCl	--
$SmCl_3$	0.5 M LiI	--
$Sm(OTf)_3$	0.5 M LiTFSI	-1.5 V
SmI_3	0.5 M LiI	-1.6 V
$SmBr_3$	0.5 M LiTFSI	-1.7 V
$SmCl_3$	0.5 M LiTFSI	-1.9 V

Table 3.2: Potentials of Sm(II)/(III) redox measured by CV using various Sm salts and supporting electrolytes.

Bulk synthesis of SmI_2 and application to organic synthesis

Using our knowledge of the effect of electrolyte composition on Sm redox behavior, we next aim to assess our ability to continuously reduce Sm(III) to Sm(II). The electrochemical reduction of Sm(III) to Sm(II) is studied at bulk scale using SmI_3. SmI_3 is initially selected for investigation due to the superior performance of the LiI supporting electrolyte with both Sm(II) and Sm(III) starting reagents. To investigate the feasibility of bulk electrochemical SmI_3 reduction, we initially synthesize SmI_3 by combining commercial 0.09 M SmI_2 solution in THF with 0.5 equivalents of solid I_2 to eliminate confounding effects arising from the presence of the triflate anion. Bulk electrolysis is conducted on a saturated solution of this SmI_3 ("0.09 M") in a divided cell to prevent consumption of the SmI_2 product at the counter electrode. After 48 hours at an applied potential of –0.4 V vs. Ag wire pseudo-reference electrode, the orange SmI_3 solution turns dark blue in the working electrode compartment of the divided cell (Figure 3.11a), indicating electrochemical formation of

SmI_2. No visible precipitate remains in the working electrode compartment, further suggesting reduction of Sm(III) to the more soluble SmI_2. The chronoamperometry trace shown in Figure 3.11b reveals that SmI_3 reduction primarily occurs over the first 30 hours of the electrolysis. UV-Vis spectra of the electrolyte solutions before electrolysis and from each compartment of the divided cell after electrolysis (Figure 3.11c) indicate formation of SmI_2 in the working electrode compartment, as evidenced by the absorption peaks at 550 and 615 nm.[86] No crossover of the SmI_2 product is observed as shown by the absence of the absorption peaks in the UV-Vis spectrum of the counter electrode compartment.

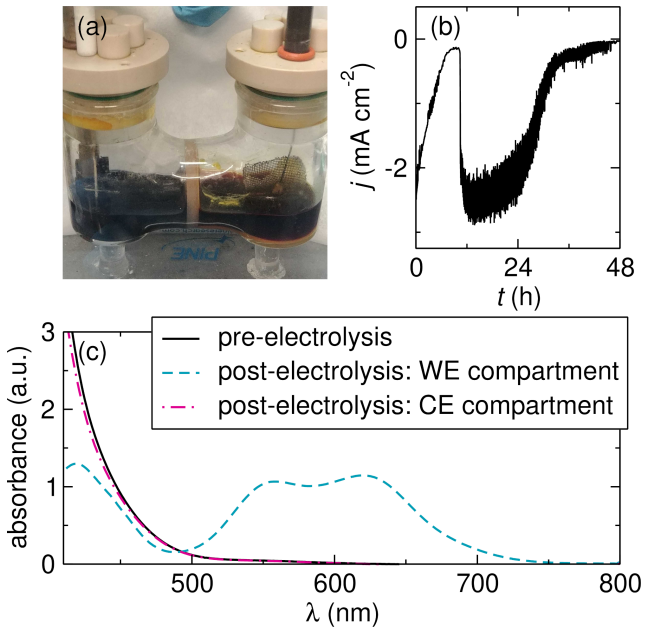

Figure 3.11: Bulk electrolysis of 0.09 M SmI_3. (a) Photograph of the SmI_x solutions in the divided cell after 48 h bulk electrolysis. The electrolyte in the working electrode compartment is dark blue, indicating formation of SmI_2. (b) Chronoamperometry trace collected during bulk electrolysis of the saturated SmI_3 solution. (c) UV-Vis spectra of the electrolyte before electrolysis and from each side of the divided cell after electrolysis. The two characteristic absorption bands associated with SmI_2 are observed in the working electrode (WE) compartment and are absent in the counter electrode (CE) compartment.

Titration of the resulting SmI_2 solution by the method of Hilmersson[90] indicates that a solution of 0.09 M SmI_2 was electrochemically generated, which equates to full conversion of the SmI_3 precipitate to SmI_2 at approximately 100% Faradaic efficiency. The results exceed yields of electrogenerated SmI_2 reported by Nishibayashi

and coworkers[87, 110] and highlight the ability to continuously electrochemically reduce Sm(III), an important consideration for electrocatalytic experiments.

To determine whether conventional reactivity of SmI_2 is preserved using the electrogenerated SmI_2, 0.05 mmol benzylacetone (**1**) is added to an aliquot of the electrogenerated SmI_2 solution containing 0.10 mmol SmI_2 (2 eq., approx. 1.1 mL). Scheme 3.12 shows the expected reduction reaction of benzylacetone by SmI_2, including the corresponding alcohol (**2**) and pinacol (**3**) products. Similar reactions are prepared using a commercially available solution of SmI_2 in THF (0.09 M as determined by titration) as a control, either as purchased or with 5 eq. added LiI to mimic the presence of supporting electrolyte. Reactions with both the commercial and the electrogenerated SmI_2 solutions favor **3** (entries 1-3). The reaction with commercial SmI_2 solution affords **3** in 38% yield and **2** in 24% yield, the reaction with commercial SmI_2 solution with 5 eq. LiI affords **3** in 72% yield and **2** in 13% yield, and the reaction with electrogenerated SmI_2 affords **3** in 58% yield and **2** in 38% yield. Both the yield and selectivity toward **3** are comparable when using the electrogenerated SmI_2 vs. the commercial SmI_2, with similar diastereomeric ratio across experimental conditions. While the cause of the slightly lower yield of **3** when using electrogenerated SmI_2 (entry 3) vs. commercial SmI_2 + 5 eq. LiI (entry 2) is unknown, it is possible that the presence of trace Ag^+ ions generated from the Ag wire pseudo-reference electrode may contribute to the shift in product distribution.

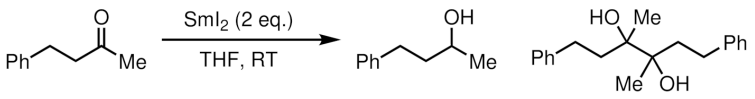

1 **2** **3**

Entry	SmI_2 source	Deviation from std. conditions	conv. 1 (%)	yield 2 (%)	yield 3 (%)
1	commercial	none	98	24	38 (1.24:1 dr)
2	commercial	+ 5 eq. LiI	99	13	72 (1.25:1 dr)
3	electrogenerated from SmI_3	none	96	38	58 (1.23:1 dr)
4	commercial	+ 8 eq. H_2O, 6 eq. Et_3N	64	52	<1
5	commercial	+ 8 eq. H_2O, 6 eq. Et_3N, 5 eq. LiI	74	62	<1
6	electrogenerated from SmI_3	+ 8 eq. H_2O, 6 eq. Et_3N	85	77	<1

Figure 3.12: Reduction of benzylacetone by SmI_2.

Additives, including various amines and water, have been shown to shift product speciation from pinacol to alcohol products in similar reactions.[111, 112] To determine whether the product distribution could be similarly modulated using electrogener-

ated SmI_2, the reduction of benzylacetone by SmI_2 is carried out in the presence of triethylamine (Et_3N) and water (entries 4-6). Reagent **1** (0.05 mmol) is added to an aliquot of the electrogenerated SmI_2 solution containing 0.10 mmol SmI_2 (2 eq., approx. 1.1 mL), along with 8 eq. H_2O and 6 eq. Et_3N. Similar reactions are prepared using commercially available SmI_2 in THF, with and without LiI as described above. All three reactions afford only product **2**. The reaction with commercial SmI_2 solution affords **2** in 52% yield, the reaction with commercial SmI_2 solution with 5 eq. LiI affords **2** in 62% yield, and the reaction with electrogenerated SmI_2 affords **2** in 77% yield. The results indicate that the electrogenerated SmI_2 performs comparably compared to commercial SmI_2 in the reduction of **1** to **2**.

Ideally, a more practical procedure for electrochemical generation of SmI_2 under electrocatalytic conditions should begin directly from a commercially available Sm(III) salt. SmI_3 can be prepared by combining $Sm(OTf)_3$ and LiI as described above. Bulk electrolysis of this SmI_3 is conducted at lower concentrations with LiI (Figure 3.13) and LiTFSI (Figure 3.14) supporting electrolytes. In the electrolyte with LiTFSI, a slight excess of LiI (3.3 eq.) is added to $Sm(OTf)_3$ to yield a yellow solution. After 24 h electrolysis at –1.5 V vs. Ag wire, the electrolyte in each of the working electrode compartments is dark blue, similar to the highly concentrated reaction with the LiI supporting electrolyte. These practical conditions for SmI_2 formation from stable, commercially available $Sm(OTf)_3$ highlight the synthetic utility of the electrochemical reduction as a means toward Sm-catalytic reactions.

3.4 Conclusions

Here, we show that the relative coordination strength of the anion of the Sm salt is the primary factor determining the electrochemical reducibility of Sm(III) species. The coordination environment of Sm can be controlled to an extent through anion exchange with the supporting electrolyte. A larger supporting electrolyte anion may prevent aggregation of Sm species, leading to more facile Sm(II)/(III) redox. Several Sm(III) reagents can be electrochemically reduced to Sm(II) in a suite of supporting electrolytes, and electrochemical reduction of SmI_3 to SmI_2 has been demonstrated at bulk scale with 0.5 M LiI supporting electrolyte in THF, highlighting the ability to continuously reduce Sm(III) over time. The electrochemically prepared SmI_2 is used in the reduction of benzylacetone to the corresponding pinacol and alcohol products, yielding similar performance to commercially available SmI_2 solutions.

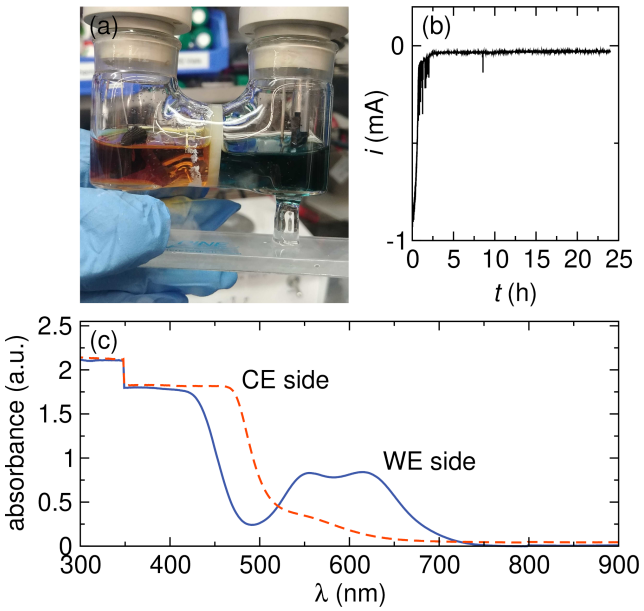

Figure 3.13: Bulk electrolysis of 5 mM SmI_3 with LiI supporting electrolyte. (a) Image of the 5 mM SmI_3 + 0.5 M LiI electrolyte after 24 h bulk electrolysis. (b) Chronoamperometry trace collected during bulk electrolysis. (c) UV-Vis spectra of the electrolyte from each compartment of the divided cell after electrolysis. SmI_3 was electrochemically reduced to SmI_2 at the working electrode.

In future work, the electrochemical reduction of Sm(III) may be used to close the catalytic cycle of Sm-mediated reductive reactions, significantly reducing the quantity of Sm required to achieve high product yields and removing the requirement for a sacrificial reductant to recycle the Sm catalyst. However, the strongly coordinating oxyanion intermediates formed during the reduction of carbonyl species may displace weakly coordinating ions, such as I^{--}, in the Sm coordination sphere. Cleavage of the Sm(III)-O bond typically requires harsh reactants such as silyl halides, from which the halide can also undergo anion exchange with more weakly coordinating anions coordinated to Sm. Developing new reagents or pathways to cleave the Sm(III)-O bond without significantly altering the nature of the Sm catalyst is of great interest for the development of new electrocatalytic Sm-driven reactions.

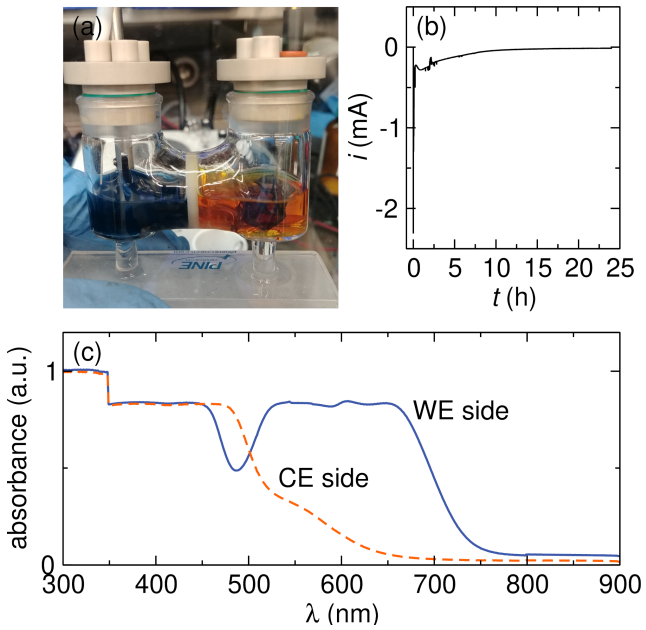

Figure 3.14: Bulk electrolysis of 5 mM SmI_3 with LiTFSI supporting electrolyte. (a) Image of the 5 mM SmI_3 + 0.1 M LiTFSI electrolyte after 24 h bulk electrolysis. (b) Chronoamperometry trace collected during bulk electrolysis. (c) UV-Vis spectra of the electrolyte from each compartment of the divided cell after electrolysis. SmI_3 was electrochemically reduced to SmI_2 at the working electrode.

Chapter 4

INCREASING THE ZN^{2+} DEPOSITION OVERPOTENTIAL TO LIMIT CROSS-PLATING FROM ZN SACRIFICIAL ANODES

Abstract: In organic electrochemistry, reductive electrosynthesis often requires a sacrificial anode to charge-balance the cathodic reaction of interest. Zn sacrificial anodes circumvent issues of side reactions and anode passivation that are common with more reducing metals, but the mild Zn^{2+} reduction potential can lead to unwanted crossover and Zn metal deposition at the cathode in undivided cells. Increasing the Zn^{2+} desolvation barrier by employing strongly coordinating additives and supporting electrolyte anions may lead to an increase in the Zn deposition overpotential and may limit or prevent competitive Zn reduction. Research on non-aqueous Zn batteries has demonstrated that the desolvation barrier can be tuned by changing the electrolyte composition. Here, we report the effects of various electrolytes and additives on the Zn deposition overpotential. Crown ethers slightly increase the deposition overpotential but do not prevent Zn deposition at strongly reducing cathodic potentials, while glyme additives decrease the desolvation barrier.

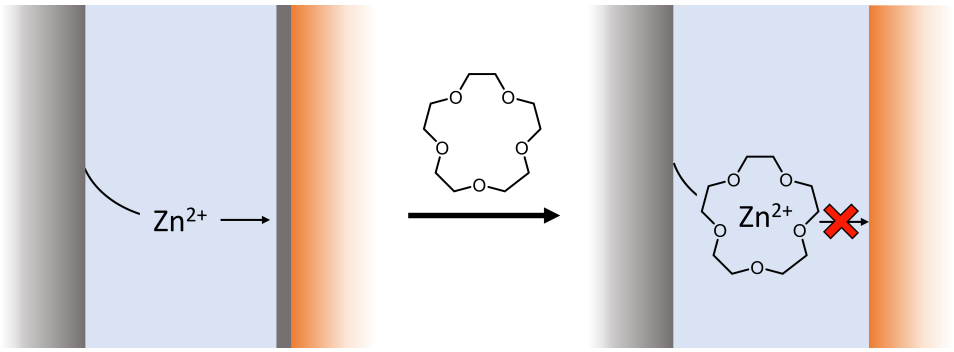

4.1 Introduction

The recent revival of organic electrosynthesis has resulted in less hazardous synthetic conditions and new reactivity that is not accessible with traditional synthetic techniques.[3, 113–118] In reductive electrosynthesis, organic transformations are performed at the cathode, and these reactions are charge-balanced by the oxidation of a metal sacrificial anode. Commonly used sacrificial anodes include Mg, Al, and Zn.[116] Sacrificial anodes enable optimization of the reductive reaction, which can later be combined with a nonsacrificial anodic process in paired electrosynthesis.[119–122]

Though the reaction at the sacrificial anode is often not directly connected to the synthetic reaction occurring at the cathode, the choice of anode material can impact the success of the reductive reaction. For instance, strongly reducing metals such as Mg or Al can chemically react with organic substrates or products, limiting yields of the desired product. Reducing metals are also more likely to be passivated by a high-impedance surface film, either before the reaction via the formation of an insulating native oxide layer or during the reaction when the anodically generated cations form nonconductive salts which nucleate at the anode surface. These processes are discussed in more detail in Chapter 5.

Using a less reducing metal as the sacrificial anode can circumvent anode passivation reactions in most cases, leading to higher yields from the reductive reaction. However, the more mild reduction potential of a sacrificial anode like Zn can induce its own challenges. The Zn^{2+} cations generated during oxidation of the anode are easily reducible. In an undivided cell, these cations can migrate from the anode to the cathode, where they can be reduced to Zn metal. This competitive reduction lowers the Faradaic efficiency of substrate reduction, decreases yields of the synthetic product, and can cause hazardous short circuits if left unchecked. Furthermore, the mild reduction potential precludes the use of Zn sacrificial anodes in deep reductive electroysnthesis, which requires extreme reducing potentials at the cathode.[123]

Switching to a divided cell would prevent crossover and eliminate the risk of short circuits, but divided cells present additional operational challenges in organic electrosynthesis. Few effective separators have been developed for use in divided cells employing organic electrolytes, and these must be carefully chosen to prevent side reactions or mixing of the catholyte and anolyte.[124] The separator also introduces a large junction potential in two-electrode cells, which are commonly used to screen reaction conditions in synthetic laboratories.

Alternatives to the divided cell would enable a greater range of synthetic conditions and allow for more effective organosynthetic transformations. For example, tuning the desolvation barrier of Zn^{2+} to disfavor Zn plating at the cathode could limit competitive Zn reduction in an undivided cell and improve the yield and Faradaic efficiency of the synthetic reaction. Research in the battery community has probed the Zn^{2+} desolvation barrier in a variety of organic solvents and with several supporting electrolytes. Strongly coordinating solvents as well as Zn salts with less dispersed charge on the anion have been shown to raise the Zn^{2+} desolvation barrier.[125] In batteries, the desolvation barrier and corresponding deposition overpotential should be minimized to promote efficient cycling and rapid charge transfer. However, in organic electrosynthesis, the Zn^{2+} desolvation barrier and deposition overpotential should be maximized to limit cross-plating and promote reduction of the substrate. Therefore, nonaqueous electrolytes that are least effective in Zn metal batteries due to poor desolvation kinetics are expected to be more effective in preventing Zn plating during reductive electrosynthesis.

Herein, we pursue two strategies to increase the Zn^{2+} desolvation barrier in organic electrolytes (Figure 4.1). We initially focus our studies on electrolytes using tetrahyrdofuran (THF) as the solvent. THF coordinates Zn^{2+} more strongly than acetonitrile (MeCN) but less strongly than N,N-dimethylformamide (DMF); however, the proposed restrictions on DMF use in the European Union necessitate further development of reactions in solvents other than DMF.[126] We first attempt to modulate the anion coordination strength to keep Zn^{2+} in solution. Next, we vary the coordination environment of Zn^{2+} by employing coordinating additives such as glymes and crown ethers. The crown ether additives slightly increase the Zn^{2+} deposition overpotential but not to the extent necessary to enable the use of Zn sacrificial anodes in deep reductive electrosynthesis. The results described herein lay important groundwork for future electrolyte design in organic electrosynthesis and suggest possible directions for further study in this area.

4.2 Methods

All chemicals were handled and stored in an Ar-filled glovebox unless stated otherwise. Tetrahydrofuran (THF, >99.9%, Fisher Scientific) was dried on a solvent purification system (Pure Process Technologies) and transferred to the glovebox without exposure to air. All chemicals were purchased from Sigma-Aldrich and used without further purification unless otherwise noted. Tetrabutylammonium

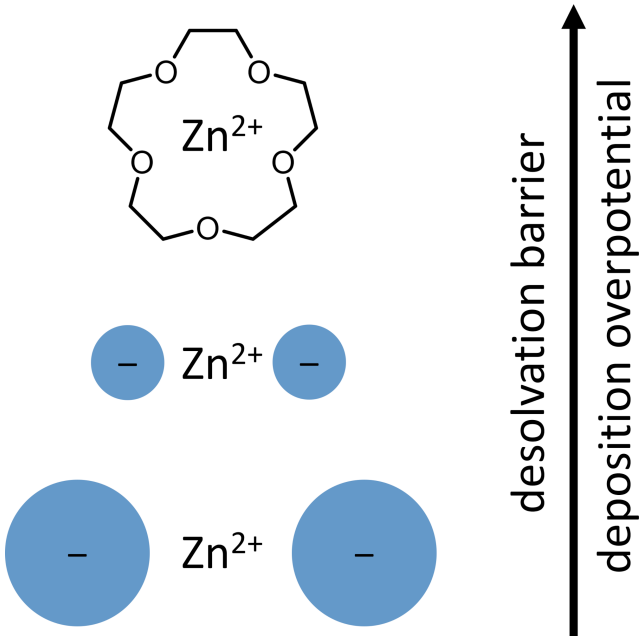

Figure 4.1: The Zn^{2+} desolvation barrier and deposition overpotential can be increased slightly by employing anions with minimal charge dispersion and additives that coordinate strongly to Zn^{2+}. By tuning these barriers, competitive Zn^{2+} reduction at the cathode may be prevented in certain conditions.

bis(trifluoromethanesulfonyl)imide (>99%) was dried under vacuum at 120 °C overnight prior to use.

All electrolytes were prepared in an Ar-filled glovebox by combining the chosen zinc salt, additive (if used), and supporting electrolyte in 2 mL THF and stirring to yield a cloudy or colorless solution.

All electrochemical experiments were conducted on a VMP3 potentiostat (Bio-Logic) in a N_2-filled glovebox. All experiments were performed in a 10 mL glass three-electrode cell (Pine Research Instrumentation) with a gas-tight PEEK cap. Unless otherwise stated, a graphite plate (IKA) was used as the working electrode and a Zn plate (IKA) was used as the counter and reference electrode. All experiments were conducted with 85% iR compensation to deconvolute the effects of electrolyte resistance from properties that affect the Zn deposition potential. During bulk electrolysis experiments, the electrolyte was stirred to facilitate transport of the active species to the electrode surface.

The graphite and Zn electrodes were polished prior to use. Graphite electrodes were ablated with sandpaper, sonicated for 5 min in water, and dried 30 min before being

transferred to the glovebox. Zn electrodes were ablated with sandpaper; polished with 9, 3, and 1 μm diamond suspensions in succession; and sonicated for 30 min in equal parts acetone and isopropanol.

For experiments that used a separate reference electrode, a Pt|Fc/Fc^+ reference electrode was prepared following literature precedent from a Pt wire, ferrocene (Fc, 98%), ferrocenium hexafluorophosphate ($FcPF_6$, 95%, Combi-Blocks), and tetrabutylammonium hexafluorophosphate ($TBAPF_6$, >99%).[127] Fc and $TBAPF_6$ were recrystallized prior to use. The Pt wire was cleaned in concentrated nitric acid and dried with a H_2 flame. The wire was sealed in a glass tube with a ceramic frit, and the tube was filled with a solution of 4 mM Fc, 4 mM $FcPF_6$, and 0.1 M $TBAPF_6$ in THF.

4.3 Results and Discussion

Battery research has demonstrated that the Zn^{2+} desolvation barrier increases with increasing coordination strength of nearby anions.[125] We therefore begin by attempting to tune the desolvation barrier for anodically generated Zn^{2+} by introducing Zn salts and supporting electrolytes with anions of different sizes and coordinating ability. Smaller anions have less dispersed charge and coordinate to Zn^{2+} more strongly than large anions. For the purposes of overcoming diffusion limitations in cyclic voltammetry (CV) and capturing Zn plating and stripping behavior, we use supporting electrolytes containing Zn^{2+} salts, even though during synthetic reactions Zn^{2+} is only generated at the anode and is not present at the start of the reaction. Zn^{2+} salts are poorly soluble in THF, so TBA^+ co-supporting electrolytes are employed here to improve ionic conductivity.

Supporting electrolytes of 0.1 M $Zn(TFSI)_2$ + 0.1 M TBATFSI ($TFSI^-$ electrolyte) and 0.1 M $Zn(OTf)_2$ + 0.1 M TBAOTf (OTf^- electrolyte) are examined initially (Figure 4.2). Several CVs are collected in succession, and the second and tenth scans are shown. In both supporting electrolytes, the Zn plating potential is initially near –0.2 V vs. Zn/Zn^{2+}. No major differences between the electrolytes are observed in early scans, despite the greater charge dispersion on $TFSI^-$ than on OTf^-. After ten scans, the Zn plating potential drops to <0.05 V in the $TFSI^-$ supporting electrolyte (Figure 4.2a). The decrease in plating potential suggests a change in the electrode/electrolyte interface that permits more facile plating after several formation cycles. By contrast, no change in plating potential is observed in the OTf^- supporting electrolyte over the first ten CV scans (Figure 4.2b). The

consistent plating potential suggests that Zn deposition is not gated by interphase formation in the same way as in the $TFSI^-$ electrolyte and that the desolvation barrier for Zn^{2+} is higher in the OTf^- electrolyte than in the $TFSI^-$ electrolyte. However, the differences in plating potential between the supporting electrolytes containing $TFSI^-$ and OTf^- are not large enough to significantly expand the range of potentials which will avoid Zn cross-plating in organic electrosynthesis.

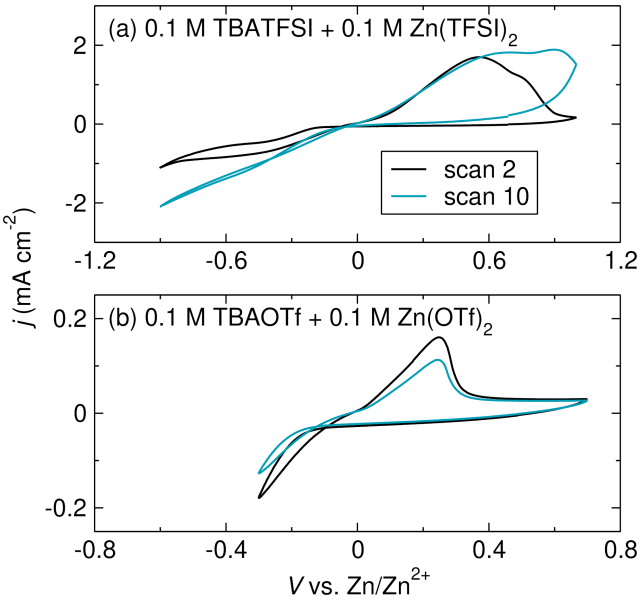

Figure 4.2: CVs of (a) 0.1 M $Zn(TFSI)_2$ + 0.1 M TBATFSI and (b) 0.1 M $Zn(OTf)_2$ + 0.1 M TBAOTf supporting electrolytes in THF. CVs were collected continuously to observe changes in the Zn plating potential over time; scans 2 and 10 are shown. Both Zn plating potentials start around –0.2 V, but in the electrolyte containing $TFSI^-$ the plating potential shifts to less negative values over time, while in the electrolyte with OTf^-, the plating potential remains roughly constant. All voltammograms are collected at a scan rate of 5 mV s^{-1}.

In an attempt to increase the Zn plating potential further, we add glymes of various chain lengths to the OTf^- supporting electrolyte. Linear ethers with multiple O donor sites can wrap around the Zn cation, yielding stronger solvation than that provided by cyclic ethers such as THF and a consequently higher desolvation barrier.[125] CVs of the OTf^- supporting electrolyte with various concentrations of mono-, di-, and tetraglyme are shown in Figure 4.3. Addition of glymes of any chain length and at any concentration resulted in a less negative Zn plating potential. The decrease in plating potential may be due to competition between the glyme additives and OTf^- in the Zn solvation shell. Such behavior has been demonstrated previously: Anions

coordinate to Zn^{2+} more readily in cyclic ethers such as THF than in linear ethers like glymes, and Zn^{2+}-solvent interactions are correspondingly stronger in glymes than in THF.[128] The results observed here suggest that linear ethers are not sufficiently strongly coordinating to Zn^{2+} to merit their inclusion as an electrolyte additive for preventing competitive Zn reduction in organic electrosynthesis.

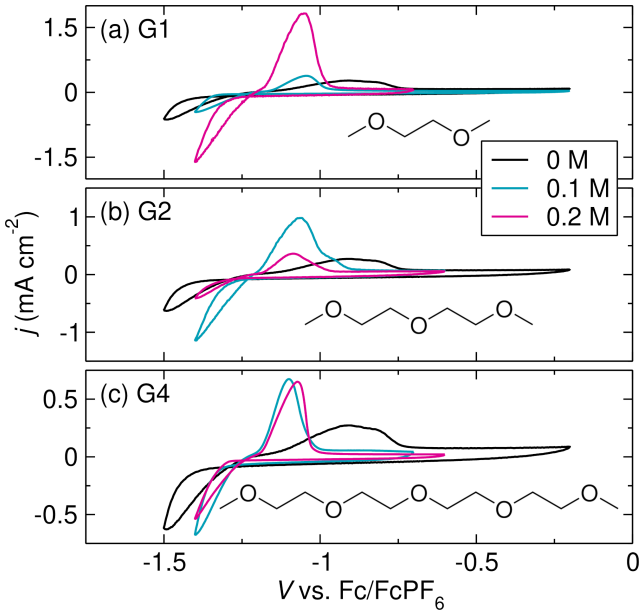

Figure 4.3: CVs of 0.1 M $Zn(OTf)_2$ + 0.1 M TBAOTf with added (a) monoglyme (G1), (b) diglyme (G2), and (c) tetraglyme (G4). Glyme concentrations of 0, 0.1, and 0.2 M are shown. In all cases, addition of glymes shifts the Zn plating potential to more positive values. All voltammograms are collected at a scan rate of 5 mV s^{-1}.

Macrocyclic ethers may be more likely than linear ethers to fully coordinate Zn^{2+} in solution and raise the desolvation barrier. The structure of crown ethers places all of the O donor atoms close to the cation, unlike glymes which need not coordinate to Zn^{2+} through every O atom. The calculated and experimental coordination geometries of Zn^{2+}-crown ether complexes suggest that 15-crown-5 and 18-crown-6 both adopt a tightly-folded geometry about Zn^{2+}, meaning these complexes are stable in mildly polar solvents like THF.[129] To determine whether coordination to crown ethers increases the Zn^{2+} desolvation barrier and deposition overpotential, 15-crown-5 and 18-crown-6 were added to the OTf^- electrolyte in various concentrations. CVs of the electrolytes with crown ethers are shown in Figure 4.4. Unlike the glyme additives, the crown ethers increase the Zn plating potential in all cases. When 15-crown-5 is used as the additive, the increase in plating potential trends with

increasing crown ether concentration (Figure 4.4a). At 0.3 M 15-crown-5, the Zn plating potential is approximately 300 mV greater than that in the OTf^- electrolyte with no additives. The increase in Zn plating potential is more mild when 18-crown-6 is used as the electrolyte additive (Figure 4.3b), reaching up to 250 mV more negative than the additive-free electrolyte when using 0.1 M 18-crown-6. The results suggest that coordination by a crown ether is more effective at increasing the Zn^{2+} desolvation barrier than using strongly coordinating anions or glymes in the supporting electrolyte.

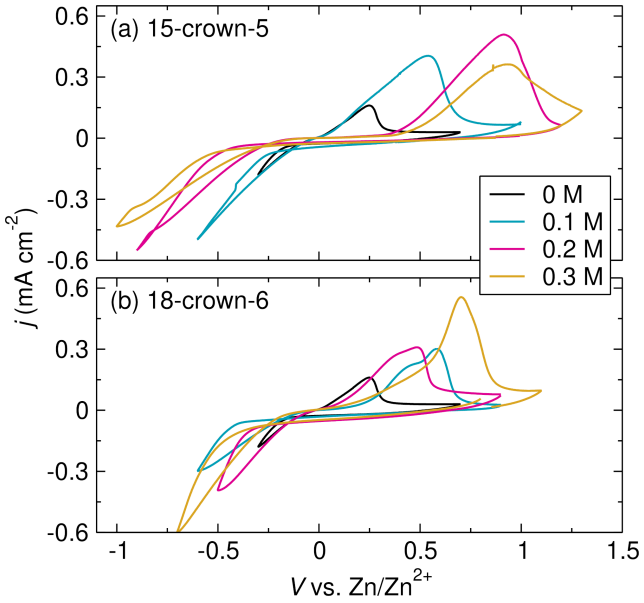

Figure 4.4: CVs of 0.1 M $Zn(OTf)_2$ + 0.1 M TBAOTf with added (a) 15-crown-5 and (b) 18-crown-6 in THF. Crown ether concentrations of 0, 0.1, 0.2, and 0.3 M are shown. Addition of 15-crown-5 leads to a negative shift in the Zn plating potential that increases with increasing ether concentration, while addition of 18-crown-6 yields more modest negative shifts. All voltammograms are collected at a scan rate of 5 mV s^{-1}.

To assess the applicability of crown ether additives under reductive electrosynthetic conditions, the crown ethers are first added to a solution of 0.05 M $Zn(OTf)_2$ + 0.2 M TBAOTf in THF. A lower $Zn(OTf)_2$ concentration is chosen to more closely mimic synthetic conditions, which will not include Zn^{2+} species other than those generated at the anode. The $Zn(OTf)_2$ used here serves as a sacrificial reductant which will enable continuous replacement of Zn species via anodic oxidation of the Zn sacrificial anode. Potentiostatic electrolysis is conducted on the 0.05 M $Zn(OTf)_2$ + 0.2 M TBAOTf supporting electrolyte with no additives, with 0.2 M

18-crown-6, and with 0.2 M 15-crown-5 (Figure 4.5). Electrolysis is first performed at –0.05 V vs. Zn/Zn^{2+} for 1 h, and then the voltage is stepped 0.05 V more negative every subsequent hour until Zn plating is observed. In the electrolytes with no additive and with 0.2 M 18-crown-6 (Figure 4.5a-b), reductive current is observed when the electrolysis is conducted at –0.1 V, and visible Zn deposits appear on the graphite electrode after 1 h at –0.1 V. Such early evidence of Zn plating suggests that 18-crown-6 is not an effective additive for increasing the Zn deposition overpotential. In the electrolyte with 0.2 M 15-crown-5, reductive current is not observed until electrolysis is conducted at –0.15 V vs. Zn/Zn^{2+}, and Zn deposits at the cathode are only observed when the electrolysis potential is –0.2 V. The results suggest that 15-crown-5 is more effective than 18-crown-6 at increasing the Zn deposition overpotential. However, the mild increase in overpotential (~100 mV) is insufficient to prevent Zn plating under strongly reducing potentials such as those used in organic electrosynthesis and will likely not expand the range of reactions in which a Zn sacrificial anode can be employed.

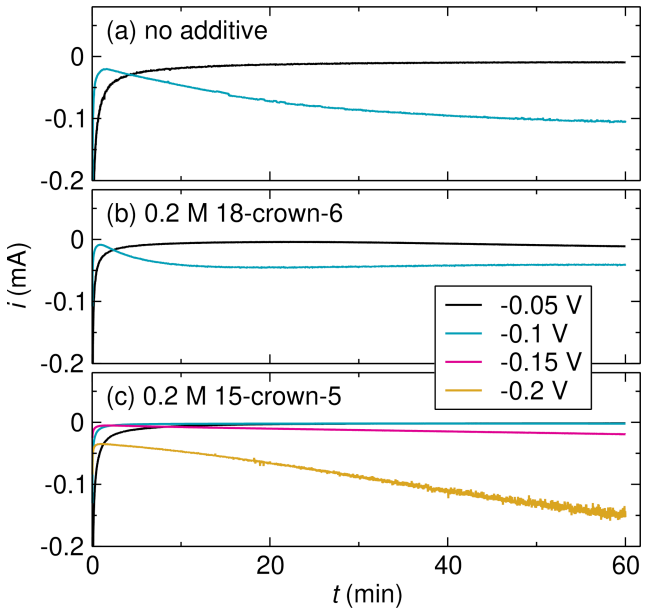

Figure 4.5: Potentiostatic electrolysis of 0.05 M $Zn(OTf)_2$ + 0.2 M TBAOTf with (a) no additive, (b) 0.2 M 18-crown-6, and (c) 0.2 M 15-crown-5 in THF. In all cases, electrolysis is performed at –0.05 V vs. Zn/Zn^{2+} for 1 h. The potential is then stepped 0.05 V more negative every hour until Zn deposition is observed at the cathode. Visible Zn deposition is observed at –0.1 V when either no additive or 18-crown-6 is used and at –0.2 V when 15-crown-5 is used.

4.4 Conclusions

Here, we demonstrate that adding crown ethers to an electrolyte containing anions that coordinate relatively strongly to Zn^{2+} slightly increases the Zn deposition overpotential. However, the increase in overpotential is likely not large enough to prevent competitive Zn reduction in electrosynthesis or to enable the use of Zn sacrificial anodes under strongly reducing conditions in an undivided cell. As such, the use of Zn sacrificial anodes for electrosynthesis in undivided cells remains restricted to cases where a substrate or catalyst in solution has a less negative reduction potential or significantly faster reduction kinetics than Zn^{2+}. Crown ether additives can be leveraged when the reduction potential of a substrate is very similar to that of Zn and when the moderate increase in deposition overpotential would enable electrolysis at a potential which distinguishes between the two reduction reactions. Competitive reduction of Zn can also be managed by employing a divided cell when the experimental design permits.

4.5 Potential Future Directions

Future work in this area will require electrolyte species that coordinate very strongly to Zn^{2+}. These species could be solvents such as DMF, supporting electrolyte anions (including those which are insoluble in THF but may be more soluble in other solvents), or additives such as cryptands or amines. Additives in particular may react or interfere with certain classes of substrates, so the increase in coordination strength afforded by the new species must be weighed against the changes in the available set of compatible reaction conditions for the reductive chemistry. Crown ethers may be worthy of further investigation in other solvent systems, and the crown ether that coordinates most strongly to Zn^{2+} will vary with solvent polarity; smaller crowns that leave the Zn^{2+} ion exposed to solvent will be most effective in polar solvents, and larger crowns that fully wrap around the cation will be most effective in low-polarity solvents.[129]

To show that changes to the electrolyte composition have the desired effect of increasing the Zn^{2+} desolvation barrier, a significant increase in the deposition overpotential must be observed. Ideally, an increase of at least 1 V should be demonstrated in both CV scans and the electrolysis onset potential, and the lack of Zn deposition should be confirmed with imaging techniques such as scanning electron microscopy, energy-dispersive X-ray spectroscopy, or X-ray photoelectron spectroscopy. This increase would place Zn on par with Al in terms of the likelihood of competitive reduction, but the more mild reducing power of Zn metal would limit

the chemical decomposition of substrates or the surface passivation often observed with Al sacrificial anodes. Finally, the new electrolyte should be tested in a proof-of-concept electrosynthetic reaction to demonstrate its compatibility with at least one common class of organic reagents and to show that the Zn deposition overpotential is maintained in the presence of the organic substrate(s).

Chapter 5

A GUIDE TO TROUBLESHOOTING METAL SACRIFICIAL ANODES FOR ORGANIC ELECTROSYNTHESIS

Abstract: The development of reductive electrosynthetic reactions is often enabled by the oxidation of a sacrificial metal anode, which charge-balances the reductive reaction of interest occurring at the cathode. The metal oxidation is frequently assumed to be straightforward and innocent relative to the chemistry of interest, but several processes can interfere with ideal sacrificial anode behavior, thereby limiting the success of reductive electrosynthetic reactions. These issues are compounded by a lack of reported observations and characterization of the anodes themselves, even when a failure at the anode is observed. Here, we weave lessons from electrochemistry, interfacial characterization, and organic synthesis to share strategies for overcoming issues related to sacrificial anodes in electrosynthesis. We highlight common but underexplored challenges with sacrificial anodes that cause reactions to fail, including detrimental side reactions between the anode or its cations and the components of the organic reaction, passivation of the anode surface by an insulating native surface film, accumulation of insulating byproducts at the anode surface during the reaction, and competitive reduction of sacrificial metal cations at the cathode. For each case, we propose experiments to diagnose issues and characterize the anode, and we explore troubleshooting strategies to overcome experimental challenges. We conclude by highlighting open questions in the field of sacrificial-anode-driven electrosynthesis and by indicating alternatives to traditional sacrificial anodes that could streamline reaction optimization.

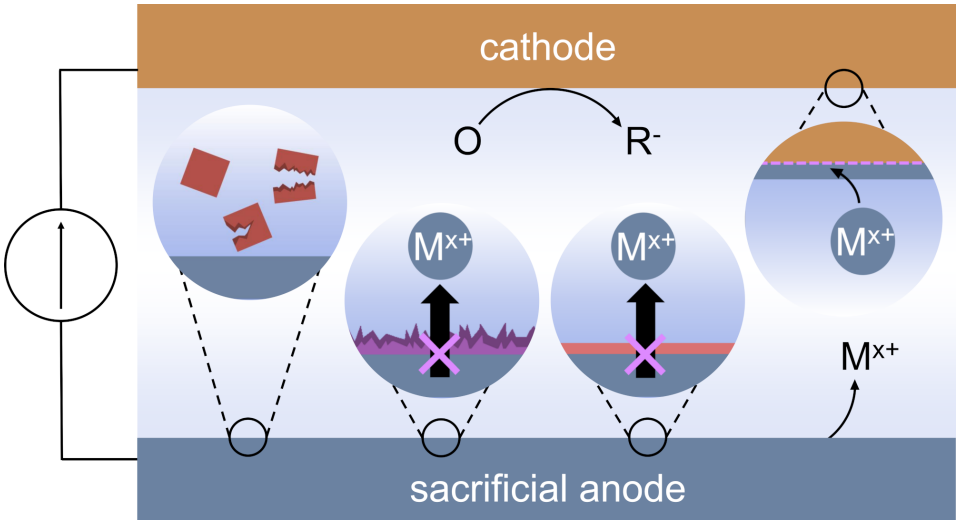

5.1 Introduction

Organic electrosynthesis has undergone a major revival in the past several years.[3, 113, 115, 117, 118, 130–135] The rapidly growing field enables new reactivity that is not achievable with traditional synthetic methods.[18, 136] Furthermore, the use of electrons as reagents offers routes to greener and safer synthetic conditions, potentially eliminating the need for harsh or hazardous chemicals.[3] Electrosynthesis also enables greater selectivity in synthetic reactions via the ability to fine-tune either the applied potential to promote specific reduction or oxidation reactions, or the applied current to select for the most kinetically labile reactions.[137] Electrochemical experiments offer a handle by which to probe the reaction mechanism, enabling greater mechanistic insight than would be achievable with chemical reductants.[138–140]

Though the eventual goal of organic electrosynthesis is to develop paired electrolyses in which reactions at both the anode and the cathode contribute to value-added products,[114, 119–122, 130, 131] individual half reactions must be well understood if they are to be combined into a larger process. In reductive electrosynthesis, these half reactions frequently rely on charge balancing via the oxidation of a sacrificial anode, typically Mg, Al, Zn, or Fe.[116] Sacrificial anodes have enabled the use of electrochemistry in a variety of organic reactions.[113–118, 141, 142] During electrolysis, the metal electrode is oxidized, releasing metal cations into solution as shown in Figure 5.1. The cations are often thought to be inert to the reductive chemistry of interest. In some situations, the cations do participate in the reaction of interest; in these cases the anode is not truly sacrificial and plays a more substantial role.[143–145]

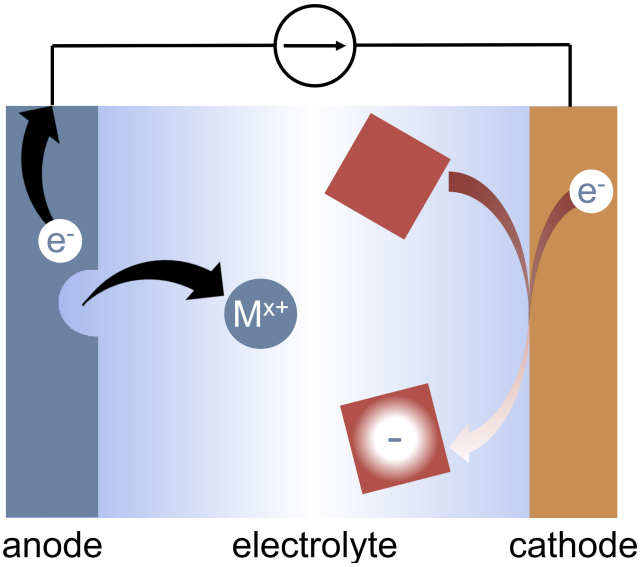

Figure 5.1: Sacrificial metal anodes enable reductive electrosynthesis by charge-balancing reductive reactions at the cathode. During a reductive reaction, the metal sacrificial anode is oxidized, releasing metal cations into solution.

In an ideal case, electrolysis with sacrificial anodes offers several benefits during early stages of reaction development. First, the oxidation reaction itself is typically straightforward and occurs at a known, constant potential. The oxidation of the metal anode is sufficient to charge balance the reductive reaction of interest, thereby preventing unwanted oxidation of substrates or additives in the solution. The addition of metal cations into solution over the course of the reaction is less likely to limit the scope of the reductive reaction than the use of other chemicals as sacrificial reductants.[121] Furthermore, metal electrodes are generally inexpensive and easy to store, and they provide a less hazardous alternative to commonly used sacrificial reductants.[146]

The ideal sacrificial anode should not limit or interfere with the reductive reaction of interest, either through direct interactions with reaction components or through its electrochemical performance. In particular, four major criteria must be satisfied to ensure that the reaction is not limited by the sacrificial anode:

1. Both the metal anode and the cations generated during electrolysis should not degrade any electrolyte components or reagents used in the reductive reaction.

2. Any inherent reactivity between the metal and the electrolyte solution should not form an insulating surface film or prohibit oxidation of the anode.

3. The anode should permit metal stripping throughout the reaction, meaning that it must not be passivated by products or byproducts formed over the course of the electrolysis.

4. Metal cations generated from anodic oxidation should not undergo competitive reduction at the cathode.

These four criteria are outlined in Figure 5.2 and serve as a basis for the outline of our discussion.

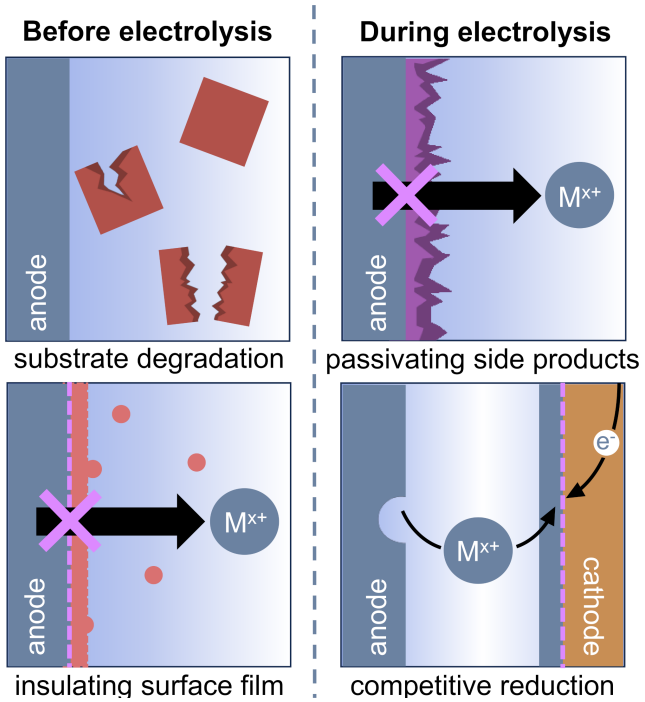

Figure 5.2: Sacrificial anodes can deviate from ideal behavior and limit the reductive reaction of interest, even under conditions that would normally be compatible with said reaction. Chemical reactions between the electrode and substrate, formation of an insulating surface film on the anode, anode passivation by side products formed during the reductive reaction, and competitive plating of anodically generated cations at the cathode can all prevent ideal anode performance.

Though many reductive electrosynthetic reactions assume that each of these sacrificial anode criteria are met, in reality several processes can interfere with these assumptions and prevent ideal sacrificial anode behavior. The surface chemistry at metal electrodes is extremely sensitive to the chemicals present in the reaction solution, a fact that has been well studied in the analytical electrochemistry community. In addition to the electrode materials, the success of an electrosynthetic

reaction depends on a host of factors that must be optimized, including chemical parameters such as the solvent, reactants, and additives, as well as electrochemical parameters including the supporting electrolyte and the magnitude of the applied potential or current.[142, 143, 147–152] Changes to any of these parameters can induce nonideal behavior at the sacrificial anode, leading to failed reactions, low yields, hazardous short-circuits, and/or extreme voltages that exceed the compliance limits of the potentiostat and stop the reaction early. Thus, the performance of the anode can impose limits on the available reaction conditions, eliminating chemical space that would otherwise be compatible with the reaction of interest.

The issues associated with sacrificial anode performance are compounded by a lack of reported observations of the anodes themselves.[153, 154] Many electrosynthetic works simply select the sacrificial anode that provides the highest yield in optimization experiments without investigating the anodic chemistry, even when a failure at the anode is observed. Not only does this strategy limit the range of compatible conditions for the reductive reaction, it also ignores potential mechanistic contributions from the cations generated during sacrificial anode oxidation. Fortunately, problems at the anode can often be diagnosed and rectified with a few brief experiments, leading to higher product yields and an expanded set of compatible reaction conditions.

Understanding and characterizing processes at the anode requires knowledge of both electrochemical and surface characterization techniques that can interrogate the chemistry at the electrode. Here, we integrate lessons from electrochemistry, interface characterization, and organic synthesis to elucidate strategies for overcoming issues related to sacrificial anodes. We highlight four common but underexplored challenges that cause reactions to fail. For each, we suggest electrochemical and surface characterization experiments to diagnose the problem, and we present experiment design strategies for troubleshooting sacrificial anodes. The fundamentals of electrochemical techniques in organic synthesis have been reviewed extensively elsewhere and will not be covered here.[137–139, 155–158] We conclude with an outlook for the future of this multidisciplinary field, including open challenges related to sacrificial anode optimization and potential new directions for developing reductive half reactions with minimal interference from anodic processes. We hope that the strategies presented here will improve the process of screening and optimizing electrosynthetic reactions, expand the chemical space in which reductive reactions can occur, enable more robust yields

from reductive electrosynthesis, and encourage collaborations at the intersection of electrochemistry, organic synthesis, and interface chemistry.

5.2 Side Reactions

As in all synthetic procedures, side reactions between reagents must be considered when optimizing a reaction. In the case of electrosynthesis, care must be taken to avoid side reactions between components of the electrochemical system as well as between the substrates and additives common to traditional organic synthesis. In particular, reactions between any combination of the electrodes, solvent, supporting electrolyte, and substrates must be considered. Even if not directly related to the reductive chemistry, chemical reactions between the sacrificial anode and any other component of the electrolyte solution can lead to low yields of the desired product.

Examples of side reactions with the anode

In many cases, reactions that occur at the sacrificial anode are chemical reductions of a reactant by a strongly electropositive anode, such as Mg. The canonical example of such a detrimental side reaction is the reaction between Mg metal and organic halides (R-X) to form Grignard reagents, RMgX, and related compounds in solution.[159, 160] Given that organic halides are frequently used as substrates for reductive electrosynthesis, such side reactions are likely problematic during the optimization stage of many methodologies. It should be noted that most Grignard reactions with non-activated Mg require an induction period, in which the native MgO surface layer is removed from the Mg source to expose reactive Mg, but the length of this induction period depends on the other compounds in solution as well as any pretreatment steps, such as polishing the Mg metal. In electrochemical systems, the anode is usually chemically or mechanically polished to ensure effective Mg stripping, but the solution composition will be reaction-dependent. In addition to affecting the substrates and mechanistic pathway, the formation of Grignard reagents can contribute to the growth of a high-impedance passivation layer at the Mg anode,[161, 162] which will be discussed in more detail in Section 5.4. In all cases, the electrolyte should be checked for potential Grignard-forming conditions before a Mg sacrificial anode is employed.

The formation of Grignard reagents is not the only undesired side reaction that can occur at sacrificial anodes. In addition to alkyl halides, Mg can also react with esters and ketones. Condon *et al.* observed that in an attempted alkylation

of decyl trichloroacetate with triethylborane, the ester group was reduced when a Mg sacrificial anode was used, leading to the formation of decanol as an undesired side product. The researchers noted that when a Mg or Zn sacrificial anode was employed, the electrolysis time was shortened from the expected 1 h to 30 min, suggesting that some chemical reduction of the substrate occurred at the anode. No chemical reduction was observed when an Al or Fe anode was employed.[163] In the electrochemical allylation of carbonyl compounds, Durandetti *et al.* observed side reactions between carbonyl species and a Mg sacrificial anode resulting from enolization of the ketone substrate. The authors attribute this reactivity to the reducing power of Mg; similar side reactions were not observed when a Zn anode was used in place of Mg.[164] Mg can chemically reduce a variety of substrates, including activated alkenes, pyridine derivatives, and cyanoarenes (Figure 5.3), which could lead to undesired byproducts in an electrochemically driven reaction.[165–168] Zn can chemically reduce carbonyl halides, potentially causing similar issues.[169] Substrates that can be chemically reduced by a mildly reducing metal can often also be reduced by more strongly reducing metals, necessitating the careful choice of sacrificial anodes in an electroreductive reaction. The choice of solvent can introduce potential side reactions as well. Saboureau *et al.* observed overconsumption of a Mg sacrificial anode during electrolyses carried out in dimethylformamide (DMF) solvent, which was traced back to chemical corrosion of the Mg anode via reductive decomposition of the solvent. Zn and Al sacrificial anodes were not subject to the same corrosion reaction.[170] Furthermore, Zn sacrificial anodes can chemically reduce Ni and Pd catalysts for reductive coupling reactions, possibly complicating reaction optimization and mechanistic studies.[171, 172]

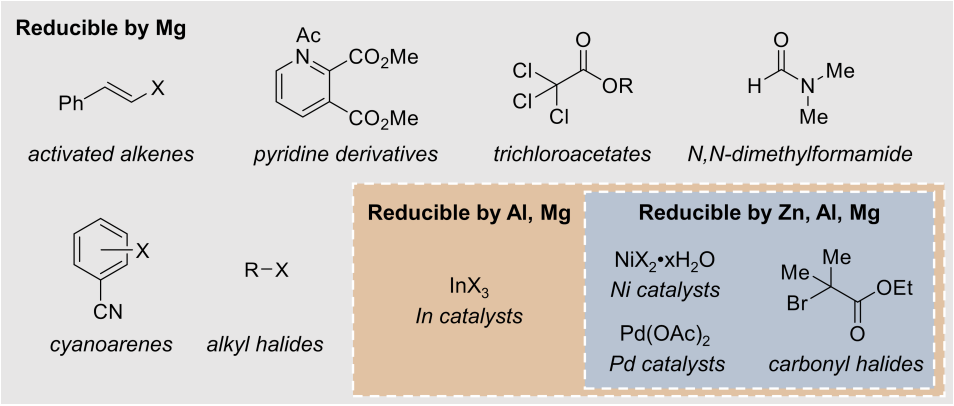

Figure 5.3: Examples of substrates and catalysts that can be chemically reduced by various metal sacrificial anodes.

Examples of side reactions with anodically generated cations

In addition to side reactions between the metal anode and reaction components in solution, the cations generated during oxidation of the anode can also interfere with the reductive reaction. Nedelec *et al.* demonstrated that the nature of the cation generated from the sacrificial anode dictates the extent of electrochemically driven cross-coupling products of alkyl halides.[151] Introduction of metal cations and salts via oxidation of the anode can also lead to diminished yields. For example, Peters *et al.* observed that anode-derived Mg salts limited the success of an electrochemical Birch reaction. Addition of Mg salts directly to the electrolyte reduced yields of the desired diene from 74% to 30%. In cases when the solution was not stirred during electrolysis, smaller anode-cathode distances were correlated with lower yields, suggesting that metal salts generated at the anode negatively impacted yields.[173]

Symptoms of side reactions with the anode

As detailed above, there are several indicators of side reactions between the sacrificial anode and another component of the system. Similarly to traditional chemical reactions, high conversion of the starting material but low yields of the desired product serve as key markers of background reactivity. Side products may appear in ^{1}H-NMR spectra of the post-electrolysis solution, either as discrete and identifiable species or as an intractable mixture formed from decomposition of the substrate, additives, or solvent. In certain cases, degradation of the electrolyte solution may be visible through a color change or the formation of precipitates.

Diagnosing the problem

A few experiments can be undertaken to determine whether the formation of an undesired side product is related to the sacrificial anode. Perhaps the simplest is to exchange the anode for a different metal. A less reducing metal, such as Zn, is less likely to undergo detrimental side reactions with electrolyte components, but the nature of any observed side reactions will be solution-dependent and must be optimized as such. However, if a specific sacrificial anode must be used, or if an understanding of the side reaction is important to mechanistic development, further electrochemical characterization can be carried out. A divided cell is an excellent tool that can be employed to decouple any observed reductive decomposition from reactions occurring at the cathode. Saboureau *et al.* adopted this approach when determining the nature of the Mg corrosion reaction in DMF during the electrosynthesis of carboxylic acids from organic halides. A Mg anode was fitted to the anodic compartment, which was

then charged with an organic halide (4-chloro-trifluoromethylbenzene) and several supporting electrolytes in succession. The cathodic reaction was the straightforward electrochemical reduction of 1,2-dibromoethane, an easily reducible species that serves as an efficient counter reaction. Analysis of the anodic compartment after electrolysis indicated that the aromatic halide was not consumed at the anode and that only DMF had degraded.[170] This set of divided cell experiments conclusively demonstrated the nature of the side reaction between anodically polarized Mg and DMF.

Troubleshooting the problem

First, we discuss solutions to the anode chemically reducing components in the electrolyte. A simple solution would be to use a less reducing metal; however, another metal could introduce new side reactions or different challenges. Alternatively, a divided cell can be used to carry out the electrolysis itself, not just in a diagnostic role, to prevent crossover from the cathodic chamber into the anodic chamber. A more complicated but exciting solution would be to generate a surface film on the anode metal that conducts the corresponding metal cation but is electronically insulating. The film would be akin to the solid-electrolyte interphase (SEI) formed on anodes in Li ion batteries, however, such a strategy has not been pursued in the context of sacrificial anodes and will thus be discussed in the Outlook section.

Next, we discuss issues of reactivity between the metal cation generated at the anode and components in the solution. A divided cell can again be used to prevent the generated cation from reacting with anything in the reaction mixture. If an undivided cell is required, a strongly coordinating binding agent could sequester the generated cation, provided that the bound complex does not react further with the electrolyte or passivate the anode.

It is important to acknowledge that not all reactions between the sacrificial anodes and the electrolyte solution are deleterious. The cations and salts produced by oxidation of the anode can participate in the reductive reaction, stabilize products formed at the cathode, or function as products in their own right. For example, Mellah and coworkers have explored the use of a samarium sacrificial anode to directly generate Sm(II) reagents for C–C bond formation in solution.[99, 174, 175] The Sm metal anode is oxidized to Sm^{2+}, and various Sm^{2+} salts including $SmCl_2$, $SmBr_2$, SmI_2, and $Sm(OTf)_2$ (OTf = triflate, $CF_3SO_3^-$) were formed *in situ* through the addition of $^nBu_4X$ salts.[99] Cations or salts formed from oxidation of the

anode can also function as *in situ*-generated reactants participating in the reduction reaction. Lu *et al.* demonstrated low product yields from an electroreductive radical silylation reaction when a divided cell was used, in part because anodically generated Mg^{2+} is proposed to participate in the overall reaction mechanism.[176] Manabe *et al.* also demonstrated such reactivity in the electrochemical reduction of triphenylphosphine oxide to triphenylphosphine. $AlCl_3$, generated via oxidation of an Al sacrificial anode, facilitated selective cleavage of the P–O bond.[177] Even if the generated cations do not participate directly in the reaction, they can stabilize products or species of interest formed during the reductive reaction. For example, Mg^{2+} and Al^{3+} cations coordinate to carboxylate anions formed as the products of electrocarboxylation reactions.[141, 178, 179] This coordination stabilizes the carboxylate and forms a precipitate, which can easily be extracted from the organic solution. Similarly, Zn^{2+} cations can stabilize intermediated formed during the reduction of quinolines.[180] Furthermore, metal anodes can chemically reduce species in solution to form reagents that are otherwise difficult to access. For example, Hilt and Smolko observed the chemical reduction of In(III) to In(0) at an Al anode. The In(0) was then oxidized at the anode to form In(I), a catalyst for the allylation of aldehydes, ketones, and esters.[181] The metal anode can also influence the selectivity of the reaction. In an electrochemical thiolation reaction via cross-electrophile coupling of alkyl bromides with functionalized thiosulfonates, Ang *et al.* determined that the cross-coupling reaction only proceeds when a Mg sacrificial anode is used. Attempts to run the reaction with a Zn, Fe, or Cu anode resulted in homocoupling of the thiosulfonate to form diphenyldisulfide as the sole product after 3 h electrolysis.[182]

5.3 Anode Passivation by Inherent Metal Reactivity

Reactions between the sacrificial anode and reaction components can affect the electrochemical behavior of the anode itself, in addition to altering the electrolyte solution. Decomposition of certain electrolyte components can form ionically insulating surface layers on the sacrificial anode, prohibiting further contact between the electrolyte and the metal and preventing oxidation of the anode. Many anode materials — particularly electropositive metals such as Mg and Al — contain native oxide layers that similarly limit efficient metal oxidation.

Examples of passivation by native oxides

The native surface oxide layers that form on Mg and Al develop before exposure to the electrolyte solution. While the oxide layer can be beneficial in preventing undesired chemical reactivity between the anode and substrate before electrolysis, in many cases the surface film is ionically insulating and does not permit oxidation or dissolution of the anode material.[183–188] Solid-state conductivity of multivalent cations is very difficult due to their high charge density and large size.[189] Once the oxides are formed, they are very thermodynamically stable, which is obvious from their position on the Ellingham Diagram. In fact, MgO and Al_2O_3 are two of the most thermodynamically stable oxides relative to the corresponding metal.[190] Mg is so oxophilic that even if it is sputtered in ultra-high vacuum, the surface is still covered by MgO.[191] The surface film thus limits the electrochemical reaction by preventing the anodic stripping from charge-balancing the cathodic reaction at low overpotentials. The oxide layer forms whenever Mg or Al is in contact with air or moisture.[183, 192] As such, a rigorous electrode polishing procedure is required to remove the passivating oxide film. Polishing the anode has the added benefit of removing any impurities or oxidized products remaining on the anode from previous reactions. If the anode has been used in prior reactions, macroscale deposits of oxidized product can be removed via sonication, electropolishing, or an acid rinse.[173, 193] The electrode should then be mechanically polished under an inert atmosphere using a razor blade, fine-grit sandpaper, or a rotary tool to minimize growth of the oxide surface film.

Even if the sacrificial anode is rigorously polished, electropositive metals can still form an insulating surface film when placed in contact with organic electrolytes. Even with rigorous drying procedures, electrolytes can still contain ppb to ppm amounts of trace water that will react with the metal. Additionally, solvent decomposition or reactions between the anode and the supporting electrolyte can form insulating surface films that prevent oxidation of the anode.[176, 177, 193, 194] Importantly, these insulating surface films may not be immediately apparent or visible to the naked eye. Even an electrode that appears shiny and metallic with no obvious corrosion could experience difficulties with anodic oxidation, preventing the cathodic reaction from proceeding to completion and limiting reaction scale-up.[177, 195]

Examples of passivation by supporting electrolyte

Reactions between the anode material and the supporting electrolyte are particularly insidious as these are two components that are optimized independently but are in fact codependent. Selecting either an anode material or a supporting electrolyte too early in the optimization process can lead to inadvertent exclusion of compatible reaction conditions if the only factor limiting the cathodic reaction is the non-obvious evolution of an insulating surface film on the anode. Fortunately, the formation of such surface films has been studied extensively in the battery community. Several supporting electrolytes commonly used in organic electrosynthesis have already been screened for metal deposition and stripping for use in battery applications, and many are found to be incompatible with Mg and Al stripping.[177, 196–198] In particular, fluoride-containing electrolytes — including those containing BF_4^-, PF_6^-, AsF_6^-, or others with anions that can hydrolyze in the presence of trace water to form HF — have been shown to form ionically insulating MF_x-rich surface films on Mg and Al.[177, 196] Other electrolytes, including those containing $CF_3SO_3^-$, $(CF_3SO_2)_2N^-$ (bistriflimide or TFSI), or ClO_4^-, are also incompatible with Mg anodes.[196–198] Using supporting electrolytes containing any of the aforementioned anions with a Mg or Al sacrificial anode is likely to lead to passivation of the anode and unsatisfactory electrochemical performance.

Symptoms of passivation by inherent reactivity

Several physical and electrochemical signatures could indicate formation of an insulating surface film on the anode. During an electrolysis experiment, a sharp increase in the overall cell voltage might be observed, especially at the start of the reaction. Depending on the instrument used, the voltage may increase until the compliance limit of the device is reached, causing the reaction to stop prematurely. In many cases, the insulating surface film is not readily apparent and no visible electrode fouling is observed because the surface films can be very thin.

Diagnosing the problem

The first step in determining if a reaction fails due to the formation of an insulating surface film on the anode is to search the literature for prior reports of reactivity between the anode and the solvent or supporting electrolyte. For Mg anodes in particular, research on SEIs in Mg metal batteries is a good starting point for exploring inherent reactivity between the anode and electrolyte.[21, 196, 198] If no prior reports of passivation exist, several electrochemical experiments can point

to the existence of an ionically insulating surface film. Linear sweep voltammetry (LSV), in which the sacrificial anode is the working electrode and the potential is swept anodically, can indicate whether metal stripping is observed at the expected potential. Figure 5.4a shows an example of an LSV experiment designed to assess metal stripping at an Al electrode.[199] When a $TBABF_4$ supporting electrolyte in tetrahydrofuran (THF) is used, the oxidative current density is extremely low and no Al oxidation is observed due to the formation of a passivating film resulting from a chemical reaction between Al and the electrolyte. The current density also decreases upon subsequent scans, indicating that Al stripping becomes more difficult due to the growth of the passivating film. It should be noted that a separate reference electrode is required for such experiments to eliminate confounding effects that may arise from the possible passivation of the counter electrode in a two-electrode cell. Several reference electrodes suitable for use in nonaqueous systems have been developed.[127, 200–202]

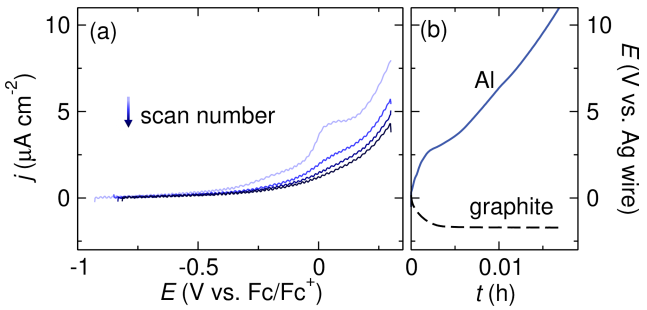

Figure 5.4: Voltammetry of Al sacrificial anode passivation with $TBABF_4$ supporting electrolyte. (a) Linear sweep voltammograms of an Al sacrificial anode in THF with 0.1 M $TBABF_4$ supporting electrolyte. The voltammograms were collected at 5 mV s^{-1} scan rate with 85% iR compensation. (b) Voltage profiles of Al and graphite electrodes during galvanostatic Al stripping in THF with 0.5 M $TBABF_4$ supporting electrolyte. The Al stripping experiment was conducted with ^{t}BuBr as a sacrificial reductant. Adapted from ref.[199] with permission from the Royal Society of Chemistry.

The potential at the anode during a constant current electrolysis can also be monitored to confirm that the high voltage observed in an electrolysis experiment is related to processes at the anode and not the cathode. Figure 5.4b shows the potentials of an Al anode and a graphite cathode during reduction of *tert*-butyl bromide (^{t}BuBr). The potential at the cathode is steady and constant, suggesting that the reduction proceeds as expected. However, the voltage at the Al anode increases to >10 V within a few seconds and quickly reaches the compliance limit of the po-

tentiostat. This sharp polarization and extreme overpotential at the anode indicate that the oxidation reaction does not proceed smoothly, likely due to the presence of a passivating surface film.[199] Monitoring both the cathode and anode voltage during electrolysis requires the use of a nonaqueous reference electrode and a potentiostat equipped with the hardware necessary to record both the working and counter electrode potentials.

Electrochemical impedance spectroscopy (EIS) may indicate changes in the anode surface resistance over the course of a reaction. To diagnose an ionically insulating surface film, an EIS experiment in a two-electrode cell using the electrolyte of interest and with both electrodes made from the sacrificial anode metal will provide the resistance associated with oxidizing the anode; a notably high resistance (more than a few kΩ) suggests that an insulating surface film has formed, preventing metal stripping and limiting the anode's performance in the reductive reaction.[203] Note, however, that a low resistance does not necessarily mean that no surface film has formed, as an electronically conductive but ionically insulating surface film can exhibit low impedance.

If the nature of the reaction that causes surface passivation is not known, various surface characterization techniques can pinpoint the electrolyte component that reacts with the anode. Scanning electron microscopy (SEM) and energy-dispersive X-ray spectroscopy (EDS) provide information about the morphology of the anode after reaction and a spatially resolved elemental distribution map, respectively. These techniques require high vacuum and thus will only probe solid products at the surface. Therefore, if elements exclusively present in the electrolyte are observed, then we can assume the electrolyte has reacted with the metal.[204] For a more in-depth understanding of the surface reaction, X-ray photoelectron spectroscopy (XPS) provides information about the chemical environment of each element within the top 5–10 nm of the surface film.[199, 205] XPS is useful for determining the identity of the surface species and for characterizing extremely thin surface films, such as the oxide layers formed when Mg and Al are exposed to air.

Troubleshooting the problem

Research in the fields of corrosion science and energy storage have demonstrated that passivating metal oxide layers on Mg or Al can be removed by adding halide salts to the electrolyte solution. On pure Al metal, chloride ions migrate through the oxide film, breaking down the oxide layer and forming "pits" in the metal; corrosion

by such pitting reactions has been well studied and is not limited to chlorides.[206–211] Chloride ions have also been shown to break down non-oxide insulating surface films on Al. Manabe *et al.* demonstrated that an insulating AlF_3 surface film which formed when Al was in contact with PF_6^--containing electrolyte could be removed by introducing TBACl as a co-supporting electrolyte, along with the chelating amine tetramethylethylenediamine (TMEDA) to promote Al stripping.[177]

Bromide additives can also break down the insulating surface film on Al anodes. Zhang *et al.* observed that adding TBABr as a co-supporting electrolyte enabled Al oxidation in electrolytes that would otherwise passivate the metal (Figure 5.5a). The current densities observed in the LSV with TBABr co-supporting electrolyte are much higher than those observed without TBABr (shown in Figure 5.4a). The current density also steadily increases upon subsequent scans, suggesting that surface passivation does not limit Al stripping. In a follow-up electrolysis experiment, the Al anode potential remained low and constant for several hours (Figure 5.5b), suggesting that Br^- contributes to the formation of an ionically conductive surface film on Al. The beneficial effect of additives is not limited to bromides in this case; Cl^--, Br^--, and I^--containing additives all enabled Al oxidation.[199]

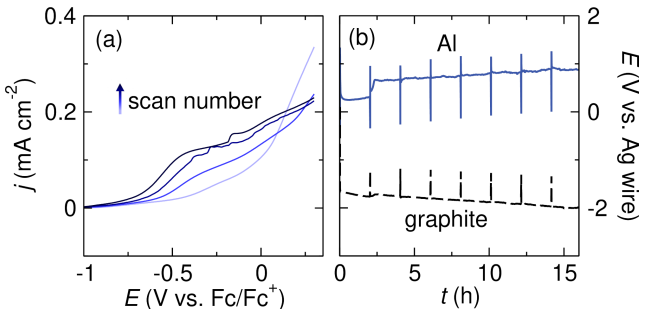

Figure 5.5: Voltammetry of Al sacrificial anode with $TBABF_4$ + TBABr supporting electrolyte. (a) Linear sweep voltammograms of an Al sacrificial anode in THF with 0.05 M $TBABF_4$ + 0.05 M TBABr supporting electrolyte. The voltammograms were collected at 5 mV s^{-1} scan rate with 85% iR compensation. (b) Voltage profiles of Al and graphite electrodes during galvanostatic Al stripping in THF with 0.25 M $TBABF_4$ + 0.25 M TBABr supporting electrolyte. The Al stripping experiment was conducted with ^{t}BuBr as a sacrificial reductant. Adapted from ref.[199] with permission from the Royal Society of Chemistry.

Similar strategies can be applied in systems with Mg sacrificial anodes. Addition of $MgCl_2$ to a solution of $Mg(TFSI)_2$ in dimethoxyethane (DME) resulted in significant improvements in Mg oxidation compared to the solution without $MgCl_2$, likely due to destabilization of the surface oxide film.[188] $MgCl_2$ was later shown to suppress the

passivation of Mg metal by PF_6^- ions.[194] Li *et al.* showed that, as an alternative to Cl-containing salts, small amounts of I_2 could be added to an electrolyte consisting of $Mg(TFSI)_2$ and DME to form an ionically conductive MgI_2 surface film that mitigated the Mg oxidation overpotential.[212]

If no satisfactory means of suppressing the formation of an insulating surface film on Mg or Al can be found, less oxophilic anodes such as Zn may be more applicable to the system at hand. Zn anodes are chemically compatible with a wide range of solvents and supporting electrolytes and are less likely to exhibit high stripping overpotentials due to passivation via inherent reactivity.[125, 213, 214]

5.4 Passivation by Products Formed During Anodic Stripping

Insulating surface films can also form due to processes that occur during the electrolysis in addition to or in lieu of the films that form immediately upon contact with the electrolyte, as described in the previous section. During stripping, fresh metal surface is exposed to the electrolyte and the corresponding metal cation is generated, ideally in solution. The fresh metal surface can react with the electrolyte components differently than the original metal surface because the surface layers described in the previous section can be anodically destroyed. The newly exposed metal can react with the electrolyte to form a new surface film composed of decomposition products from the supporting electrolyte, solvent, or organic substrate.[215, 216] Further, though stripping produces metal cations that ideally dissolve into the electrolyte, the metal cations can react at the anode/electrolyte interface to form insulating deposits.

Examples of passivation by insulating salt nucleation

Passivation of the sacrificial anode during electrolysis has been observed in several synthetic reactions. Here we define passivation as the evolution of a high impedance surface film that shuts down electrochemistry at that electrode. In many cases, this passivation is linked to the use of strongly reducing anodes like Mg or Al.

First we focus on examples using Mg anodes. While attempting to scale up reactions involving electrochemical cross-electrophile coupling of alkyl halides, Zhang *et al.* initially observed high cell voltage accompanied by visible formation of a thick passivating film during the first few hours of electrolysis.[205] Lu *et al.* observed similar passivation of the Mg sacrificial anode in an electrochemically driven three-component cross-electrophile coupling reaction; though conversion of

the starting material exceeded 95%, the desired product was obtained in low yields due to the growth of a thick passivating film at the anode and accompanying high cell voltage.[217] Anode passivation can also be influenced by seemingly unrelated components. In the electroreduction of epoxides, Huang *et al.* employed tripyrrolidinophosphoric acid triamide (TPPA) as a cosolvent to improve the solubility of the LiCl suppprting electrolyte in THF and to prevent cathodic reduction of the sacrificial metal cations. When the electroreduction was run in the absence of TPPA, the Mg sacrificial anode was coated in insulating salts, which passivated the anode and caused extreme cell voltages that stopped the reaction early.[218]

Mg is not the only sacrificial anode that can be passivated during electrolysis. In a Ni-catalyzed cross-electrophile coupling reaction, Perkins *et al.* observed significant precipitation of metal halide salts when either a Mg or Al sacrificial anode was used. Incomplete conversion of the starting material was observed when an Al anode was used, and no reaction was observed when using a Mg anode.[219] Walker *et al.* observed high cell voltage and passivation of a Zn sacrificial anode during electrolysis in an electrochemical Ni-catalyzed Mizoroki-Heck reaction. Due to the low yields and incomplete conversion of starting material, the authors posit that the Ni catalyst is incompatible with the high cell voltage that arises from the anodic passivation.[171]

Several of the passivation reactions described above can be attributed to salt nucleation at the anode surface. As metal cations are stripped into solution, they coordinate to anions in solution and form a surface layer of insoluble salts that prevents further metal stripping. Salt deposition is common with multivalent cations like Mg^{2+} and Al^{3+} since multivalent cations are difficult to solvate due to their high charge density.[128, 220] A rough or uneven anode surface can exacerbate nucleation of these salts at the anode/electrolyte interface.[204, 221] The surface roughness may arise from either insufficient electrode polishing or corrosion/pitting reactions with other species in solution, such as organic halides or halide complexes.[204, 221, 222] When an anodic potential is applied, the rough electrode surface generates an uneven electric field, which leads to non-uniform metal stripping and makes the surface even rougher (Figure 5.6). The roughness increases the surface area of the electrode, leaving more space for salt nucleation. Further, the nanoscale heterogeneities can change the contact angle between a salt crystal and the electrode, which can reduce the energetic barrier for nucleation.[223] An insulating salt layer thus forms and will grow over the anode surface during the

reaction. While anode corrosion will need to be managed through reaction design, surface roughness can be mitigated by employing appropriate electrode polishing procedures (*vide supra*).

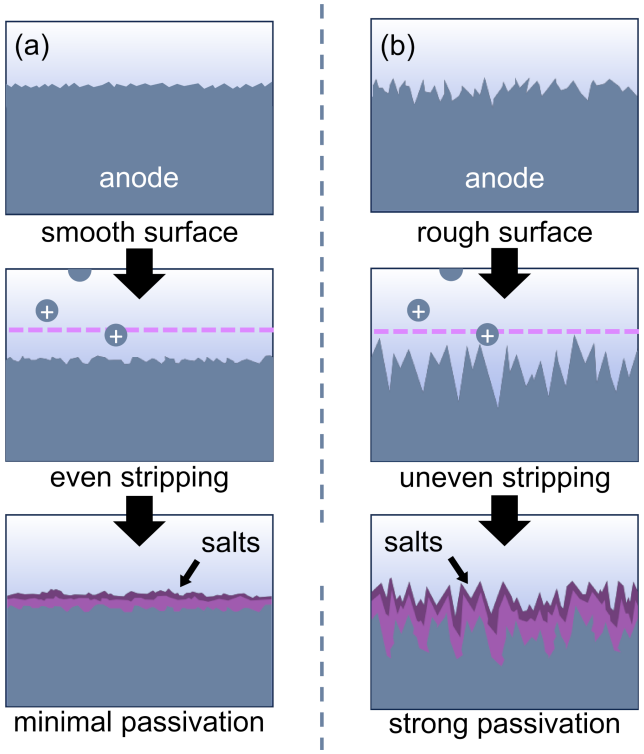

Figure 5.6: Metal stripping behavior as a function of surface roughness. (a) An even electric field leads to smooth metal stripping, while (b) an uneven electric field caused by surface heterogeneities leads to nucleation of metal salts as the anode is oxidized.

Symptoms of passivation by products formed during anodic stripping

Anode passivation by insulating salts or by corrosion during the reaction is usually readily apparent. Extreme anode fouling is common in such reactions and marked by the growth of a thick, visible surface coating. The coatings typically look black in color due to their rough nature and can appear as crystalline deposits, a tacky surface layer, or a conformal film. In a constant current experiment, the cell voltage typically increases over the first few minutes to hours of the electrolysis as the insulating surface blocks cation transport. Depending on the nature of the surface reactions, the anode fouling may result in low product yields, incomplete conversion of starting materials, and/or extreme cell voltages that reach the compliance limits of the instrument before the reaction is complete.

Diagnosing the problem

The appearance of a thick coating on the anode is usually enough to suggest that high cell voltages are related to processes happening at the anode. The growth of this film is often unrelated to the cathodic reaction and can thus unnecessarily limit the range of applicable conditions for the reductive reaction of interest. To verify that the anodic surface coating is insulating and prevents Mg stripping (and that the high cell voltage is not caused by some concurrent cathodic process), the voltage of both electrodes can be monitored during the electrolysis. This experiment requires the use of a reference electrode.[127, 200–202] Large fluctuations or a sharp increase in anode voltage suggest that anode passivation may be limiting conversion.[204, 205, 218]

A sharp increase in anode voltage is usually related to a mechanically stable surface coating. However, not all surface coatings are tightly bound to the anode, and mechanical stirring or inadvertent scraping of the anode during the reaction can dislodge salt deposits at the anode surface, exposing fresh metal. Figure 5.7a shows an example of a fluctuating anodic voltage profile that is characteristic of salts dislodging from the Mg anode. As the surface deposits grow, the anode voltage increases. When part of the insulating salt coating is dislodged from the anode surface by contact with the stir bar, for instance, fresh Mg metal is exposed, and Mg stripping can again occur at lower overpotentials. The anode potential then decreases, and the Mg anode is oxidized as in the beginning of the reaction. However, any salt remaining on the anode contributes to surface roughening, which exacerbates further salt nucleation when the Mg is oxidized. The salt layer regrows over the exposed Mg, and the anode voltage increases once again. This process repeats until the end of the reaction.[204]

If anode passivation is determined to be the cause of a failed electrolysis reaction, the next step is to determine the reaction that causes passivation. Characterization of the surface film by XPS, SEM, EDS, X-ray fluorescence, X-ray diffraction, or infrared or Raman spectroscopy can indicate the nature of species present at the anode surface. XPS gives the most detailed chemical information about the surface film and has been used to characterize surface reactions at sacrificial anodes previously,[204, 205] but depending on the nature of the reaction, other techniques may also provide sufficient information to understand the surface reaction.

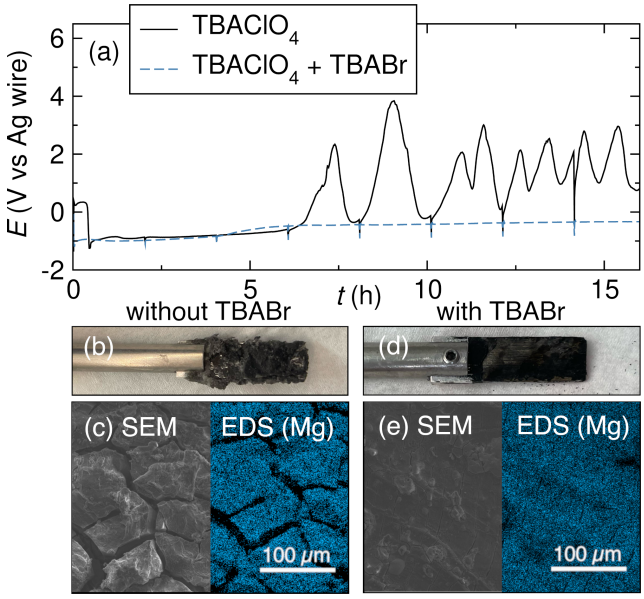

Figure 5.7: Mg sacrificial anode passivation is prevented by Br additives. (a) Voltage profiles of a Mg anode during Mg oxidation in the presence of 0.5 M ^{t}BuBr using either 0.5 M $TBAClO_4$ or 0.25 M $TBAClO_4$ + 0.25 M TBABr supporting electrolyte in THF. (b) Photo of the Mg anode with insulating salt nucleation after electrolysis with the $TBAClO_4$ electrolyte. (c) SEM/EDS images of the Mg anode after removal of the insulating salt coating. (d) Photo and (e) SEM/EDS images of the Mg anode with minimal salt buildup after electrolysis with the $TBAClO_4$ + TBABr electrolyte. Reprinted with permission from ref.[204], licensed under CC BY-NC-ND 4.0. Copyright (2023) The Authors.

Troubleshooting the problem

Once the nature of the surface reaction has been determined, several strategies can be used to troubleshoot the issue. If the surface reaction is due to passivation by salt nucleation, proper polishing procedures as described above can minimize the initial sites available for salt nucleation. Nucleation sites can form from corrosion reactions even if the anode is well polished, though, so chemical strategies for removing the salt layer may need to be employed. Coordinating solvents can be added to improve the solubility of metal salts. Zhang *et al.* added DME as a cosolvent to dissolve $Mg(ClO_4)_2$ and $MgBr_2$ which deposited at the Mg surface during cross-electrophile coupling of alkyl halides.[205] Lu *et al.* employed the same strategy in a three-component cross-electrophile coupling reaction.[217] Both $Mg(ClO_4)_2$ and $MgBr_2$ are poorly soluble in THF, which was used as the reaction medium, but linear ethers chelate more strongly to the Mg^{2+} ions and solubilize Mg salts.[224, 225] As described above, TPPA plays a similar role in supporting Mg sacrificial

anode oxidation in THF; a passivating salt layer forms on the anode in the absence of TPPA but does not prevent Mg oxidation when TPPA is present.[218] Peters *et al.* observed that TPPA could prevent passivation of a galvanized steel wire electrode following Mg deposition during an electrochemical Birch reaction.[173] The cosolvent/additive strategy is not limited to reactions in THF: During an electrocatalytic sulfination of aryl halides, Lou *et al.* demonstrated that passivation of a Zn sacrificial anode by a solution of SO_2 in acetonitrile could be mitigated by running the reaction in 9:1 acetonitrile:dimethylacetamide.[226] In pure dimethylacetamide, the black passivating deposits that formed on the electrode peeled off, suggesting that dimethylacetamide solvates the deposits better than acetonitrile.

Reactions between the anode and a substrate can be mitigated by including halide salts as additives or co-supporting electrolytes, similarly to managing anode passivation by reactions prior to electrolysis. Halide-containing salts can react at the metal surface to form an ionically conductive surface film, preventing nucleation of insulating species during the reaction. Zhang *et al.* demonstrated the utility of this strategy with a Mg electrode during the reduction of organohalides. During the reduction of ^{t}BuBr using a supporting electrolyte of 0.5 M $TBAClO_4$ in THF, the anode voltage fluctuates as described above (Figure 5.7a), and a thick surface film consisting of $Mg(ClO_4)_2$ and $MgBr_2$ forms at the anode. Figure 5.7 shows the anode after electrolysis (b) and after removal of the salt layer (c); the rough and insulating surface coating prevents effective Mg oxidation, and cracks in the Mg surface provide ample sites for additional salt nucleation. By contrast, when a supporting electrolyte consisting of 0.25 M $TBAClO_4$ and 0.25 M TBABr is used, the anodic voltage remains stable for the full reaction (Figure 5.7a) and the Mg surface is smooth and crack-free (Figure 5.7d-e). The Br-containing supporting electrolyte is thought to form an ionically conductive surface film on the Mg anode that prevents contact between the corrosive organohalide and the anode.[204] This passivation-preventing behavior has also been observed with a LiBr co-supporting electrolyte in Mg battery chemistry.[227]

5.5 Reduction of Anodically Generated Cations at the Cathode

Once effective metal stripping has been enabled, metal cations will be introduced to the electrolyte throughout the electrolysis reaction. When using an undivided cell, it is possible to reduce the newly generated metal cations at the cathode. Competitive reduction of the metal cations and the substrate leads to low Faradaic

efficiencies for electrochemical reactions. In some cases, the metal deposits can passivate the cathode, preventing further reduction of the substrate. Both situations can produce low product yields. Product distribution can also change if the kinetics of the reduction reaction at the plated metal are different from those of the original cathode material; sometimes this leads to new reactivity.[132] If reduction of the cation is significantly easier than reduction of the substrate, metal deposits at the cathode can build up and eventually reach the anode, leading to extremely hazardous short circuits.[228] In all cases, the plated metal is thus no longer innocent in the reaction, even if the anode metal and the cations in solution do not otherwise interact with components of the reductive reaction. Figure 5.8 shows the possible outcomes of competitive reduction of the organic substrate and anodically generated cations.

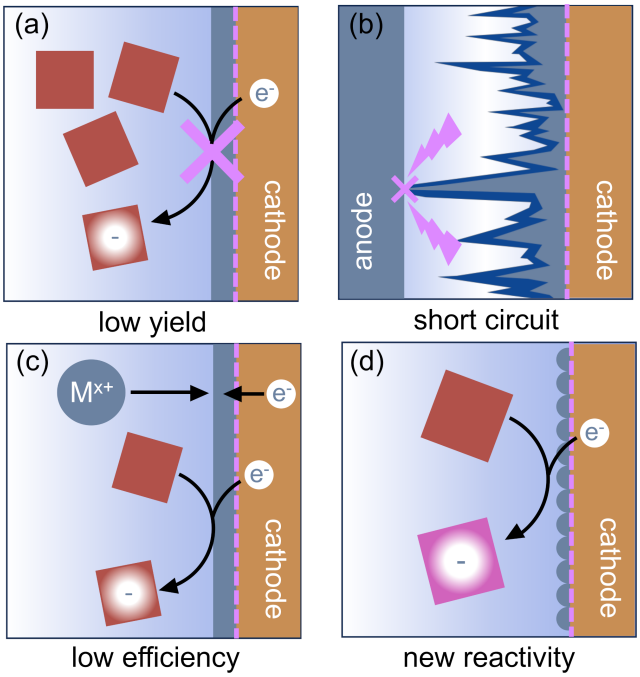

Figure 5.8: Reduction of anodically generated cations can outcompete reduction of the organic substrate at the cathode, leading to (a) low product yields, (b) hazardous short circuits, and (c) low Faradaic efficiency. (d) In certain cases, metal deposition from the anode can lead to new or better controlled reactivity at the cathode.

Special attention must be given to systems in which cross-plating of the metal cations is likely to occur. In a constant current electrolysis experiment, the applied current and reaction time are often chosen assuming that 100% of the electrons passed will go towards conversion of the reactants, i.e., the Faradaic efficiency approaches 100%. However, when metal cations are reduced at the cathode at the same time as the substrate, some of the electrons passed at the cathode will go toward metal

plating rather than substrate reduction, and product yields will be correspondingly lower. While competitive reduction of cations from the sacrificial anode is often an undesired side reaction that must be mitigated to improve reaction efficiency, reduction of the cations is not necessarily chemically incompatible with reduction of the substrate, and employing strategies to prevent metal plating can lead to higher product yields under otherwise similar conditions. Thus, care must be taken not to mistake low Faradaic efficiency for bad or incompatible reaction conditions, even though both result in lower-than-expected yields of the product.

Examples of competitive reduction

The competitive reduction of metal cations makes certain anodes, particularly those metals with mild reduction potentials, inapplicable in electrochemical reactions that require strongly reducing potentials at the cathode.[123] Zinc cations are particularly prone to cross-plating in undivided cells ($E^{\circ}_{Zn/Zn^{2+}}$=–0.76 V vs. SHE, compared to $E^{\circ}_{Al/Al^{3+}}$=–1.66 V and $E^{\circ}_{Mg/Mg^{2+}}$=–2.36 V), and the competitive reduction of the metal cations competes with the reductive reaction of interest. Yuan *et al.* noted that the competitive reduction of Zn cations and CO_2 or styrene substrates at a Ni cathode leads to low yields for styrene carboxylation. Such low yields were not observed when the sacrificial anode was switched to Al or Mg, which are thermodynamically more difficult to reduce.[229] Zhang *et al.* reported that reduction of Zn^{2+} generated at a Zn sacrificial anode competes with reduction of 4-*tert*-butylstyrene in an electrochemical carbofunctionalization reaction with alkyl bromides; a Mg sacrificial anode did not result in similar challenges.[230] In a Ni-catalyzed electrochemical cyclization of alkynyl aryl iodides, Déjardin *et al.* observed incomplete reduction of the substrate by the Ni catalyst, likely because reduction of anodically generated Zn^{2+} competes with reduction of the Ni catalyst. Switching to an Al sacrificial anode significantly increased product yields.[231]

While the mild reduction potential of Zn makes it particularly prone to competitive reduction and cross-plating, other anodically generated cations can also be reduced at the cathode under strongly reducing potentials. Lu *et al.* observed cathodic deposition of Mg metal from the sacrificial anode at the end of an electrolysis reaction involving electroreductive disilylation of alkenes. In dry, nonacidic solutions, the Mg plating does not pose any experimental hazards, but in wet solvent or in the presence of acid, the plated Mg is combustible in air and the reaction workup must be handled with caution.[176] Durandetti *et al.* observed cross-plating of Fe from a Fe sacrificial anode during a electroassisted zinc-free Reformatsky-type reaction

catalyzed by Fe species generated *in situ*. Fe deposition did not interfere with the reaction and high product yields could be obtained, but excess charge was passed to account for the low Faradaic efficiency.[232] Ishifune *et al.* observed competitive reduction of several anodically generated cations during the electroreduction of p-methoxyisopropylbenzene.[233]

Symptoms of competitive reduction

Competitive reduction of anodically generated cations is most often evidenced by lower-than-expected product yields and low Faradaic efficiency, especially in constant current electrolysis. Depending on the possibility and nature of substrate reduction (chemical or electrochemical) at the plated metal, competitive reduction may result in low substrate conversion, full conversion but an unexpected product distribution, or degradation of the substrate and/or products as described in previous sections. Cathode fouling may also be observed, though whether or not the metal deposition is visible by eye will depend on the size of the deposits and extent of deposition.

Diagnosing the problem

Depending on the extent of metal deposition, microscopy techniques may be required to confirm that competitive cation reduction is occurring. SEM and EDS can easily identify micron-sized metal deposits and spatially map the elemental composition of the surface, which will indicate whether the reduced cations cover the entire cathode surface or whether the original cathode material is still accessible.[234] Once cross-plating is confirmed, electrochemical techniques can be used to determine if the cross-plating limits yields by any mechanism other than competition for electrons. Cyclic voltammetry (CV) experiments will indicate the reduction potentials of individual components in the system, including the substrate(s) and anodically generated cations. A reference electrode or non-interfering reference couple is required to accurately determine the relative reduction potentials of each component. Conducting CV experiments before electrolysis can hint at whether competitive reduction will occur during electrolysis — if the metal cation is reduced at a potential that is similar to or more positive than the substrate or catalyst to be reduced during electrolysis, competitive reduction is likely to occur.

Troubleshooting the problem

Competitive reduction can be prevented most easily by switching to a sacrificial anode with a more negative reduction potential. However, in many cases, using a more reducing metal introduces additional complications as described in the previous three sections. If an anode with a mild reduction potential must be used to prevent substrate degradation or anodic passivation, a divided cell can physically separate the anode and cathode, preventing cross-plating and short circuits.[228]

If the reduction potential of the anodically generated cations is more negative than that of the substrate but competitive reduction still occurs during constant current electrolysis, then reduction of the cation is kinetically faster than reduction of the substrate. In this situation, instead of performing constant current electrolysis, electrolysis can be conducted at a constant potential which is more negative than the reduction potential of the substrate but less negative than that of the anodically generated cation. Constant potential electrolysis can thus improve selectivity for substrate reduction over cation reduction.[137] Conducting electrolysis at a constant potential prevents reduction reactions that are less thermodynamically accessible (i.e., the reduction of species with more negative reduction potentials,) but longer electrolysis times may be required to fully reduce the substrate. In a constant potential reductive electrolysis, the anode/counter electrode should only be used as the reference electrode (i.e., in a two-electrode cell) in cases where no electrode passivation or undesired reactivity is observed. Otherwise, the potential will drift at the counter/reference electrode, which will cause the working electrode to experience more oxidizing conditions than initially expected.

As in the case of side reactions between the anode and the substrate, it is important to acknowledge that cross-plating of anodically generated cations can be beneficial in some reactions. In certain cases, plating at the cathode generates active sites for important chemical and electrochemical transformations (Figure 5.8d). For example, Huang *et al.* found that Zn particles deposited at the cathode from sacrificial anode cations mediate the allylation of aldehydes in aqueous ammonia solutions by forming nucleophilic allylzinc species at the electrode surface.[234] Similarly, reduction of anodically generated Zn^{2+} can form nanostructured Zn at the cathode, which can mediate the electroreduction of epoxides to alkenes and of imines and alkyl halides to amines.[235, 236] Reduction of cations from the sacrificial anode can also pin the cathodic potential at such a level as to avoid over-reducing the substrate to undesired products. In a constant current

experiment, the electrode potentials are controlled by the potentials of the fastest oxidation and reduction events. Deposition of an easily reducible metal can thus prevent extreme reducing potentials that would degrade products at the cathode, albeit while reducing Faradaic efficiency. Gosmini *et al.* observed that reducing anodically generated Zn at the cathode kept the cathode potential high enough to prevent direct reduction of an aryl halide species and instead promoted the desired cross-coupling of aryl halides with 2-halopyridine.[237] Similarly, in the electrochemical carboxylation of benzal diacetates, Senboku *et al.* found that reduction of anodically generated Zn^{2+} at the cathode prevented extreme cathodic potentials that would lead to over-reduction of the desired metal acetate product.[238] Cross-plated cations generated at the sacrificial anode can play a role in the reductive synthetic reaction; this synergy can be considered a form of paired electrolysis.

5.6 Summary and Outlook

Although the oxidation of a sacrificial metal anode is assumed to be a straightforward and simple counter reaction, processes involving the anode are integral to the overall reaction and can dictate the success or failure of an electrosynthetic transformation. To develop robust electrochemically-driven reactions, the chemistry at the anode must be understood and optimized alongside the cathodic reaction. The chemical and electrochemical effects of the sacrificial anode processes affect every aspect of the synthetic reaction, from the Faradaic efficiency to the scalability to the stability of the substrate and reactants. Sacrificial anode chemistry cannot be ignored in reaction optimization.

A major roadblock to the development of effective half reactions using sacrificial anodes is the relative lack of data on the anodes. It is not sufficient to report only the best-performing sacrificial anode in an optimization table, even if a reaction fails exclusively because of an anodic process and not because of anything related to the reductive reaction of interest. At minimum, several of the most common sacrificial anodes should be screened, and a description of the behavior of each anode under a given set of reaction conditions should be reported in the supporting information. In particular, visible fouling of either electrode and changes in the product distribution that are directly tied to the anode chemistry should be highlighted. Only by reporting both successes and failures with different sacrificial anodes can the process of optimizing the anode chemistry be streamlined in future reactions.

Though visual observations are useful to begin troubleshooting issues at the anode, more detailed analytical data are necessary to develop a fundamental understanding of the anodic processes and how they influence the cathodic reaction. Though some instruments have been optimized to enable inexpensive and rapid screening of synthetic conditions, they are often insufficient for analytical characterization of electrochemical processes at either electrode, especially when screening multiple sacrificial anodes. Control over potential or current across multiple cells with reference electrodes and the ability to analyze the electrochemical data are required for exploring and understanding sacrificial anode processes in more detail.

To date, most of the analysis of sacrificial anode behavior has been conducted for reactions run in THF as the solvent. Moving forward, more attention should be paid to anode processes in other commonly used solvents, such as acetonitrile and N,N-dimethylformamide. The higher donor number and coordinating ability of these solvents may affect the solubility of the sacrificial cations and their corresponding salts, as well as the nature of the surface film formed at the anode. New electrolyte design strategies may be required to enable effective metal oxidation in solvents other than THF.

In addition to electrolyte design strategies, altering the chemistry of the anode itself may enable new reactivity. Ionically conductive but electronically insulating surface coatings, similar to SEIs on battery anodes, could permit efficient metal stripping while minimizing chemical or electrochemical degradation of electrolyte components at the anode surface.[220] Such surface layers can be generated *in situ* from reactions between the metal and the electrolyte or *ex situ* through solid state synthesis or reaction in a different solution than the one used for reductive electrosynthesis. Native SEIs, i.e., those formed in contact with electrolyte, and artificial SEIs on metals commonly used as sacrificial anodes (Mg, Zn, Al) are being studied in the battery literature; this research can provide a starting point for the development of surface coatings for use in electrosynthesis.

Alternatively, new nonmetallic anodes can be designed to mitigate or prevent the common failure mechanisms detailed here. Materials that undergo oxidative deintercalation mechanisms, for instance, exhibit a wide range of chemical potentials allowing the potential at the anode to be tuned. Further, the deintercalation reactions can generate a variety of different cations in solution depending on the application. Our group is currently working toward these goals.

Many strategies for improving sacrificial anode performance involve introducing new species or tunable parameters, adding to the already long list of variables that must be optimized in each reaction. In the future, machine learning may assist in predicting the performance of a particular sacrificial anode under a given set of reaction conditions.[239] Such predictive technology presents an attractive complement to traditional synthetic screening experiments. However, to effectively train a model to predict sacrificial anode behavior, both successful and failed reactions must be reported in the literature. A balanced training set requires high-quality data on the anode chemistry for each reaction conducted in the optimization of the sacrificial anode, even if the reaction results in low product yields.

Although sacrificial anodes will continue to be necessary for optimizing individual half reactions, the long-term goal of electrosynthesis is to move towards a paired electrolysis setup to maximize atom economy by taking advantage of desirable reactions at both electrodes. The processes at each electrode can be related if targeting a convergent electrosynthesis procedure, but the two half reactions are not required to contribute to the same overall transformation as long as neither reaction is deleterious to the other.[121] Before incorporating a reductive reaction into a paired electrolysis setup, detailed mechanistic studies must first be undertaken to ensure that the sacrificial anode and its byproducts are not required for the reductive reaction to proceed. Divided cell studies which separate the sacrificial anode cations from the reductive reaction are particularly instructive in these cases.

Ultimately, a deep understanding of sacrificial anode behavior in electrosynthetic conditions and the development of experimental guidelines for sacrificial anode choice will require cross-disciplinary collaborations between synthetic chemists, electrochemists, and surface scientists. A thorough understanding of sacrificial anode chemistry will streamline reaction optimization and expand the chemical space compatible with electrosynthetic reactions. We hope that by addressing the major pitfalls described herein, sacrificial anodes will not limit the development of new and interesting reductive electrochemistry.

Chapter 6

PERSPECTIVE AND OUTLOOK

This thesis probes the effect of supporting electrolyte design and composition on electrochemical performance in both energy storage and electrosynthesis applications. Several electrolytes and additives have been explored to control interfacial reactivity, tailor the composition of the surface film at a metal electrode, promote reduction of an analyte, or prevent unwanted metal deposition. In Chapter 2, we find that a highly concentrated supporting electrolyte limits electrolyte decomposition and polysulfide shuttling in Li-S batteries, promoting new high-temperature cycling applications. In Chapter 3, the size and coordination strength of the supporting electrolyte anion is shown to affect the redox potential of Sm complexes for use in electrocatalytic systems. In Chapter 4, crown ethers are shown to slightly increase the Zn^{2+} deposition overpotential, laying groundwork for the use of Zn sacrificial anodes in deep reductive electrosynthesis. Finally, Chapter 5 integrates lessons from electrochemistry, surface characterization, and organic synthesis to present a guide to troubleshooting sacrificial anodes in electrosynthetic reactions, providing several strategies to ensure that reductive reactions are not limited by anodic processes.

The current state of research on the solid-electrolyte interphase (SEI) that forms between battery anodes and the supporting electrolyte suggests that further investigation of surface film formation on multivalent metal anodes would expand the range of electrolytes that can be used in multivalent batteries. The exact structure and composition of an individual SEI is difficult to ascertain conclusively due to its often heterogeneous structure and to the changes that occur when the electrode is removed from the cell. For most metal anode batteries that exist today, certain components of the SEI have been linked to favorable or poor electrochemical performance. The SEIs that form on Li metal have been fairly well studied over the past several years, but the SEIs that develop on multivalent metal anodes are less well understood because multivalent ion conduction through the SEI is difficult due to the ion's higher charge density and larger size.

Multivalent ion conduction through the SEI or surface film also limits the use of metal sacrificial anodes in organic electrosynthesis. The chemistry of the sacrificial anode itself has only recently come under intense study, and electrolyte composi-

tion plays a significant role in the formation of a non-insulating surface film. To date, reactions at a sacrificial anode have only been studied in detail for syntheses conducted in THF. The electrolyte design strategies that prevent anode passivation may not be applicable in other solvents or under certain synthetic conditions, and new strategies must be developed as these challenges arise.

A deeper understanding of metal deposition and dissolution in multiple solvents, in the presence of various supporting electrolytes, and under different synthetic conditions will enable the development of new electrosynthetic reactions and new battery chemistries. Several approaches can expand our understanding of interfacial reactions between the electrode and electrolyte and the electrolyte's effect on reductive electrosynthetic reactions.

First, the chemical composition of the interfaces and interphases that form at various metal anodes in different solvents can be investigated to develop a batter understanding of chemical reactivity between the metals, solvents, and supporting electrolyte salts. Metals such as Mg, Al, and Zn are commonly used as sacrificial anodes in electrosynthesis and as battery anodes, but other metals like Cu, Fe, and Ni are also frequently employed in electrosynthesis and are worthy of further investigation. The surface composition can be probed by imaging, elemental analysis, and spectroscopic techniques, and computational studies offer an opportunity to investigate multivalent ion conduction in various components of the surface film. *In situ* or *operando* characterization of the surface film and its evolution during electrosynthesis or battery cycling is particularly interesting as this characterization would elucidate the film's formation pathways and composition inside the cell, without confounding factors that arise during transfer and analysis.

Electrolyte tailoring strategies can be adopted to promote ionic conductivity in the interphase or to limit deleterious electrolyte decomposition. Various additives can modulate the deposition and dissolution overpotentials at the metal anode. These additives can promote the oxidation of metal sacrificial anodes, form ionically conductive interphases at the metal-electrolyte interface, and prevent unwanted cation reduction at the cathode. However, the additives themselves should be inert to the reductive chemistry of interest. Ideally, the electrolyte could be tailored to target a specific surface composition that permits clean metal plating and stripping without affecting other reactions in the cell.

One strategy for targeting specific surface films is to generate the surface film *ex situ*. This strategy has been previously employed in Li metal batteries — and to

a lesser extent in Mg, Na, and K batteries — to create artificial SEIs that permit efficient metal stripping and plating while limiting electrolyte decomposition.[22, 240–242] A similar approach can tailor the electrode-electrolyte interface on other metal anodes for use in batteries or in electrosynthesis. Artificial surface films are especially interesting because the additives, solvents, and electrolyte salts used to generate the surface film do not need to be compatible with the reaction conditions in which the newly coated anode will be used. The anode electrochemistry can thus be optimized independently of the synthetic reaction of interest. Artificial surface coatings may therefore enable the use of electrodes that would otherwise be chemically incompatible with the electrolyte itself. For example, a surface film that conducts Li^+ but blocks contact between Li metal and the electrolyte solution could enable Li sacrificial anodes in electrosynthesis.

Combining knowledge from battery chemistry and SEI design with strategies for electrolyte tailoring in organic electrosynthesis could accelerate and improve research outcomes in both fields. Thorough investigation of reactivity between commonly used metal anodes and various solvents, salts, and additives will promote greater understanding of metal-electrolyte interface chemistry and enable a broad range of applications for nonaqueous electrochemistry.

BIBLIOGRAPHY

(1) Anastas, P.; Eghbali, N. Green Chemistry: Principles and Practice. *Chem. Soc. Rev.* **2010**, *39*, 301–312.

(2) Anastas, P. T.; Warner, J. C., *Green Chemistry: Theory and Practice*; Oxford University Press: 1998.

(3) Frontana-Uribe, B. A.; Little, R. D.; Ibanez, J. G.; Palma, A.; Vasquez-Medrano, R. Organic Electrosynthesis: A Promising Green Methodology in Organic Chemistry. *Green Chem.* **2010**, *12*, 2099–2119.

(4) Matthews, M. A. Green Electrochemistry. Examples and Challenges. *Pure Appl. Chem.* **2001**, *73*, 1305–1308.

(5) Sbei, N.; Hardwick, T.; Ahmed, N. Green Chemistry: Electrochemical Organic Transformations via Paired Electrolysis. *ACS Sustainable Chem. Eng.* **2021**, *9*, 6148–6169.

(6) Ye, T.; Li, L.; Zhang, Y. Recent Progress in Solid Electrolytes for Energy Storage Devices. *Adv. Funct. Mater.* **2020**, *30*, 2000077.

(7) Zheng, F.; Kotobuki, M.; Song, S.; Lai, M. O.; Lu, L. Review on Solid Electrolytes for All-Solid-State Lithium-Ion Batteries. *J. Power Sources* **2018**, *389*, 198–213.

(8) Galiński, M.; Lewandowski, A.; Stępniak, I. Ionic Liquids as Electrolytes. *Electrochim. Acta* **2006**, *51*, 5567–5580.

(9) Zheng, Y.; Wang, D.; Kaushik, S.; Zhang, S.; Wada, T.; Hwang, J.; Matsumoto, K.; Hagiwara, R. Ionic Liquid Electrolytes for Next-generation Electrochemical Energy Devices. *EnergyChem* **2022**, *4*, 100075.

(10) Lakshmanan, S.; Murugesan, T. The Chlor-Alkali Process: Work in Progress. *Clean Techn. Environ. Policy* **2014**, *16*, 225–234.

(11) Ma, I. A. W.; Ammar, S.; Kumar, S. S. A.; Ramesh, K.; Ramesh, S. A Concise Review on Corrosion Inhibitors: Types, Mechanisms and Electrochemical Evaluation Studies. *J. Coat. Technol. Res.* **2022**, *19*, 241–268.

(12) Roth, H. G.; Romero, N. A.; Nicewicz, D. A. Experimental and Calculated Electrochemical Potentials of Common Organic Molecules for Applications to Single-Electron Redox Chemistry. *Synlett* **2016**, *27*, 714–723.

(13) Chen, M.; Zhang, J.; Ji, X.; Fu, J.; Feng, G. Progress on Predicting the Electrochemical Stability Window of Electrolytes. *Curr. Opin. Electrochem.* **2022**, *34*, 101030.

(14) Kasnatscheew, J.; Streipert, B.; Röser, S.; Wagner, R.; Laskovic, I. C.; Winter, M. Determining Oxidative Stability of Battery Electrolytes: Validity of Common Electrochemical Stability Window (ESW) Data and Alternative Strategies. *Phys. Chem. Chem. Phys.* **2017**, *19*, 16078–16086.

(15) Fan, X.; Wang, C. High-Voltage Liquid Electrolytes for Li Batteries: Progress and Perspectives. *Chem. Soc. Rev.* **2021**, *50*, 10486–10566.

(16) Tan, S.; Ji, Y. J.; Zhang, Z. R.; Yang, Y. Recent Progress in Research on High-Voltage Electrolytes for Lithium-Ion Batteries. *ChemPhysChem* **2014**, *15*, 1956–1969.

(17) Song, G.; Atrens, A. Recent Insights into the Mechanism of Magnesium Corrosion and Research Suggestions. *Adv. Eng. Mater.* **2007**, *9*, 177–183.

(18) Yan, M.; Kawamata, Y.; Baran, P. S. Synthetic Organic Electrochemical Methods Since 2000: On the Verge of a Renaissance. *Chem. Rev.* **2017**, *117*, 13230–13319.

(19) An, S. J.; Li, J.; Daniel, C.; Mohanty, D.; Nagpure, S.; Wood, D. L. The State of Understanding of the Lithium-Ion-Battery Graphite Solid Electrolyte Interphase (SEI) and Its Relationship to Formation Cycling. *Carbon* **2016**, *105*, 52–76.

(20) Agubra, V. A.; Fergus, J. W. The Formation and Stability of the Solid Electrolyte Interface on the Graphite Anode. *Journal of Power Sources* **2014**, *268*, 153–162.

(21) Attias, R.; Salama, M.; Hirsch, B.; Goffer, Y.; Aurbach, D. Anode-Electrolyte Interfaces in Secondary Magnesium Batteries. *Joule* **2019**, *3*, 27–52.

(22) Sun, Y.; Ai, F.; Lu, Y.-C. Electrolyte and Interphase Design for Magnesium Anode: Major Challenges and Perspectives. *Small* **2022**, *18*, 2200009.

(23) Liang, Z.; Ban, C. Strategies to Enable Reversible Magnesium Electrochemistry: From Electrolytes to Artificial Solid–Electrolyte Interphases. *Angew. Chem. Int. Ed.* **2021**, *60*, 11036–11047.

(24) Scrosati, B.; Garche, J. Lithium Batteries: Status, Prospects and Future. *J. Power Sources* **2010**, *195*, 2419–2430.

(25) Cabana, J.; Monconduit, L.; Larcher, D.; Palacín, M. R. Beyond Intercalation-Based Li-Ion Batteries: The State of the Art and Challenges of Electrode Materials Reacting Through Conversion Reactions. *Adv. Mater.* **2010**, *22*, E170–E192.

(26) Armand, M.; Tarascon, J.-M. Building Better Batteries. *Nature* **2008**, *451*, 652–657.

(27) Thackeray, M. M.; Wolverton, C.; Isaacs, E. D. Electrical Energy Storage for Transportation—Approaching the Limits of, and Going beyond, Lithium-Ion Batteries. *Energy Environ. Sci.* **2012**, *5*, 7854–7863.

(28) Dörfler, S.; Walus, S.; Locke, J.; Fotouhi, A.; Auger, D. J.; Shateri, N.; Abendroth, T.; Härtel, P.; Althues, H.; Kaskel, S. Recent Progress and Emerging Application Areas for Lithium–Sulfur Battery Technology. *Energy Technol.* **2021**, *9*, 2000694.

(29) Fotouhi, A.; Auger, D. J.; O'Neill, L.; Cleaver, T.; Walus, S. Lithium-Sulfur Battery Technology Readiness and Applications—A Review. *Energies* **2017**, *10*, 1937.

(30) Yoo, H. D.; Shterenberg, I.; Gofer, Y.; Gershinsky, G.; Pour, N.; Aurbach, D. Mg Rechargeable Batteries: An on-Going Challenge. *Energy Environ. Sci.* **2013**, *6*, 2265–2279.

(31) Wang, J.; Wang, Y.; He, X.; Ren, J.; Jiang, C.; Wan, C. Electrochemical Characteristics of Sulfur Composite Cathode Materials in Rechargeable Lithium Batteries. *J. Power Sources* **2004**, *138*, 271–273.

(32) Cheng, X.-B.; Zhang, R.; Zhao, C.-Z.; Wei, F.; Zhang, J.-G.; Zhang, Q. A Review of Solid Electrolyte Interphases on Lithium Metal Anode. *Adv. Sci.* **2016**, *3*, 1500213.

(33) Mistry, A. N.; Mukherjee, P. P. "Shuttle" in Polysulfide Shuttle: Friend or Foe? *J. Phys. Chem. C* **2018**, *122*, 23845–23851.

(34) Mikhaylik, Y. V.; Akridge, J. R. Polysulfide Shuttle Study in the Li/S Battery System. *J. Electrochem. Soc.* **2004**, *151*, A1969.

(35) Cuisinier, M.; Cabelguen, P.-E.; Adams, B. D.; Garsuch, A.; Balasubramanian, M.; Nazar, L. F. Unique Behaviour of Nonsolvents for Polysulphides in Lithium–Sulphur Batteries. *Energy Environ. Sci.* **2014**, *7*, 2697–2705.

(36) Yamada, Y.; Furukawa, K.; Sodeyama, K.; Kikuchi, K.; Yaegashi, M.; Tateyama, Y.; Yamada, A. Unusual Stability of Acetonitrile-Based Superconcentrated Electrolytes for Fast-Charging Lithium-Ion Batteries. *J. Am. Chem. Soc.* **2014**, *136*, 5039–5046.

(37) Seo, D. M.; Borodin, O.; Han, S.-D.; Boyle, P. D.; Henderson, W. A. Electrolyte Solvation and Ionic Association II. Acetonitrile-Lithium Salt Mixtures: Highly Dissociated Salts. *J. Electrochem. Soc.* **2012**, *159*, A1489–A1500.

(38) Nilsson, V.; Younesi, R.; Brandell, D.; Edström, K.; Johansson, P. Critical Evaluation of the Stability of Highly Concentrated LiTFSI - Acetonitrile Electrolytes vs. Graphite, Lithium Metal and LiFePO4 Electrodes. *J. Power Sources* **2018**, *384*, 334–341.

(39) Cheng, L.; Curtiss, L. A.; Zavadil, K. R.; Gewirth, A. A.; Shao, Y.; Gallagher, K. G. Sparingly Solvating Electrolytes for High Energy Density Lithium–Sulfur Batteries. *ACS Energy Lett.* **2016**, *1*, 503–509.

(40) Dokko, K.; Tachikawa, N.; Yamauchi, K.; Tsuchiya, M.; Yamazaki, A.; Takashima, E.; Park, J.-W.; Ueno, K.; Seki, S.; Serizawa, N.; Watanabe, M. Solvate Ionic Liquid Electrolyte for Li–S Batteries. *J. Electrochem. Soc.* **2013**, *160*, A1304–A1310.

(41) Pang, Q.; Shyamsunder, A.; Narayanan, B.; Kwok, C. Y.; Curtiss, L. A.; Nazar, L. F. Tuning the Electrolyte Network Structure to Invoke Quasi-Solid State Sulfur Conversion and Suppress Lithium Dendrite Formation in Li–S Batteries. *Nat. Energy* **2018**, *3*, 783–791.

(42) See, K. A.; Wu, H.-L.; Lau, K. C.; Shin, M.; Cheng, L.; Balasubramanian, M.; Gallagher, K. G.; Curtiss, L. A.; Gewirth, A. A. Effect of Hydrofluoroether Cosolvent Addition on Li Solvation in Acetonitrile-Based Solvate Electrolytes and Its Influence on S Reduction in a Li–S Battery. *ACS Appl. Mater. Interfaces* **2016**, *8*, 34360–34371.

(43) Zasova, L. V.; Ignatiev, N.; Khatuntsev, I.; Linkin, V. Structure of the Venus Atmosphere. *Planet. Space Sci.* **2007**, *55*, 1712–1728.

(44) Jones, J.-P.; Hennessy, J.; Billings, K. J.; Krause, F. C.; Pasalic, J.; Bugga, R. V. Communication—Atomic Layer Deposition of Aluminum Fluoride for Lithium Metal Anodes. *J. Electrochem. Soc.* **2020**, *167*, 060502.

(45) Deng, Z.; Zhang, Z.; Lai, Y.; Liu, J.; Li, J.; Liu, Y. Electrochemical Impedance Spectroscopy Study of a Lithium/Sulfur Battery: Modeling and Analysis of Capacity Fading. *J. Electrochem. Soc.* **2013**, *160*, A553.

(46) Trinh, N. D.; Lepage, D.; Aymé-Perrot, D.; Badia, A.; Dollé, M.; Rochefort, D. An Artificial Lithium Protective Layer That Enables the Use of Acetonitrile-Based Electrolytes in Lithium Metal Batteries. *Angew. Chem. Int. Ed.* **2018**, *57*, 5072–5075.

(47) Rupich, M. W.; Pitts, L.; Abraham, K. M. Characterization of Reactions and Products of the Discharge and Forced Overdischarge of Li / SO 2 Cells. *J. Electrochem. Soc.* **1982**, *129*, 1857–1861.

(48) Neelakantan, P. Raman Spectrum of Acetonitrile. *Proc. Indian Acad. Sci.* **1964**, *60*, 422–424.

(49) Contarini, S.; Rabalais, J. W. Ion Bombardment-Induced Decomposition of Li and Ba Sulfates and Carbonates Studied by X-ray Photoelectron Spectroscopy. *J. Electron Spectros. Relat. Phenomena* **1985**, *35*, 191–201.

(50) Chowdari, B. V. R.; Tan, K. L.; Chia, W. T.; Gopalakrishnan, R. Thermal, Physical, Electrical and XPS Studies of the Li2O:P2O5: MoO3 Glass System. *J. Non-Cryst. Solids* **1991**, *128*, 18–29.

(51) Sexton, B. A.; Avery, N. R. Coordination of Acetonitrile (CH3CN) to Platinum (111): Evidence for an *H*2(C, N) Species. *Surf. Sci.* **1983**, *129*, 21–36.

(52) Hamrin, K.; Johansson, G.; Gelius, U.; Nordling, C.; Siegbahn, K. Valence Bands and Core Levels of the Isoelectronic Series LiF, BeO, BN, and Graphite Studied by ESCA. *Phys. Scr.* **1970**, *1*, 277–280.

(53) Li, N.-W.; Yin, Y.-X.; Li, J.-Y.; Zhang, C.-H.; Guo, Y.-G. Passivation of Lithium Metal Anode via Hybrid Ionic Liquid Electrolyte toward Stable Li Plating/Stripping. *Adv. Sci.* **2017**, *4*, 1600400.

(54) Zhang, W.; Zhang, S.; Fan, L.; Gao, L.; Kong, X.; Li, S.; Li, J.; Hong, X.; Lu, Y. Tuning the LUMO Energy of an Organic Interphase to Stabilize Lithium Metal Batteries. *ACS Energy Lett.* **2019**, *4*, 644–650.

(55) Bournel, F.; Laffon, C.; Parent, P.; Tourillon, G. Adsorption of Some Substituted Ethylene Molecules on Pt(111) at 95 K Part 1: NEXAFS, XPS and UPS Studies. *Surf. Sci.* **1996**, *350*, 60–78.

(56) Shuttleworth, D. Preparation of Metal-Polymer Dispersions by Plasma Techniques. An ESCA Investigation. *J. Phys. Chem.* **1980**, *84*, 1629–1634.

(57) Yamin, H.; Gorenshtein, A.; Penciner, J.; Sternberg, Y.; Peled, E. Lithium Sulfur Battery Oxidation/Reduction Mechanisms of Polysulfides in THF Solutions. *J. Electrochem. Soc.* **1988**, *135*, 1045–1048.

(58) Cheon, S.-E.; Ko, K.-S.; Cho, J.-H.; Kim, S.-W.; Chin, E.-Y.; Kim, H.-T. Rechargeable Lithium Sulfur Battery I. Structural Change of Sulfur Cathode During Discharge and Charge. *J. Electrochem. Soc.* **2003**, *150*, A796–A799.

(59) Lee, C.-W.; Pang, Q.; Ha, S.; Cheng, L.; Han, S.-D.; Zavadil, K. R.; Gallagher, K. G.; Nazar, L. F.; Balasubramanian, M. Directing the Lithium–Sulfur Reaction Pathway via Sparingly Solvating Electrolytes for High Energy Density Batteries. *ACS Cent. Sci.* **2017**, *3*, 605–613.

(60) Ding, F.; Xu, W.; Choi, D.; Wang, W.; Li, X.; Engelhard, M. H.; Chen, X.; Yang, Z.; Zhang, J.-G. Enhanced Performance of Graphite Anode Materials by AlF3 Coating for Lithium-Ion Batteries. *J. Mater. Chem.* **2012**, *22*, 12745–12751.

(61) Owen, N.; Zhang, Q. Investigations of Aluminum Fluoride as a New Cathode Material for Lithium-Ion Batteries. *J. Appl. Electrochem.* **2017**, *47*, 417–431.

(62) Sun, Y.-K.; Lee, M.-J.; Yoon, C. S.; Hassoun, J.; Amine, K.; Scrosati, B. The Role of AlF3 Coatings in Improving Electrochemical Cycling of Li-Enriched Nickel-Manganese Oxide Electrodes for Li-Ion Batteries. *Adv. Mater.* **2012**, *24*, 1192–1196.

(63) Hess, A.; Kemnitz, E.; Lippitz, A.; Unger, W. E. S.; Menz, D. H. ESCA, XRD, and IR Characterization of Aluminum Oxide, Hydroxyfluoride, and Fluoride Surfaces in Correlation with Their Catalytic Activity in Heterogeneous Halogen Exchange Reactions. *J. Catal.* **1994**, *148*, 270–280.

(64) Girard, P.; Namy, J. L.; Kagan, H. B. Divalent Lanthanide Derivatives in Organic Synthesis. 1. Mild Preparation of Samarium Iodide and Ytterbium Iodide and Their Use as Reducing or Coupling Agents. *J. Am. Chem. Soc.* **1980**, *102*, 2693–2698.

(65) Szostak, M.; Fazakerley, N. J.; Parmar, D.; Procter, D. J. Cross-Coupling Reactions Using Samarium(II) Iodide. *Chem. Rev.* **2014**, *114*, 5959–6039.

(66) Cha, J. Y.; Yeoman, J. T. S.; Reisman, S. E. A Concise Total Synthesis of (-)-Maoecrystal Z. *J. Am. Chem. Soc.* **2011**, *133*, 14964–14967.

(67) Hebri, H.; Duñach, E.; Périchon, J. SmCl3-catalysed Electrosynthesis of γ-Butyrolactones from 3-Chloroesters and Carbonyl Compounds. *J. Chem. Soc., Chem. Commun.* **1993**, 499–500.

(68) Bingham, T. W.; Hernandez, L. W.; Olson, D. G.; Svec, R. L.; Hergenrother, P. J.; Sarlah, D. Enantioselective Synthesis of Isocarbostyril Alkaloids and Analogs Using Catalytic Dearomative Functionalization of Benzene. *J. Am. Chem. Soc.* **2019**, *141*, 657–670.

(69) Mei, R.; Sauermann, N.; Oliveira, J. C. A.; Ackermann, L. Electroremovable Traceless Hydrazides for Cobalt-Catalyzed Electro-Oxidative C–H/N–H Activation with Internal Alkynes. *J. Am. Chem. Soc.* **2018**, *140*, 7913–7921.

(70) Fukaya, K. et al. Synthesis of Paclitaxel. 1. Synthesis of the ABC Ring of Paclitaxel by SmI2-Mediated Cyclization. *Org. Lett.* **2015**, *17*, 2570–2573.

(71) Nicolaou, K. C.; Ellery, S. P.; Chen, J. S. Samarium Diiodide Mediated Reactions in Total Synthesis. *Angew. Chem. Int. Ed.* **2009**, *48*, 7140–7165.

(72) Edmonds, D. J.; Johnston, D.; Procter, D. J. Samarium(II)-Iodide-Mediated Cyclizations in Natural Product Synthesis. *Chem. Rev.* **2004**, *104*, 3371–3404.

(73) Heravi, M. M.; Nazari, A. Samarium(II) Iodide-Mediated Reactions Applied to Natural Product Total Synthesis. *RSC Adv.* **2022**, *12*, 9944–9994.

(74) Szostak, M.; Spain, M.; Procter, D. J. Preparation of Samarium(II) Iodide: Quantitative Evaluation of the Effect of Water, Oxygen, and Peroxide Content, Preparative Methods, and the Activation of Samarium Metal. *J. Org. Chem.* **2012**, *77*, 3049–3059.

(75) Aspinall, H. C.; Greeves, N.; Valla, C. Samarium Diiodide-Catalyzed Diastereoselective Pinacol Couplings. *Org. Lett.* **2005**, *7*, 1919–1922.

(76) Bhatt, A. I.; May, I.; Volkovich, V. A.; Collison, D.; Helliwell, M.; Polovov, I. B.; Lewin, R. G. Structural Characterization of a Lanthanum Bistriflimide Complex, La(N(SO2CF3)2)3(H2O)3, and an Investigation of La, Sm, and Eu Electrochemistry in a Room-Temperature Ionic Liquid, [Me3NnBu][N(SO2CF3)2]. *Inorg. Chem.* **2005**, *44*, 4934–4940.

(77) Castrillejo, Y.; Fernández, P.; Medina, J.; Hernández, P.; Barrado, E. Electrochemical Extraction of Samarium from Molten Chlorides in Pyrochemical Processes. *Electrochim. Acta* **2011**, *56*, 8638–8644.

(78) Massot, L.; Chamelot, P.; Taxil, P. Cathodic Behaviour of Samarium(III) in LiF–CaF2 Media on Molybdenum and Nickel Electrodes. *Electrochim. Acta* **2005**, *50*, 5510–5517.

(79) Léonard, E.; Duñach, E.; Périchon, J. First Samarium-Catalysed Coupling of Aldehydes and Ketones. *J. Chem. Soc. Chem. Commun.* **1989**, *0*, 276–277.

(80) Hebri, H.; Duñach, E.; Périchon, J. Samarium-Catalyzed Electrochemical Reduction of Organic Halides. *Synth. Commun.* **1991**, *21*, 2377–2382.

(81) Hébri, H.; Duñach, E.; Heintz, M.; Troupel, M.; Périchon, J. Samarium-Catalyzed Electrosynthesis of 1,2-Diketones by the Direct Reductive Dimerization of Aromatic Esters: A Novel Coupling Reaction. *Synlett* **1991**, *1991*, 901–902.

(82) Espanet, B.; Duñach, E.; Périchon, J. SmCl3-catalyzed Electrochemical Cleavage of Allyl Ethers. *Tetrahedron Lett.* **1992**, *33*, 2485–2488.

(83) Hébri, H.; Duñach, E.; Périchon, J. Samarium-Catalyzed Electrochemical Cyanomethylation of Esters. *Synlett* **1992**, *1992*, 293–294.

(84) Miller, R. S.; Sealy, J. M.; Shabangi, M.; Kuhlman, M. L.; Fuchs, J. R.; Flowers, R. A. Reactions of SmI2 with Alkyl Halides and Ketones: Inner-Sphere vs Outer-Sphere Electron Transfer in Reactions of Sm(II) Reductants. *J. Am. Chem. Soc.* **2000**, *122*, 7718–7722.

(85) Parrish, J. D.; Little, R. D. Electrochemical Generation of Low-Valent Lanthanides. *Tetrahedron Lett.* **2001**, *42*, 7767–7770.

(86) Sun, L.; Sahloul, K.; Mellah, M. Use of Electrochemistry to Provide Efficient SmI2 Catalytic System for Coupling Reactions. *ACS Catal.* **2013**, *3*, 2568–2573.

(87) Arashiba, K.; Kanega, R.; Himeda, Y.; Nishibayashi, Y. Electrochemical Reduction of Samarium Triiodide into Samarium Diiodide. *Chem. Lett.* **2020**, *49*, 1171–1173.

(88) Enemærke, R. J.; Hertz, T.; Skrydstrup, T.; Daasbjerg, K. Evidence for Ionic Samarium(II) Species in THF/HMPA Solution and Investigation of Their Electron-Donating Properties. *Chem. – Eur. J.* **2000**, *6*, 3747–3754.

(89) Connelly, N. G.; Geiger, W. E. Chemical Redox Agents for Organometallic Chemistry. *Chem. Rev.* **1996**, *96*, 877–910.

(90) Dahlén, A.; Hilmersson, G. Microwave-Assisted Generation of Lanthanide(II) Halides in THF and Simple Quantitative Determination. *Eur. J. Inorg. Chem.* **2004**, *2004*, 3020–3024.

(91) Fang, J.; Wang, D.; Deng, G.-J.; Gong, H. Transition Metal-Free Protodecarboxylation of Electron Rich Aromatic Acids under Mild Conditions. *Tetrahedron Lett.* **2017**, *58*, 4503–4506.

(92) Mitsudo, K.; Kaide, T.; Nakamoto, E.; Yoshida, K.; Tanaka, H. Electrochemical Generation of Cationic Pd Catalysts and Application to Pd/TEMPO Double-Mediatory Electrooxidative Wacker-Type Reactions. *J. Am. Chem. Soc.* **2007**, *129*, 2246–2247.

(93) Shi, L.; Tu, Y.-Q.; Wang, M.; Zhang, F.-M.; Fan, C.-A.; Zhao, Y.-M.; Xia, W.-J. A Reaction for Sp3-sp3 C-C Bond Formation via Cooperation of Lewis Acid-Promoted/Rh-Catalyzed C-H Bond Activation. *J. Am. Chem. Soc.* **2005**, *127*, 10836–10837.

(94) Batsanov, A. S.; Bruce, J. I.; Ganesh, T.; Low, P. J.; Kataky, R.; Puschmann, H.; Steel, P. G. Synthesis, Characterisation and Application of Lanthanide Cyclen Complexes in Organic Synthesis. *J. Chem. Soc., Perkin Trans. 1* **2002**, 932–937.

(95) Cabrera, A.; Salmón, M.; Rosas, N.; Pérez-Flores, J.; Velasco, L.; Espinosa-Pérez, G.; Arias, J. L. Characterization of a Novel [Sm(HMPA)4I2]I Complex by Positive Ion Fast Atom Bombardment and High Resolution Mass Spectrometry. *Polyhedron* **1998**, *17*, 193–197.

(96) Hou, Z.; Wakatsuki, Y. Isolation and X-ray Structures of the Hexamethylphosphoramide (Hmpa)-Coordinated Lanthanide(II) Diiodide Complexes [Sml2(Hmpa)4] and [Yb(Hmpa)4(Thf)2]I2. *J. Chem. Soc., Chem. Commun.* **1994**, 1205–1206.

(97) Shabangi, M.; Kuhlman, M. L.; Flowers, R. A. Mechanism of Reduction of Primary Alkyl Radicals by SmI2-HMPA. *Org. Lett.* **1999**, *1*, 2133–2135.

(98) Stevens, A. C.; Brak, K.; Bremner, W. S.; Brown, A. M.; Chtchemelinine, A.; Heumann, L.; Kerschen, J. A.; Subotkowski, W.; Vieira, T.; Wolfe, L. C.; Xu, B.; Yu, C.-Y. Development of a Scalable Lanthanide Halide/Quaternary Ammonium Salt System for the Nucleophilic Addition of Grignard Reagents to Carbonyl Groups and Application to the Synthesis of a Remdesivir Intermediate. *Org. Process Res. Dev.* **2022**, *26*, 754–763.

(99) Sahloul, K.; Sun, L.; Requet, A.; Chahine, Y.; Mellah, M. A Samarium "Soluble" Anode: A New Source of SmI2 Reagent for Electrosynthetic Application. *Chem. – Eur. J.* **2012**, *18*, 11205–11209.

(100) Schwartz, P.-O.; Pejic, M.; Wachtler, M.; Bäuerle, P. Synthesis and Characterization of Electroactive PEDOT-TEMPO Polymers as Potential Cathode Materials in Rechargeable Batteries. *Synthetic Metals* **2018**, *243*, 51–57.

(101) Chen, P.; Fryling, M. A.; McCreery, R. L. Electron Transfer Kinetics at Modified Carbon Electrode Surfaces: The Role of Specific Surface Sites. *Anal. Chem.* **1995**, *67*, 3115–3122.

(102) Maity, S.; Flowers, R. A. Mechanistic Study and Development of Catalytic Reactions of Sm(II). *J. Am. Chem. Soc.* **2019**, *141*, 3207–3216.

(103) Bodizs, G.; Raabe, I.; Scopelliti, R.; Krossing, I.; Helm, L. Synthesis, Structures and Characterisations of Truly Homoleptic Acetonitrile Ln3+ Complexes in Solid State and in Solution. *Dalton Trans.* **2009**, 5137–5147.

(104) Mudring, A.-V.; Tang, S. Ionic Liquids for Lanthanide and Actinide Chemistry. *Eur. J. Inorg. Chem.* **2010**, *2010*, 2569–2581.

(105) Arenz, S.; Babai, A.; Binnemans, K.; Driesen, K.; Giernoth, R.; Mudring, A.-V.; Nockemann, P. Intense Near-Infrared Luminescence of Anhydrous Lanthanide(III) Iodides in an Imidazolium Ionic Liquid. *Chemical Physics Letters* **2005**, *402*, 75–79.

(106) Gonçalves, M. C.; de Zea Bermudez, V.; Sá Ferreira, R. A.; Carlos, L. D.; Ostrovskii, D.; Rocha, J. Optically Functional Di-Urethanesil Nanohybrids Containing Eu3+ Ions. *Chem. Mater.* **2004**, *16*, 2530–2543.

(107) Stasko, D.; Reed, C. A. Optimizing the Least Nucleophilic Anion. A New, Strong Methyl+ Reagent. *J. Am. Chem. Soc.* **2002**, *124*, 1148–1149.

(108) Díaz-Torres, R.; Alvarez, S. Coordinating Ability of Anions and Solvents towards Transition Metals and Lanthanides. *Dalton Trans.* **2011**, *40*, 10742–10750.

(109) Fuchs, J. R.; Mitchell, M. L.; Shabangi, M.; Flowers, R. A. The Effect of Lithium Bromide and Lithium Chloride on the Reactivity of SmI2 in THF. *Tetrahedron Lett.* **1997**, *38*, 8157–8158.

(110) Arashiba, K.; Kanega, R.; Himeda, Y.; Nishibayashi, Y. Catalytic Ammonia Formation with Electrochemically Reduced Samarium Diiodide from Samarium Triiodide and Water from Dinitrogen. *Chem. Lett.* **2021**, *50*, 1356–1358.

(111) Dahlén, A.; Hilmersson, G. Instantaneous SmI2/H2O/Amine-Mediated Reductions in THF. *Chem. – Eur. J.* **2003**, *9*, 1123–1128.

(112) Maity, S.; Hoz, S. Deciphering a 20-Year-Old Conundrum: The Mechanisms of Reduction by the Water/Amine/SmI2 Mixture. *Chem. – Eur. J.* **2015**, *21*, 18394–18400.

(113) Shatskiy, A.; Lundberg, H.; Kärkäs, M. D. Organic Electrosynthesis: Applications in Complex Molecule Synthesis. *ChemElectroChem* **2019**, *6*, 4067–4092.

(114) Claraz, A.; Masson, G. Recent Advances in C(Sp3)–C(Sp3) and C(Sp3)–C(Sp2) Bond Formation through Cathodic Reactions: Reductive and Convergent Paired Electrolyses. *ACS Org. Inorg. Au* **2022**, *2*, 126–147.

(115) Liu, X.-F.; Zhang, K.; Tao, L.; Lu, X.-B.; Zhang, W.-Z. Recent Advances in Electrochemical Carboxylation Reactions Using Carbon Dioxide. *Green Chem. Eng.* **2022**, *3*, 125–137.

(116) Li, Y.; Wen, L.; Guo, W. A Guide to Organic Electroreduction Using Sacrificial Anodes. *Chem. Soc. Rev.* **2023**, *52*, 1168–1188.

(117) Huang, B.; Sun, Z.; Sun, G. Recent Progress in Cathodic Reduction-Enabled Organic Electrosynthesis: Trends, Challenges, and Opportunities. *eScience* **2022**, *2*, 243–277.

(118) *Electrochemistry in Organic Synthesis*, 1st ed.; Ackermann, L., Ed.; Georg Thieme Verlag KG: Stuttgart, 2022, b000000126.

(119) Li, W.; Nonaka, T.; Chou, T.-C. Paired Electrosynthesis of Organic Compounds. *Electrochemistry* **1999**, *67*, 4–10.

(120) Muchez, L.; De Vos, D. E.; Kim, M. Sacrificial Anode-Free Electrosynthesis of α-Hydroxy Acids via Electrocatalytic Coupling of Carbon Dioxide to Aromatic Alcohols. *ACS Sustainable Chem. Eng.* **2019**, *7*, 15860–15864.

(121) Wu, T.; Moeller, K. D. Organic Electrochemistry: Expanding the Scope of Paired Reactions. *Angew. Chem. Int. Ed.* **2021**, *60*, 12883–12890.

(122) Marken, F.; Cresswell, A. J.; Bull, S. D. Recent Advances in Paired Electrosynthesis. *Chem. Rec.* **2021**, *21*, 2585–2600.

(123) Zhang, W.; Guan, W.; Martinez Alvarado, J. I.; Novaes, L. F. T.; Lin, S. Deep Electroreductive Chemistry: Harnessing Carbon- and Silicon-Based Reactive Intermediates in Organic Synthesis. *ACS Catal.* **2023**, *13*, 8038–8048.

(124) Hilt, G. Basic Strategies and Types of Applications in Organic Electrochemistry. *ChemElectroChem* **2020**, *7*, 395–405.

(125) Han, S.-D.; Rajput, N. N.; Qu, X.; Pan, B.; He, M.; Ferrandon, M. S.; Liao, C.; Persson, K. A.; Burrell, A. K. Origin of Electrochemical, Structural, and Transport Properties in Nonaqueous Zinc Electrolytes. *ACS Appl. Mater. Interfaces* **2016**, *8*, 3021–3031.

(126) Commission Regulation (EU) 2021/2030 of 19 November 2021 Amending Annex XVII to Regulation (EC) No 1907/2006 of the European Parliament and of the Council Concerning the Registration, Evaluation, Authorisation and Restriction of Chemicals (REACH) as Regards N,N-dimethylformamide (Text with EEA Relevance), 2021.

(127) Paddon, C. A.; Compton, R. G. A Reference Electrode for Electrochemical and Cryoelectrochemical Use in Tetrahydrofuran Solvent. *Electroanalysis* **2005**, *17*, 1919–1923.

(128) Han, K. S.; Hahn, N. T.; Zavadil, K. R.; Jaegers, N. R.; Chen, Y.; Hu, J. Z.; Murugesan, V.; Mueller, K. T. Factors Influencing Preferential Anion Interactions during Solvation of Multivalent Cations in Ethereal Solvents. *J. Phys. Chem. C* **2021**, *125*, 6005–6012.

(129) Cooper, T. E.; Carl, D. R.; Oomens, J.; Steill, J. D.; Armentrout, P. B. Infrared Spectroscopy of Divalent Zinc and Cadmium Crown Ether Systems. *J. Phys. Chem. A* **2011**, *115*, 5408–5422.

(130) C. Leech, M.; D. Garcia, A.; Petti, A.; P. Dobbs, A.; Lam, K. Organic Electrosynthesis: From Academia to Industry. *React. Chem. Eng.* **2020**, *5*, 977–990.

(131) Meyer, T. H.; Choi, I.; Tian, C.; Ackermann, L. Powering the Future: How Can Electrochemistry Make a Difference in Organic Synthesis? *Chem* **2020**, *6*, 2484–2496.

(132) Zhou, H.-Y.; Tang, H.-T.; He, W.-M. The Future of Organic Electrochemistry Current Transfer. *Chinese J. Catal.* **2023**, *46*, 4–10.

(133) Pletcher, D. Organic Electrosynthesis – A Road to Greater Application. A Mini Review. *Electrochem. Comm.* **2018**, *88*, 1–4.

(134) Pollok, D.; R. Waldvogel, S. Electro-Organic Synthesis – a 21st Century Technique. *Chem. Sci.* **2020**, *11*, 12386–12400.

(135) Wiebe, A.; Gieshoff, T.; Möhle, S.; Rodrigo, E.; Zirbes, M.; Waldvogel, S. R. Electrifying Organic Synthesis. *Angew. Chem. Int. Ed.* **2018**, *57*, 5594–5619.

(136) Zhu, C.; Ang, N. W. J.; Meyer, T. H.; Qiu, Y.; Ackermann, L. Organic Electrochemistry: Molecular Syntheses with Potential. *ACS Cent. Sci.* **2021**, *7*, 415–431.

(137) Rafiee, M.; Mayer, M. N.; Punchihewa, B. T.; Mumau, M. R. Constant Potential and Constant Current Electrolysis: An Introduction and Comparison of Different Techniques for Organic Electrosynthesis. *J. Org. Chem.* **2021**, *86*, 15866–15874.

(138) McKenzie, E. C. R.; Hosseini, S.; Petro, A. G. C.; Rudman, K. K.; Gerroll, B. H. R.; Mubarak, M. S.; Baker, L. A.; Little, R. D. Versatile Tools for Understanding Electrosynthetic Mechanisms. *Chem. Rev.* **2022**, *122*, 3292–3335.

(139) Sandford, C.; A. Edwards, M.; J. Klunder, K.; P. Hickey, D.; Li, M.; Barman, K.; S. Sigman, M.; S. White, H.; D. Minteer, S. A Synthetic Chemist's Guide to Electroanalytical Tools for Studying Reaction Mechanisms. *Chem. Sci.* **2019**, *10*, 6404–6422.

(140) Costentin, C.; Savéant, J.-M. Concepts and Tools for Mechanism and Selectivity Analysis in Synthetic Organic Electrochemistry. *Proc. Natl. Acad. Sci.* **2019**, *116*, 11147–11152.

(141) Silvestri, G.; Gambino, S.; Filardo, G.; Tiitta, M.; Sjostrom, M.; Wold, S.; Berglind, R.; Karlsson, B. Use of Sacrificial Anodes in Synthetic Electrochemistry. Processes Involving Carbon Dioxide. *Acta Chemica Scandinavica* **1991**, *45*, 987–992.

(142) Chaussard, J.; Folest, J.-C.; Nedelec, J.-Y.; Perichon, J.; Sibille, S.; Troupel, M. Use of Sacrificial Anodes in Electrochemical Functionalization of Organic Halides. *Synthesis* **1990**, *1990*, 369–381.

(143) Heard, D. M.; Lennox, A. J. J. Electrode Materials in Modern Organic Electrochemistry. *Angew. Chem. Int. Ed.* **2020**, *59*, 18866–18884.

(144) Izzi, M.; Sportelli, M. C.; Ditaranto, N.; Picca, R. A.; Innocenti, M.; Sabbatini, L.; Cioffi, N. Pros and Cons of Sacrificial Anode Electrolysis for the Preparation of Transition Metal Colloids: A Review. *ChemElectroChem* **2020**, *7*, 386–394.

(145) Rodríguez, A.; García-Vázquez, J. A. The Use of Sacrificial Anodes for the Electrochemical Synthesis of Metallic Complexes. *Coord. Chem. Rev.* **2015**, *303*, 42–85.

(146) Charboneau, D. J.; Hazari, N.; Huang, H.; Uehling, M. R.; Zultanski, S. L. Homogeneous Organic Electron Donors in Nickel-Catalyzed Reductive Transformations. *J. Org. Chem.* **2022**, *87*, 7589–7609.

(147) Burrows, C. J.; Harper, J. B.; Sander, W.; Tantillo, D. J. Solvation Effects in Organic Chemistry. *J. Org. Chem.* **2022**, *87*, 1599–1601.

(148) Couper, A. M.; Pletcher, D.; Walsh, F. C. Electrode Materials for Electrosynthesis. *Chem. Rev.* **1990**, *90*, 837–865.

(149) Aymard, F.; Nédélec, J.-Y.; Périchon, J. An Efficient Inexpensive Electrochemical Preparation of Ruppert's Reagent. *Tetrahedron Letters* **1994**, *35*, 8623–8624.

(150) Franco, D.; Riahi, A.; Hénin, F.; Muzart, J.; Duñach, E. Electrochemical Reduction of a Racemic Allyl β-Keto Ester Catalyzed by Nickel Complexes: Asymmetric Induction. *Eur. J. Org. Chem.* **2002**, *2002*, 2257–2259.

(151) Nedelec, J. Y.; Mouloud, H. A. H.; Folest, J. C.; Perichon, J. Electrochemical Cross-Coupling of Alkyl Halides in the Presence of a Sacrificial Anode. *J. Org. Chem.* **1988**, *53*, 4720–4724.

(152) Koyanagi, T.; Herath, A.; Chong, A.; Ratnikov, M.; Valiere, A.; Chang, J.; Molteni, V.; Loren, J. One-Pot Electrochemical Nickel-Catalyzed Decarboxylative Sp2–Sp3 Cross-Coupling. *Org. Lett.* **2019**, *21*, 816–820.

(153) Beil, S. B.; Pollok, D.; Waldvogel, S. R. Reproducibility in Electroorganic Synthesis—Myths and Misunderstandings. *Angew. Chem. Int. Ed.* **2021**, *60*, 14750–14759.

(154) Klein, M.; Waldvogel, S. R. Counter Electrode Reactions—Important Stumbling Blocks on the Way to a Working Electro-organic Synthesis. *Angew. Chem. Int. Ed.* **2022**, *61*, e202204140.

(155) Leech, M. C.; Lam, K. A Practical Guide to Electrosynthesis. *Nat. Rev. Chem.* **2022**, *6*, 275–286.

(156) Kingston, C.; Palkowitz, M. D.; Takahira, Y.; Vantourout, J. C.; Peters, B. K.; Kawamata, Y.; Baran, P. S. A Survival Guide for the "Electro-curious". *Acc. Chem. Res.* **2020**, *53*, 72–83.

(157) Schotten, C.; P. Nicholls, T.; A. Bourne, R.; Kapur, N.; N. Nguyen, B.; E. Willans, C. Making Electrochemistry Easily Accessible to the Synthetic Chemist. *Green Chem.* **2020**, *22*, 3358–3375.

(158) Elgrishi, N.; Rountree, K. J.; McCarthy, B. D.; Rountree, E. S.; Eisenhart, T. T.; Dempsey, J. L. A Practical Beginner's Guide to Cyclic Voltammetry. *J. Chem. Educ.* **2018**, *95*, 197–206.

(159) Seyferth, D. The Grignard Reagents. *Organometallics* **2009**, *28*, 1598–1605.

(160) In *Hydroboration and Organic Synthesis: 9-Borabicyclo[3.3.1]Nonane (9-BBN)*, Dhillon, R. S., Ed.; Springer: Berlin, Heidelberg, 2007, pp 271–281.

(161) Koon, S. E.; Oyler, C. E.; Hill, J. H. M.; Bowyer, W. J. Visualization of the Areal Distribution of the Reactivity of Magnesium Surfaces in the Formation of Grignard Reagents. *J. Org. Chem.* **1993**, *58*, 3225–3226.

(162) Teerlinck, C. E.; Bowyer, W. J. Reactivity of Magnesium Surfaces during the Formation of Grignard Reagents. *J. Org. Chem.* **1996**, *61*, 1059–1064.

(163) Condon, S.; Zou, C.; Nédélec, J.-Y. Electrochemical Alkyl Transfer Reaction from Trialkylboranes to Polyhalo Compounds. *J. Organomet. Chem.* **2006**, *691*, 3245–3250.

(164) Durandetti, S.; Sibille, S.; Perichon, J. Electrochemical Allylation of Carbonyl Compounds Using Nickel Catalyst and Zinc(II) Species. *J. Org. Chem.* **1989**, *54*, 2198–2204.

(165) Ohno, T.; Sakai, M.; Ishino, Y.; Shibata, T.; Maekawa, H.; Nishiguchi, I. Mg-Promoted Regio- and Stereoselective C-Acylation of Aromatic α,β-Unsaturated Carbonyl Compounds. *Org. Lett.* **2001**, *3*, 3439–3442.

(166) Yamamoto, Y.; Maekawa, H.; Goda, S.; Nishiguchi, I. Novel One-Pot Vicinal Double C-Acylation of Styrenes and Methacrylates by Electroreduction. *Org. Lett.* **2003**, *5*, 2755–2758.

(167) Kita, Y.; Maekawa, H.; Yamasaki, Y.; Nishiguchi, I. Highly Selective and Facile Synthesis of Dihydro- and Tetrahydropyridine Dicarboxylic Acid Derivatives Using Electroreduction as a Key Step1. *Tetrahedron* **2001**, *57*, 2095–2102.

(168) Wu, X.; Gannett, C. N.; Liu, J.; Zeng, R.; Novaes, L. F. T.; Wang, H.; Abruña, H. D.; Lin, S. Intercepting Hydrogen Evolution with Hydrogen-Atom Transfer: Electron-Initiated Hydrofunctionalization of Alkenes. *J. Am. Chem. Soc.* **2022**, *144*, 17783–17791.

(169) Areias, M. C. C.; Bieber, L. W.; Navarro, M.; Diniz, F. B. Metal-Free Electrochemical Reformatsky Reaction in Water: Further Evidence for a Radical Mechanism. *J. Electroanal. Chem.* **2003**, *558*, 125–130.

(170) Saboureau, C.; Troupel, M.; Perichon, J. Organic Electrosynthesis with a Sacrificial Anode. Chemical Reductive Degradation of the Solvent N,N-dimethyl Formamide. *J. Appl. Electrochem.* **1990**, *20*, 97–101.

(171) Walker, B. R.; Sevov, C. S. An Electrochemically Promoted, Nickel-Catalyzed Mizoroki–Heck Reaction. *ACS Catal.* **2019**, *9*, 7197–7203.

(172) Lai, Y.-L.; Huang, J.-M. Palladium-Catalyzed Electrochemical Allylic Alkylation between Alkyl and Allylic Halides in Aqueous Solution. *Org. Lett.* **2017**, *19*, 2022–2025.

(173) Peters, B. K. et al. Scalable and Safe Synthetic Organic Electroreduction Inspired by Li-ion Battery Chemistry. *Science* **2019**, *363*, 838–845.

(174) Sun, L.; Mellah, M. Efficient Electrosynthesis of SmCl2, SmBr2, and Sm(OTf)2 from a "Sacrificial" Samarium Anode: Effect of nBu4NPF6 on the Reactivity. *Organometallics* **2014**, *33*, 4625–4628.

(175) Sun, L.; Sahloul, K.; Mellah, M. Use of Electrochemistry to Provide Efficient SmI2 Catalytic System for Coupling Reactions. *ACS Catal.* **2013**, *3*, 2568–2573.

(176) Lu, L.; Siu, J. C.; Lai, Y.; Lin, S. An Electroreductive Approach to Radical Silylation via the Activation of Strong Si–Cl Bond. *J. Am. Chem. Soc.* **2020**, *142*, 21272–21278.

(177) Manabe, S.; Wong, C. M.; Sevov, C. S. Direct and Scalable Electroreduction of Triphenylphosphine Oxide to Triphenylphosphine. *J. Am. Chem. Soc.* **2020**, *142*, 3024–3031.

(178) Silvestri, G.; Gambino, S.; Filardo, G.; Greco, G.; Gulotta, A. Electrochemical Carboxylation of Benzal Chloride. *Tetrahedron Lett.* **1984**, *25*, 4307–4308.

(179) Matthessen, R.; Fransaer, J.; Binnemans, K.; Vos, D. E. D. Electrocarboxylation: Towards Sustainable and Efficient Synthesis of Valuable Carboxylic Acids. *Beilstein J. Org. Chem.* **2014**, *10*, 2484–2500.

(180) Wang, M.; Zhang, C.; Ci, C.; Jiang, H.; Dixneuf, P. H.; Zhang, M. Room Temperature Construction of Vicinal Amino Alcohols via Electroreductive Cross-Coupling of N-Heteroarenes and Carbonyls. *J. Am. Chem. Soc.* **2023**, *145*, 10967–10973.

(181) Hilt, G.; Smolko, K. I. Electrochemical Regeneration of Low-Valent Indium(I) Species as Catalysts for C-C Bond Formations. *Angew. Chem. Int. Ed.* **2001**, *40*, 3399–3402.

(182) Ang, N. W. J.; Ackermann, L. Electroreductive Nickel-Catalyzed Thiolation: Efficient Cross-Electrophile Coupling for C-S Formation. *Chem. – Eur. J.* **2021**, *27*, 4883–4887.

(183) Leisegang, T.; Meutzner, F.; Zschornak, M.; Münchgesang, W.; Schmid, R.; Nestler, T.; Eremin, R. A.; Kabanov, A. A.; Blatov, V. A.; Meyer, D. C. The Aluminum-Ion Battery: A Sustainable and Seminal Concept? *Front. Chem.* **2019**, *7*.

(184) Kim, S. S.; See, K. A. Activating Magnesium Electrolytes through Chemical Generation of Free Chloride and Removal of Trace Water. *ACS Appl. Mater. Interfaces* **2021**, *13*, 671–680.

(185) Ghijsen, J.; Namba, H.; Thiry, P. A.; Pireaux, J. J.; Caudano, P. Adsorption of Oxygen on the Magnesium (0001) Surface Studied by XPS. *Appl. Surf. Sci.* **1981**, *8*, 397–411.

(186) Thiry, P. A.; Ghijsen, J.; Sporken, R.; Pireaux, J. J.; Johnson, R. L.; Caudano, R. Incipient Oxidation of Magnesium: A High-Resolution Electron-Energy-Loss and Photoemission Study. *Phys. Rev. B* **1989**, *39*, 3620–3631.

(187) He, S.; Luo, J.; Leo Liu, T. MgCl 2 /AlCl 3 Electrolytes for Reversible Mg Deposition/Stripping: Electrochemical Conditioning or Not? *J. Mater. Chem. A* **2017**, *5*, 12718–12722.

(188) Shterenberg, I.; Salama, M.; Yoo, H. D.; Gofer, Y.; Park, J.-B.; Sun, Y.-K.; Aurbach, D. Evaluation of (CF3SO2)2N- (TFSI) Based Electrolyte Solutions for Mg Batteries. *J. Electrochem. Soc.* **2015**, *162*, A7118.

(189) Iton, Z. W. B.; See, K. A. Multivalent Ion Conduction in Inorganic Solids. *Chem. Mater.* **2022**, *34*, 881–898.

(190) Ellingham, H. J. T. Reducibility of Oxides and Sulphides in Metallurgical Processes. *J. Soc. Chem. Ind.* **1944**, *63*, 125–160.

(191) Connell, J. G.; Genorio, B.; Lopes, P. P.; Strmcnik, D.; Stamenkovic, V. R.; Markovic, N. M. Tuning the Reversibility of Mg Anodes via Controlled Surface Passivation by H2O/Cl– in Organic Electrolytes. *Chem. Mater.* **2016**, *28*, 8268–8277.

(192) Nordlien, J. H.; Ono, S.; Masuko, N.; Nisancioglu, K. A TEM Investigation of Naturally Formed Oxide Films on Pure Magnesium. *Corros. Sci.* **1997**, *39*, 1397–1414.

(193) DeLano, T. J.; Reisman, S. E. Enantioselective Electroreductive Coupling of Alkenyl and Benzyl Halides via Nickel Catalysis. *ACS Catal.* **2019**, *9*, 6751–6754.

(194) Shterenberg, I.; Salama, M.; Gofer, Y.; Aurbach, D. Hexafluorophosphate-Based Solutions for Mg Batteries and the Importance of Chlorides. *Langmuir* **2017**, *33*, 9472–9478.

(195) Harwood, S. J.; Palkowitz, M. D.; Gannett, C. N.; Perez, P.; Yao, Z.; Sun, L.; Abruña, H. D.; Anderson, S. L.; Baran, P. S. Modular Terpene Synthesis Enabled by Mild Electrochemical Couplings. *Science* **2022**, *375*, 745–752.

(196) Lu, Z.; Schechter, A.; Moshkovich, M.; Aurbach, D. On the Electrochemical Behavior of Magnesium Electrodes in Polar Aprotic Electrolyte Solutions. *J. Electroanal. Chem.* **1999**, *466*, 203–217.

(197) Shuai, H.; Xu, J.; Huang, K. Progress in Retrospect of Electrolytes for Secondary Magnesium Batteries. *Coord. Chem. Rev.* **2020**, *422*, 213478.

(198) Yoo, H. D.; Han, S.-D.; Bolotin, I. L.; Nolis, G. M.; Bayliss, R. D.; Burrell, A. K.; Vaughey, J. T.; Cabana, J. Degradation Mechanisms of Magnesium Metal Anodes in Electrolytes Based on (CF3SO2)2N– at High Current Densities. *Langmuir* **2017**, *33*, 9398–9406.

(199) Zhang, W.; Guan, W.; Wang, Y.; Lin, S.; See, K. A. Enabling Al Sacrificial Anodes in Tetrahydrofuran Electrolytes for Reductive Electrosynthesis. *Chem. Sci.* **2023**, *14*, 13108–13118.

(200) Dugas, R.; Forero-Saboya, J. D.; Ponrouch, A. Methods and Protocols for Reliable Electrochemical Testing in Post-Li Batteries (Na, K, Mg, and Ca). *Chem. Mater.* **2019**, *31*, 8613–8628.

(201) Schuett, F. M.; Zeller, S. J.; Eckl, M. J.; Matzik, F. M.; Heubach, M.-K.; Geng, T.; Hermann, J. M.; Uhl, M.; Kibler, L. A.; Engstfeld, A. K.; Jacob, T. Versatile 3D-Printed Micro-Reference Electrodes for Aqueous and Non-Aqueous Solutions. *Angew. Chem.* **2021**, *133*, 22965–22972.

(202) Ciobanu, M.; Wilburn, J. P.; Lowy, D. A. Miniaturized Reference Electrodes. II. Use in Corrosive, Biological, and Organic Media. *Electroanalysis* **2004**, *16*, 1351–1358.

(203) Wang, S.; Zhang, J.; Gharbi, O.; Vivier, V.; Gao, M.; Orazem, M. E. Electrochemical Impedance Spectroscopy. *Nat. Rev. Methods Primers* **2021**, *1*, 1–21.

(204) Zhang, W.; Gu, C.; Wang, Y.; Ware, S. D.; Lu, L.; Lin, S.; Qi, Y.; See, K. A. Improving the Mg Sacrificial Anode in Tetrahydrofuran for Synthetic Electrochemistry by Tailoring Electrolyte Composition. *JACS Au* **2023**, *3*, 2280–2290.

(205) Zhang, W.; Lu, L.; Zhang, W.; Wang, Y.; Ware, S. D.; Mondragon, J.; Rein, J.; Strotman, N.; Lehnherr, D.; See, K. A.; Lin, S. Electrochemically Driven Cross-Electrophile Coupling of Alkyl Halides. *Nature* **2022**, *604*, 292–297.

(206) McCafferty, E. Sequence of Steps in the Pitting of Aluminum by Chloride Ions. *Corros. Sci.* **2003**, *45*, 1421–1438.

(207) Levy, N. R.; Auinat, M.; Ein-Eli, Y. Tetra-Butyl Ammonium Fluoride – An Advanced Activator of Aluminum Surfaces in Organic Electrolytes for Aluminum-Air Batteries. *Energy Storage Mater.* **2018**, *15*, 465–474.

(208) Rehim, S. S. A.; Hassan, H. H.; Amin, M. A. Corrosion and Corrosion Inhibition of Al and Some Alloys in Sulphate Solutions Containing Halide Ions Investigated by an Impedance Technique. *Appl. Surf. Sci.* **2002**, *187*, 279–290.

(209) Mazhar, A. A.; Badawy, W. A.; Abou-Romia, M. M. Impedance Studies of Corrosion Resistance of Aluminium in Chloride Media. *Surf. Coat. Tech.* **1986**, *29*, 335–345.

(210) Li, W.; Cochell, T.; Manthiram, A. Activation of Aluminum as an Effective Reducing Agent by Pitting Corrosion for Wet-chemical Synthesis. *Sci. Rep.* **2013**, *3*, 1229.

(211) Natishan, P. M.; O'Grady, W. E. Chloride Ion Interactions with Oxide-Covered Aluminum Leading to Pitting Corrosion: A Review. *J. Electrochem. Soc.* **2014**, *161*, C421.

(212) Li, X.; Gao, T.; Han, F.; Ma, Z.; Fan, X.; Hou, S.; Eidson, N.; Li, W.; Wang, C. Reducing Mg Anode Overpotential via Ion Conductive Surface Layer Formation by Iodine Additive. *Adv. Energy Mater.* **2018**, *8*, 1701728.

(213) Chae, M. S.; Heo, J. W.; Kwak, H. H.; Lee, H.; Hong, S.-T. Organic Electrolyte-Based Rechargeable Zinc-Ion Batteries Using Potassium Nickel Hexacyanoferrate as a Cathode Material. *J. Power Sources* **2017**, *337*, 204–211.

(214) Cheng, Y.; Luo, L.; Zhong, L.; Chen, J.; Li, B.; Wang, W.; Mao, S. X.; Wang, C.; Sprenkle, V. L.; Li, G.; Liu, J. Highly Reversible Zinc-Ion Intercalation into Chevrel Phase Mo6S8 Nanocubes and Applications for Advanced Zinc-Ion Batteries. *ACS Appl. Mater. Interfaces* **2016**, *8*, 13673–13677.

(215) Shoesmith, D. W.; Sunder, S.; Bailey, M. G.; Wallace, G. J.; Stanchell, F. W. Anodic Oxidation of Copper in Alkaline Solutions: Part IV. Nature of the Passivating Film. *J. Electroanal. Chem. Interf. Electrochem.* **1983**, *143*, 153–165.

(216) Vorauer, T.; Schöggl, J.; Sanadhya, S. G.; Poluektov, M.; Widanage, W. D.; Figiel, L.; Schädler, S.; Tordoff, B.; Fuchsbichler, B.; Koller, S.; Brunner, R. Impact of Solid-Electrolyte Interphase Reformation on Capacity Loss in Silicon-Based Lithium-Ion Batteries. *Commun. Mater.* **2023**, *4*, 1–12.

(217) Lu, L.; Wang, Y.; Zhang, W.; Zhang, W.; See, K. A.; Lin, S. Three-Component Cross-Electrophile Coupling: Regioselective Electrochemical Dialkylation of Alkenes. *J. Am. Chem. Soc.* **2023**, *145*, 22298–22304.

(218) Huang, C.; Ma, W.; Zheng, X.; Xu, M.; Qi, X.; Lu, Q. Epoxide Electroreduction. *J. Am. Chem. Soc.* **2022**, *144*, 1389–1395.

(219) Perkins, R. J.; Pedro, D. J.; Hansen, E. C. Electrochemical Nickel Catalysis for Sp2-Sp3 Cross-Electrophile Coupling Reactions of Unactivated Alkyl Halides. *Org. Lett.* **2017**, *19*, 3755–3758.

(220) Zhang, H.; Qiao, L.; Kühnle, H.; Figgemeier, E.; Armand, M.; Gebresilassie Eshetu, G. From Lithium to Emerging Mono- and Multivalent-Cation-Based Rechargeable Batteries: Non-Aqueous Organic Electrolyte and Interphase Perspectives. *Energy Environ. Sci.* **2023**, *16*, 11–52.

(221) Liu, X.; Du, A.; Guo, Z.; Wang, C.; Zhou, X.; Zhao, J.; Sun, F.; Dong, S.; Cui, G. Uneven Stripping Behavior, an Unheeded Killer of Mg Anodes. *Adv. Mater.* **2022**, *34*, 2201886.

(222) He, P.; Huang, J. Detrimental Effects of Surface Imperfections and Unpolished Edges on the Cycling Stability of a Zinc Foil Anode. *ACS Energy Lett.* **2021**, *6*, 1990–1995.

(223) Zeng, Q.; Xu, S. Thermodynamics and Characteristics of Heterogeneous Nucleation on Fractal Surfaces. *J. Phys. Chem. C* **2015**, *119*, 27426–27433.

(224) Shao, Y.; Liu, T.; Li, G.; Gu, M.; Nie, Z.; Engelhard, M.; Xiao, J.; Lv, D.; Wang, C.; Zhang, J.-G.; Liu, J. Coordination Chemistry in Magnesium Battery Electrolytes: How Ligands Affect Their Performance. *Sci. Rep.* **2013**, *3*, 3130.

(225) Okoshi, M.; Yamada, Y.; Yamada, A.; Nakai, H. Theoretical Analysis on De-Solvation of Lithium, Sodium, and Magnesium Cations to Organic Electrolyte Solvents. *J. Electrochem. Soc.* **2013**, *160*, A2160.

(226) Lou, T. S.-B.; Kawamata, Y.; Ewing, T.; Correa-Otero, G. A.; Collins, M. R.; Baran, P. S. Scalable, Chemoselective Nickel Electrocatalytic Sulfinylation of Aryl Halides with SO2. *Angew. Chem. Int. Ed.* **2022**, *61*, e202208080.

(227) Li, R.; Li, Y.; Zhang, R.; He, M.; Ma, Y.; Huo, H.; Zuo, P.; Yin, G. Voltage Hysteresis of Magnesium Anode: Taking Magnesium-Sulfur Battery as an Example. *Electrochim. Acta* **2021**, *369*, 137685.

(228) Kim, H.; Kim, H.; Lambert, T. H.; Lin, S. Reductive Electrophotocatalysis: Merging Electricity and Light To Achieve Extreme Reduction Potentials. *J. Am. Chem. Soc.* **2020**, *142*, 2087–2092.

(229) Yuan, G.-Q.; Jiang, H.-F.; Lin, C.; Liao, S.-J. Efficient Electrochemical Synthesis of 2-Arylsuccinic Acids from CO2 and Aryl-Substituted Alkenes with Nickel as the Cathode. *Electrochim. Acta* **2008**, *53*, 2170–2176.

(230) Zhang, W.; Lin, S. Electroreductive Carbofunctionalization of Alkenes with Alkyl Bromides via a Radical-Polar Crossover Mechanism. *J. Am. Chem. Soc.* **2020**, *142*, 20661–20670.

(231) Déjardin, C.; Renou, A.; Maddaluno, J.; Durandetti, M. Nickel-Catalyzed Electrochemical Cyclization of Alkynyl Aryl Iodide and the Domino Reaction with Aldehydes. *J. Org. Chem.* **2021**, *86*, 8882–8890.

(232) Durandetti, M.; Meignein, C.; Périchon, J. Iron-Mediated Electrochemical Reaction of α-Chloroesters with Carbonyl Compounds. *Org. Lett.* **2003**, *5*, 317–320.

(233) Ishifune, M.; Yamashita, H.; Kera, Y.; Yamashita, N.; Hirata, K.; Murase, H.; Kashimura, S. Electroreduction of Aromatics Using Magnesium Electrodes in Aprotic Solvents Containing Alcoholic Proton Donors. *Electrochim. Acta* **2003**, *48*, 2405–2409.

(234) Huang, J.-M.; Dong, Y. Zn-Mediated Electrochemical Allylation of Aldehydes in Aqueous Ammonia. *Chem. Commun.* **2009**, *0*, 3943–3945.

(235) Huang, J.-M.; Lin, Z.-Q.; Chen, D.-S. Electrochemically Supported Deoxygenation of Epoxides into Alkenes in Aqueous Solution. *Org. Lett.* **2012**, *14*, 22–25.

(236) Huang, J.-M.; Wang, X.-X.; Dong, Y. Electrochemical Allylation Reactions of Simple Imines in Aqueous Solution Mediated by Nanoscale Zinc Architectures. *Angew. Chem. Int. Ed.* **2011**, *50*, 924–927.

(237) Gosmini, C.; Lasry, S.; Nedelec, J.-Y.; Perichon, J. Electrochemical Cross-Coupling between 2-Halopyridines and Aryl or Heteroaryl Halides Catalysed by Nickel-2,2′-Bipyridine Complexes. *Tetrahedron* **1998**, *54*, 1289–1298.

(238) Senboku, H.; Sakai, K.; Fukui, A.; Sato, Y.; Yamauchi, Y. Efficient Synthesis of Mandel Acetates by Electrochemical Carboxylation of Benzal Diacetates. *ChemElectroChem* **2019**, *6*, 4158–4164.

(239) Dörr, M.; Hielscher, M. M.; Proppe, J.; Waldvogel, S. R. Electrosynthetic Screening and Modern Optimization Strategies for Electrosynthesis of Highly Value-added Products. *ChemElectroChem* **2021**, *8*, 2621–2629.

(240) Kang, D.; Xiao, M.; Lemmon, J. P. Artificial Solid-Electrolyte Interphase for Lithium Metal Batteries. *Batter. Supercaps* **2021**, *4*, 445–455.

(241) Gao, S.; Sun, F.; Liu, N.; Yang, H.; Cao, P.-F. Ionic Conductive Polymers as Artificial Solid Electrolyte Interphase Films in Li Metal Batteries – A Review. *Mater. Today* **2020**, *40*, 140–159.

(242) Liu, W.; Liu, P.; Mitlin, D. Review of Emerging Concepts in SEI Analysis and Artificial SEI Membranes for Lithium, Sodium, and Potassium Metal Battery Anodes. *Adv. Energy Mater.* **2020**, *10*, 2002297.

Appendix A

SUPPLEMENTARY INFORMATION FOR FLUORIDE IN THE SEI STABILIZES THE LI METAL INTERFACE IN LI-S BATTERIES WITH SOLVATE ELECTROLYTES

Appendix A contains supplementary information for Chapter 2: Fluoride in the SEI Stabilizes the Li Metal Interface in Li-S Batteries with Solvate Electrolytes. Included in the appendix are fits to EIS and Raman data, C 1s XPS data for all conditions analyzed in the chapter, tabulated XPS peak locations and assignments for all XPS spectra reported in the chapter, ^{1}H-NMR spectra of the solvate electrolytes after reaction with Li metal, and capacity fade data for Li-S cells employing AlF_3-coated Li as the anode.

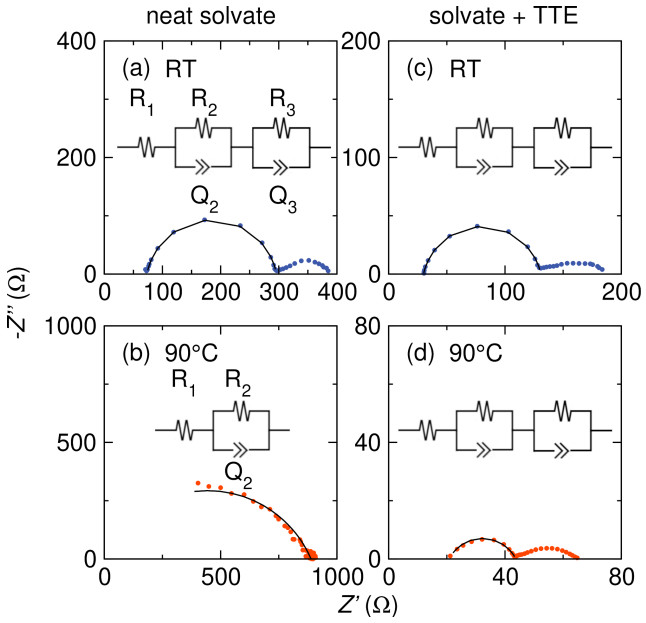

Figure A.1: Fits to the high frequency feature of the final collected EIS spectra of Li-Li symmetric cells prepared with (a) neat solvate electrolyte at room temperature, (b) neat solvate electrolyte at 90 °C, (c) solvate + TTE electrolyte at room temperature, and (d) solvate + TTE electrolyte at 90 °C. EIS data was collected from 10^{6}-10^{-6} Hz (a,c,d) or 10^{6}-1 Hz (b) at 10 points per decade, with a 10 mV amplitude, continuously for 47 h.

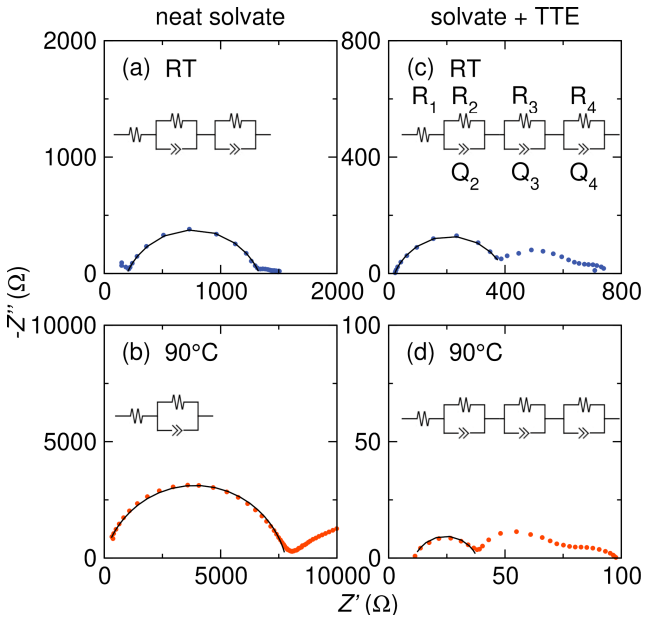

Figure A.2: Fits to the high frequency feature of the final collected EIS spectra of AlF_3-coated Li symmetric cells prepared with (a) neat solvate electrolyte at room temperature, (b) neat solvate electrolyte at 90 °C, (c) solvate + TTE electrolyte at room temperature, and (d) solvate + TTE electrolyte at 90 °C. EIS data was collected from 10^6-10^{-6} Hz (a,c,d) or 10^6-1 Hz (b) at 10 points per decade, with a 10 mV amplitude, continuously for 47 h.

Figure	**Peak binding energy (eV)**	**Assignment**
4a	532.5	SO_4
	533.7	Li_2O
4b	400.1	adsorbed MeCN
4c	685.7	LiF
	689.4	TFSI
4d	531.5	Li_2CO_3
	532.5	SO_4
4e	399.4	CN group
4f	685.7	LiF
	689.4	TFSI

Table A.1: Peak assignments of the X-ray photoelectron spectra of Li metal reacted with the neat solvate electrolyte at RT and 90 °C

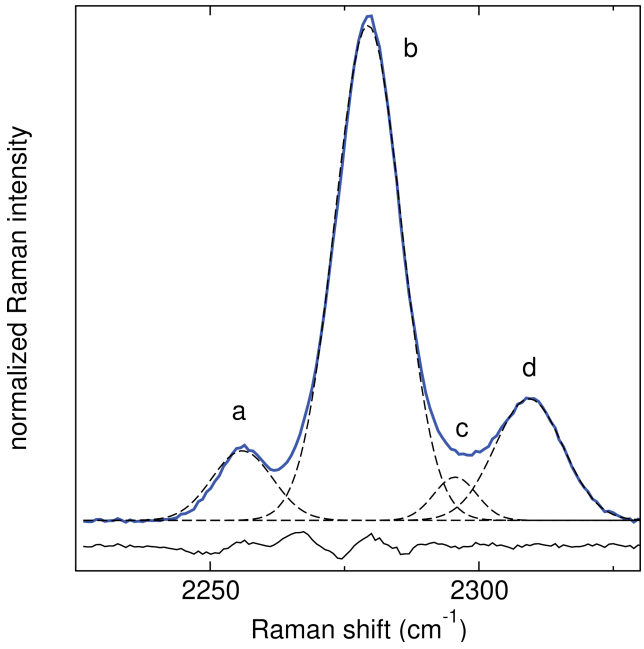

Figure A.3: Fits to the room temperature Raman spectrum of MeCN modes in the neat solvate electrolyte.

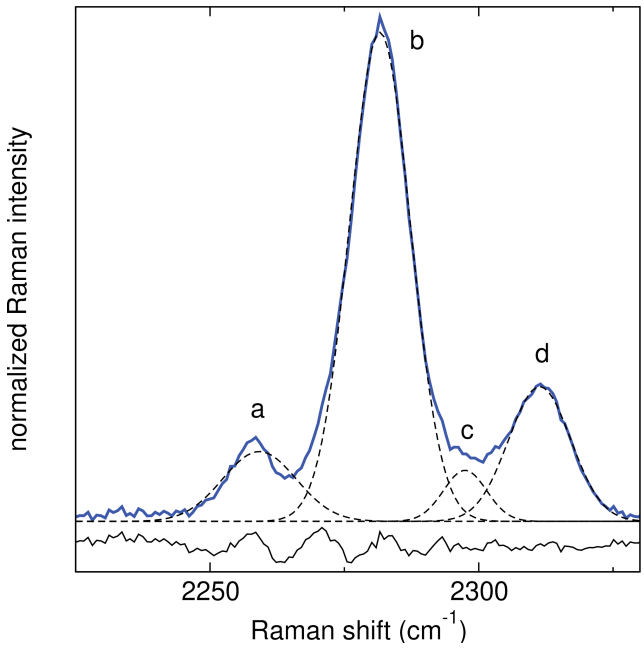

Figure A.4: Fits to the room temperature Raman spectrum of MeCN modes in the solvate + TTE electrolyte.

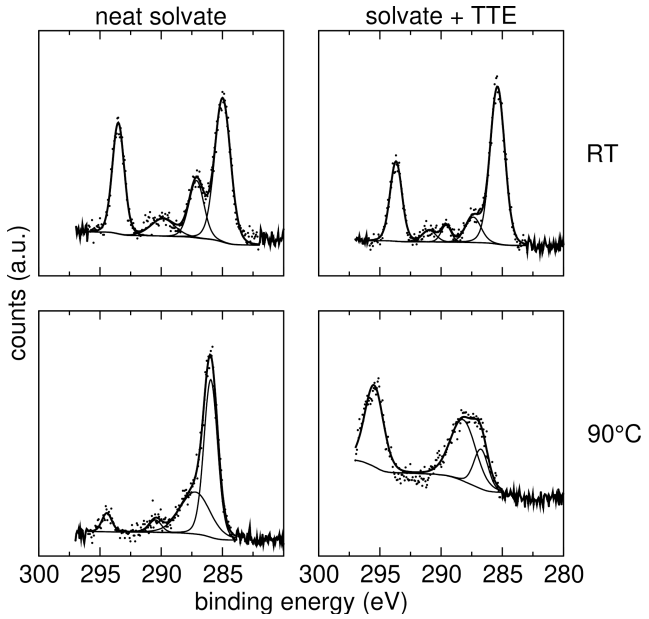

Figure A.5: The C 1s spectra of Li metal with reacted with (a) neat solvate electrolyte at RT, (b) solvate + TTE electrolyte at RT, (c) neat solvate electrolyte at 90 °C, and (d) solvate + TTE electrolyte at 90 °C. The lowest binding energy peak in each spectrum was calibrated to 285 eV.

Figure	**Peak binding energy (eV)**	**Assignment**
5a	532.2	Li_2SO_4
	533.4	Li_2O
	534.6	impurity
5b	400	adsorbed MeCN
5c	685.4	LiF
	689.1	TTE or TFSI
5d	533.1	SO_4
	531.5	Li_2CO_3
5e	399.9	CN group
5f	685.6	LiF
	686.9	TTE or TFSI
	688.9	TFSI
	690.4	TTE

Table A.2: Peak assignments of the X-ray photoelectron spectra of Li metal reacted with the solvate + TTE electrolyte at RT and 90 °C

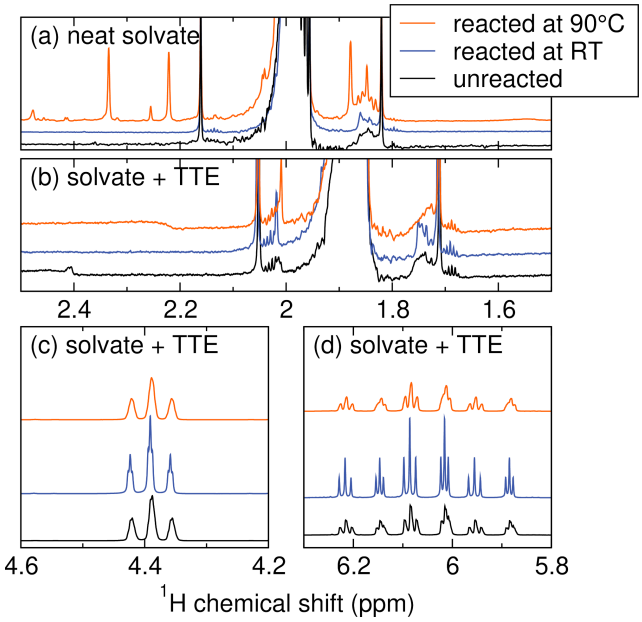

Figure A.6: ^{1}H-NMR spectra of (a) the neat solvate electrolyte and (b)-(d) the solvate + TTE electrolyte before and after reaction with Li metal at room temperature and 90 °C. New peaks appear after reaction between the neat solvate electrolyte and Li at 90 °C, indicating electrolyte decomposition. No decomposition is observed after reaction between the solvate + TTE electrolyte at either temperature. The minor shifts in (b) at 1.75 ppm and 2.01 ppm are likely related to negligible changes in coordination structure after heating rather than electrolyte decomposition. The excess deuterated MeCN added as a lock may also affect electrolyte speciation but does not contribute to decomposition.

Figure	**Peak binding energy (eV)**	**Assignment**
11a	532.3	Li_2SO_4
	533.6	Li_2O
11b	400.1	adsorbed MeCN
11c	689.2	TFSI
	685.4	LiF
11d	531.4	Li_2CO_3
	532.3	Li_2SO_4
	533.6	Li_2O
11e	399.4	CN group
11f	689.2	TFSI
	685.4	LiF

Table A.3: Peak assignments of the X-ray photoelectron spectra of AlF_3-coated Li metal reacted with the neat solvate electrolyte at RT and 90 °C

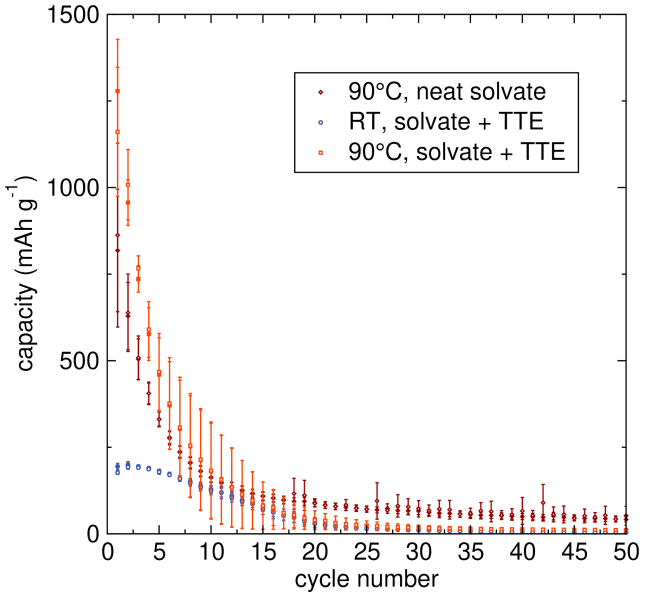

Figure A.7: Capacity fade over 50 cycles in AlF_3-coated Li-S cells prepared with both the neat solvate electrolyte and the solvate + TTE electrolyte. Cells cycled at high temperatures yield higher initial capacity but more rapid capacity fade than cells cycled at room temperature. All cells were cycled at C/10 rate.

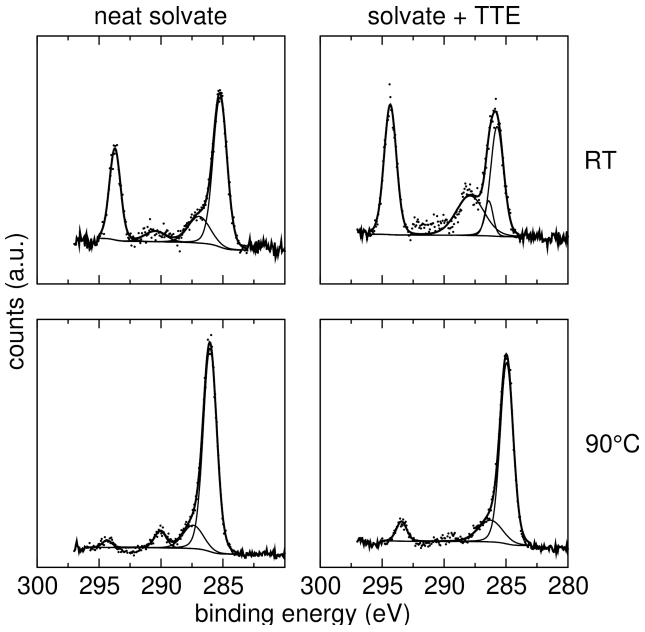

Figure A.8: The C 1s spectra of AlF_3-coated Li metal with reacted with (a) neat solvate electrolyte at RT, (b) solvate + TTE electrolyte at RT, (c) neat solvate electrolyte at 90 °C, and (d) solvate + TTE electrolyte at 90 °C. The lowest binding energy peak in each spectrum was calibrated to 285 eV.

Figure	Peak binding energy (eV)	Assignment
12a	532.5	SO_4
	533.6	Li_2O
	534.6	impurity
12b	400.1	adsorbed MeCN
12c	689.2	TFSI
	685.4	LiF
	685.9	LiF
12d	532.5	SO_4
	533.7	Li_2O
12e	400.1	adsorbed MeCN
12f	689.2	TFSI
	685.4	LiF

Table A.4: Peak assignments of the X-ray photoelectron spectra of AlF_3-coated Li metal reacted with the solvate + TTE electrolyte at RT and 90 °C

Appendix B

SUPPLEMENTARY INFORMATION FOR ELECTROCHEMICAL PREPARATION OF SM(II) REAGENT FACILITATED BY WEAKLY COORDINATING ANIONS

Appendix B contains supplementary information for Chapter 3: Electrochemical Preparation of Sm(II) Reagent Facilitated by Weakly Coordinating Anions. Included in the appendix are background CVs for each supporting electrolyte studied, CVs of Sm salts in various supporting electrolytes, peak current densities and peak splitting for all CVs reported in Chapter 3, and ^{1}H-NMR data for all reported compounds.

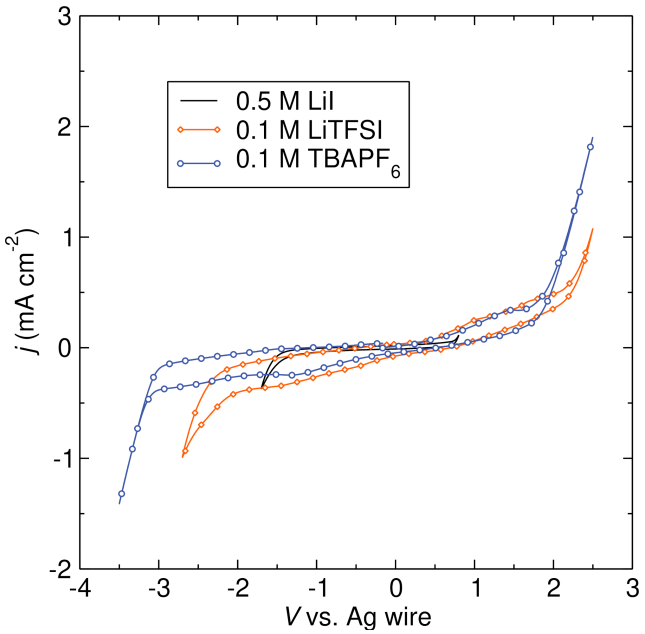

Figure B.1: Background CVs collected at 100 mV/s with 0.5 M LiI, 0.1 M LiTFSI, and 0.1 M $TBAPF_6$ supporting electrolytes.

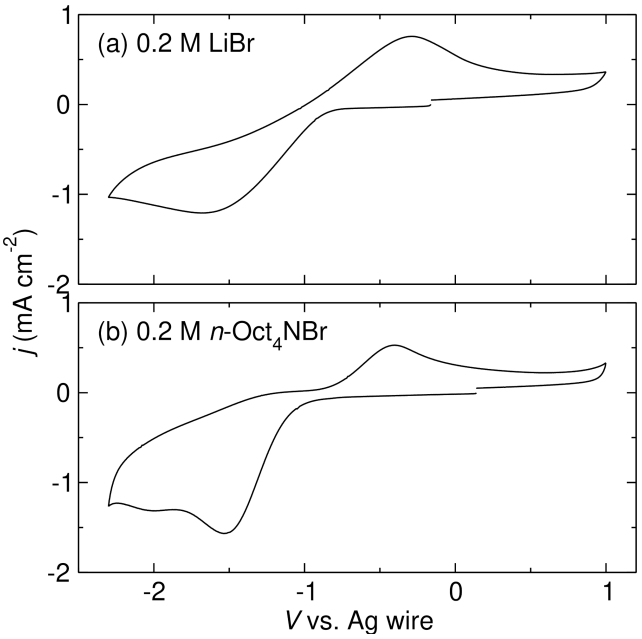

Figure B.2: CVs of 10 mM $Sm(OTf)_3$ with (a) 0.2 M LiBr supporting electrolyte and (b) 0.2 M tetraoctylammonium bromide supporting electrolyte. $Sm(OTf)_3$ undergoes anion exchange with both species to form $SmBr_3$ *in situ*. Both CVs exhibit large peak splittings and $i_{p,c} > i_{p,a}$, indicating electrochemically irreversible reactions.

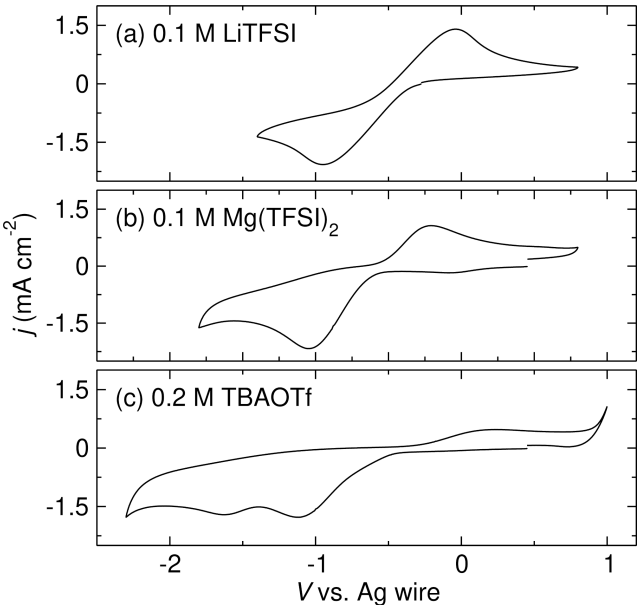

Figure B.3: CVs of 10 mM $Sm(OTf)_3$ + 33 mM LiI with (a) 0.1 M LiTFSI, (b) 0.1 M $Mg(TFSI)_2$, and (c) 0.2 M TBAOTf supporting electrolyte. $Sm(OTf)_3$ undergoes anion exchange with LiI to form SmI_3 *in situ*. While LiTFSI and $Mg(TFSI)_2$ supporting electrolytes permit SmI_3 redox comparable to that with LiI supporting electrolyte, multiple irreversible reductive features are observed with TBAOTf supporting electrolyte. The additional reductive wave at -1.6 V vs. Ag wire may be related to the I^-/I_3^- redox couple.

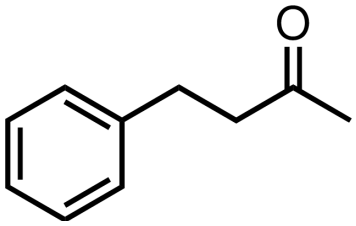

Figure B.4: Structure of benzylacetone. Reported ^{1}H-NMR: (500 MHz, $CDCl_3$) δ 7.32-7.16 (m, 5H), 2.76 (m, 4H), 2.15 (s, 3H).[47]

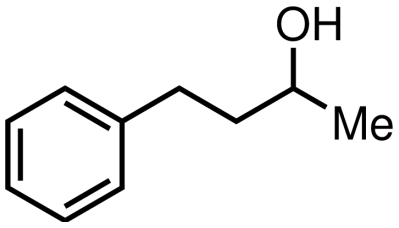

Figure B.5: Structure of 4-phenyl-2-butanol (**1**). Reported ^{1}H-NMR: (500 MHz, $CDCl_3$) δ 7.32-7.18 (m, 5H), 3.87-3.78 (m, 1H), 2.84-2.63 (m, 2H), 1.85-1.72 (m, 2H), 1.23 (d, J = 7.2 Hz, 3H).[48]

Sm source	Supporting electrolyte	$j_{p,a}$ (mA cm^{-2})	$j_{p,c}$ (mA cm^{-2})	ΔE_p (V)
10 mM SmI_2	0.5 M LiI	0.96	0.75	0.80
5 mM SmI_2	0.5 M LiI	0.61	0.54	0.52
2 mM SmI_2	0.5 M LiI	0.26	0.26	0.31
1 mM SmI_2	0.5 M LiI	0.13	0.15	0.20
10 mM SmI_2	0.5 M LiTFSI	1.02	0.98	0.25
5 mM SmI_2	0.5 M LiTFSI	0.44	0.44	0.20
2 mM SmI_2	0.5 M LiTFSI	0.11	0.12	0.16
1 mM SmI_2	0.5 M LiTFSI	0.02	--	--
10 mM SmI_2	0.5 M $TBAPF_6$	0.55	0.84	0.39
5 mM SmI_2	0.5 M $TBAPF_6$	0.12	--	--
2 mM SmI_2	0.5 M $TBAPF_6$	0.08	--	--
1 mM SmI_2	0.5 M $TBAPF_6$	0.03	--	--
5 mM SmI_2	0.5 M LiCl	--	--	--
5 mM SmI_2	0.25 M LiI + 0.25 M LiCl	0.05	0.10	0.86
5 mM SmI_2	0.45 M LiI + 0.05 M LiCl	0.05	0.02	0.56
10 mM $SmCl_3$	0.5 M LiTFSI	0.28	0.59	0.39
10 mM $Sm(OTf)_3$	0.5 M LiTFSI	0.11	0.36	1.12
10 mM $SmBr_3$	0.5 M LiTFSI	0.65	0.89	0.40
10 mM SmI_3	0.5 M LiI	0.94	0.97	0.58

Table B.1: Peak current densities and peak splitting at scan rates of 100 mV s^{-1} for all CVs reported in Chapter 3.

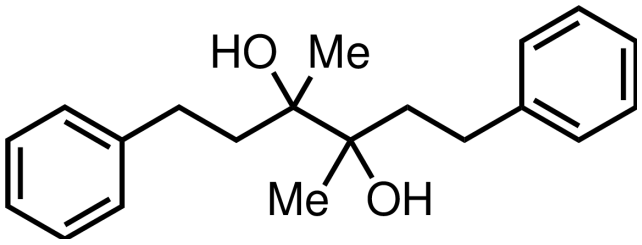

Figure B.6: Structure of the pinacol product (**2**). Reported ^{1}H-NMR: (500 MHz, $CDCl_3$) δ 7.30-7.16 (m, 10H), 3.85 (m, 2H), 2.61-1.78 (m, 8H), 1.28-1.25 (d, J = 6 Hz, 3H, CH_3 diast.).[49]

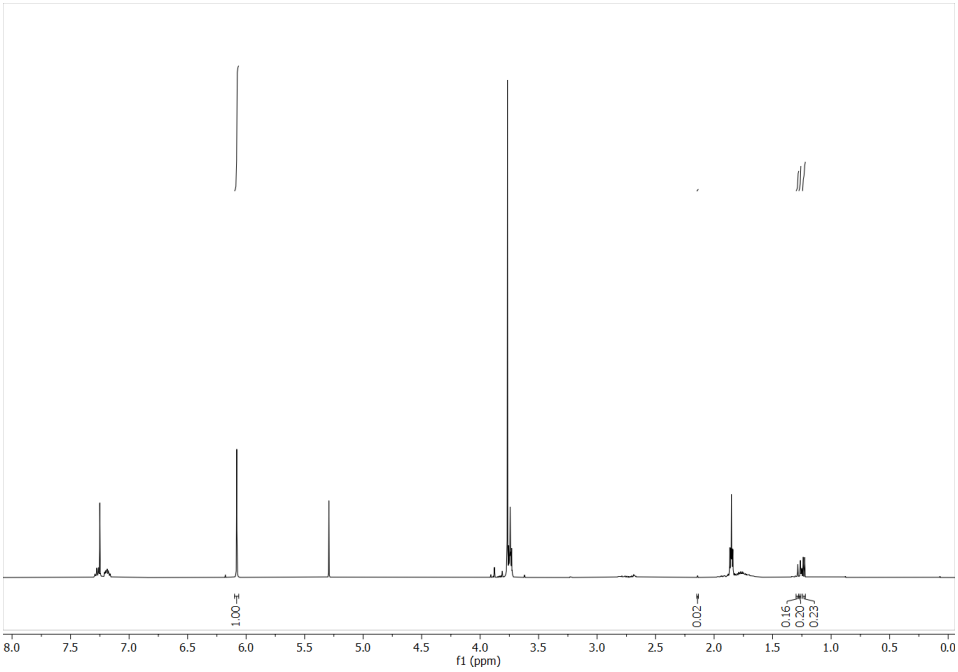

Figure B.7: ^{1}H-NMR of the crude mixture of benzylacetone reduction by commercial SmI_2. Spectrum was referenced to 1,3,5-trimethoxybenzene (8.9 mg, 6.08 ppm, s, 3H) as internal standard.

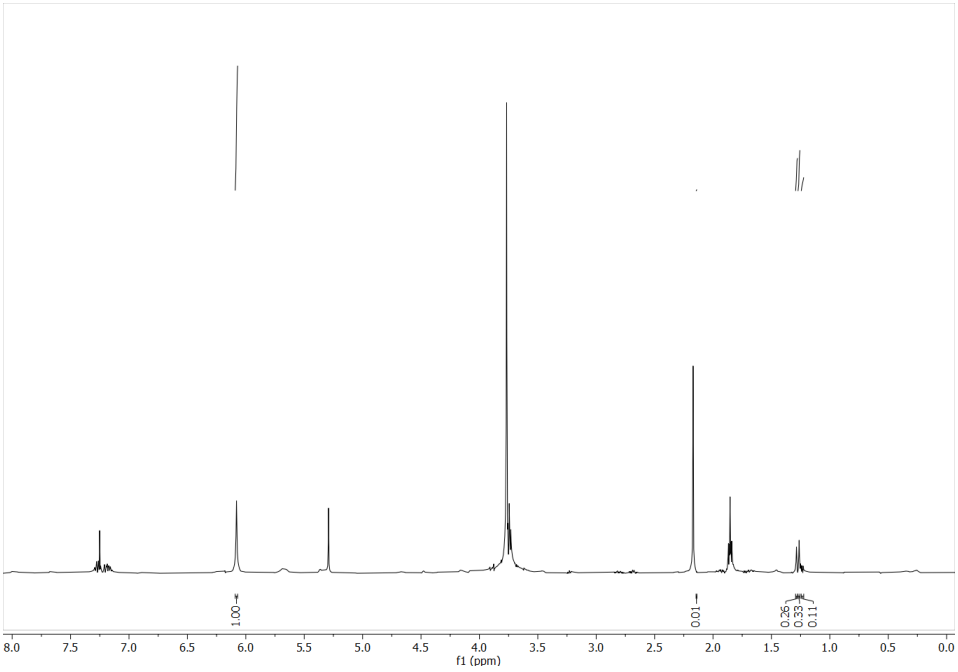

Figure B.8: ^{1}H-NMR of the crude mixture of benzylacetone reduction by commercial SmI_2 with 5 eq. added LiI. Spectra were referenced to 1,3,5-trimethoxybenzene (10.3 mg, 6.08 ppm, s, 3H) as internal standard.

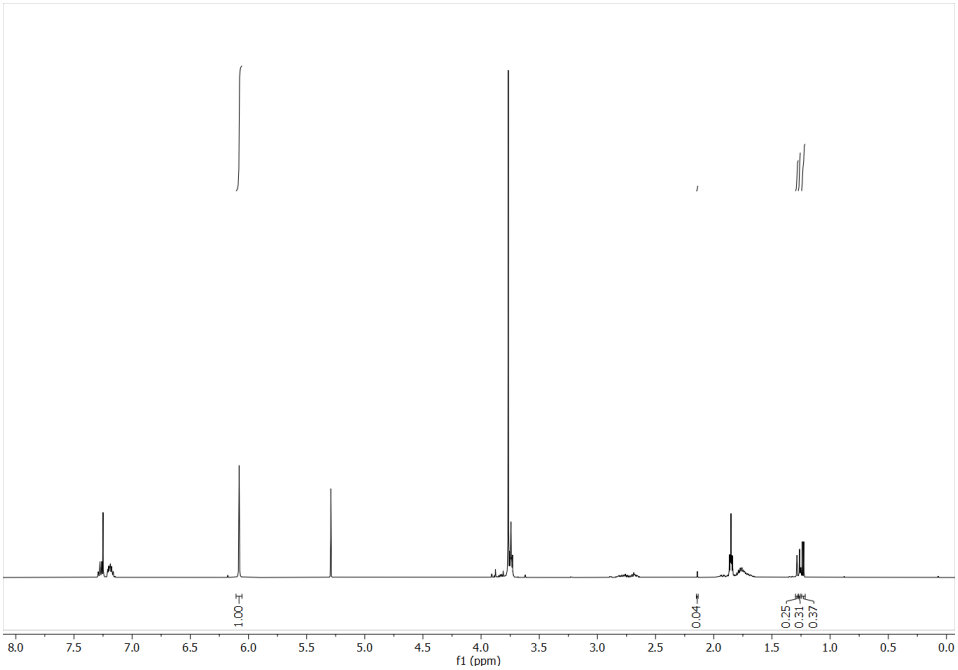

Figure B.9: ^{1}H-NMR of the crude mixture of benzylacetone reduction by electrogenerated SmI_2. Spectra were referenced to 1,3,5-trimethoxybenzene (8.7 mg, 6.08 ppm, s, 3H) as internal standard.

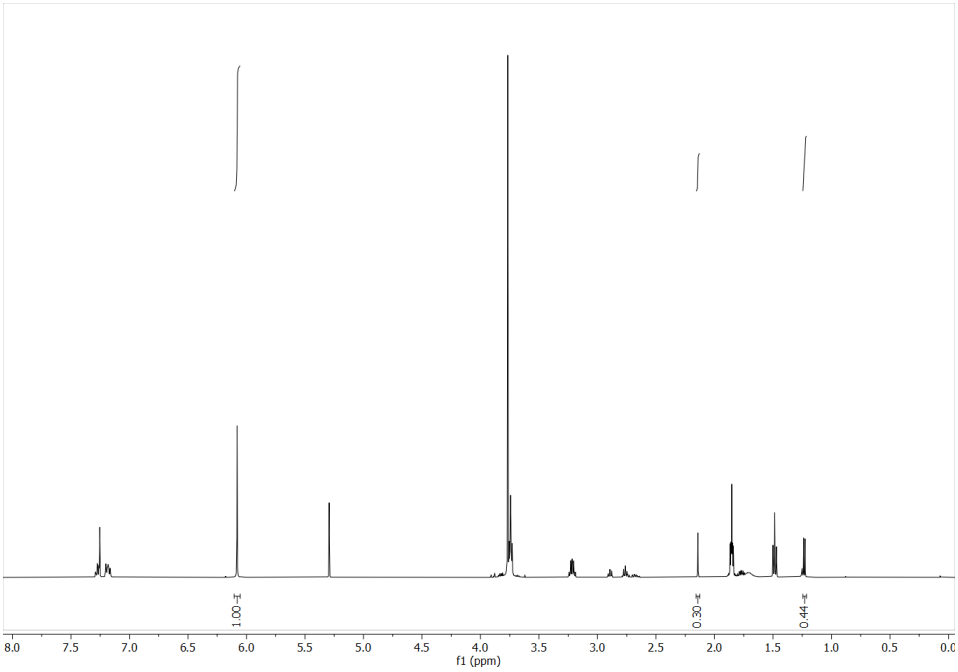

Figure B.10: ^{1}H-NMR of the crude mixture of benzylacetone reduction by commercial SmI_2 with 8 eq. added H_2O and 6 eq. added Et_3N. Spectra were referenced to 1,3,5-trimethoxybenzene (10.0 mg, 6.08 ppm, s, 3H) as internal standard.

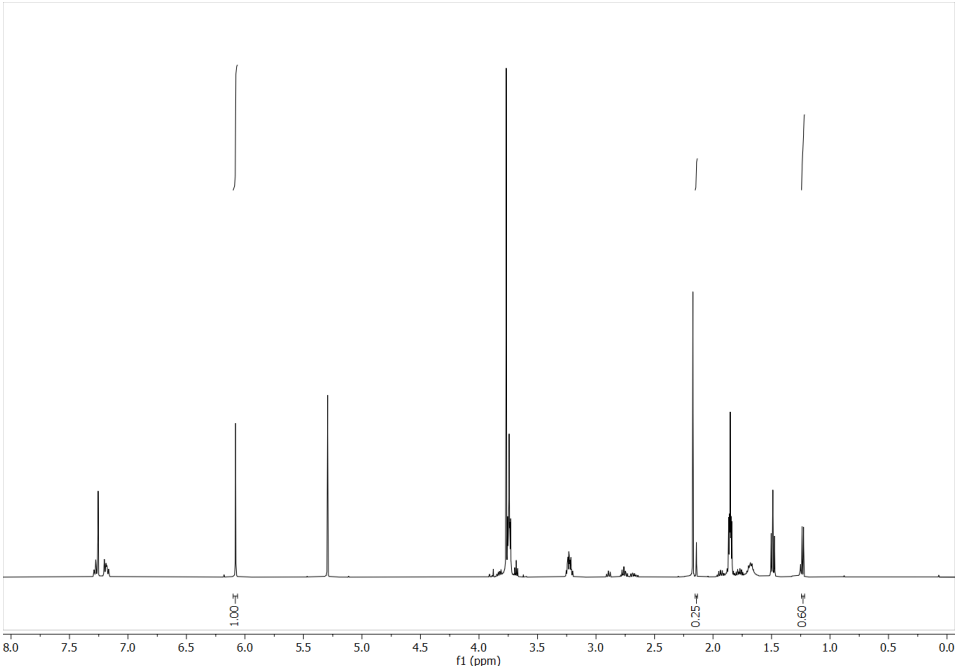

Figure B.11: ^{1}H-NMR of the crude mixture of benzylacetone reduction by commercial SmI_2 with 8 eq. added H_2O, 6 eq. added Et_3N, and 5 eq. added LiI. Spectra were referenced to 1,3,5-trimethoxybenzene (8.7 mg, 6.08 ppm, s, 3H) as internal standard.

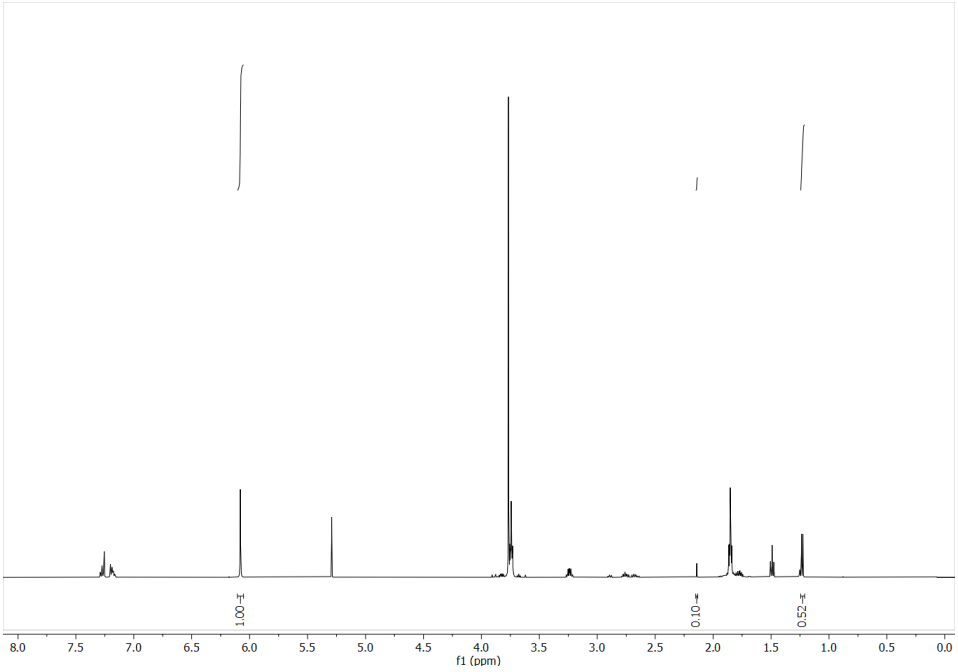

Figure B.12: ^{1}H-NMR of the crude mixture of benzylacetone reduction by electrogenerated SmI_2 with 8 eq. added H_2O and 6 eq. added Et_3N. Spectra were referenced to 1,3,5-trimethoxybenzene (12.4 mg, 6.08 ppm, s, 3H) as internal standard.